Supporting Information

Linking zeolite structures to reactivity in the carbonylation of dimethyl ether

Dong Jae Jeong[1], Xu Wang[2], Nam Jun Park[1], Donggyu Lee[1], Yongkyu Lee[1], Jong Wook Bae[2], Won Bo Lee[1], Jong Hun Kang[1,*]

[1] School of Chemical and Biological Engineering and the Institute of Chemical Processes, Seoul National University, Seoul 08826, Republic of Korea

[2] School of Chemical Engineering, Sungkyunkwan University (SKKU), 2066 Seobu-ro, Jangan-gu, Suwon, Gyeonggi-do, 16419, Republic of Korea

* Corresponding author E-mail: jonghunkang@snu.ac.kr

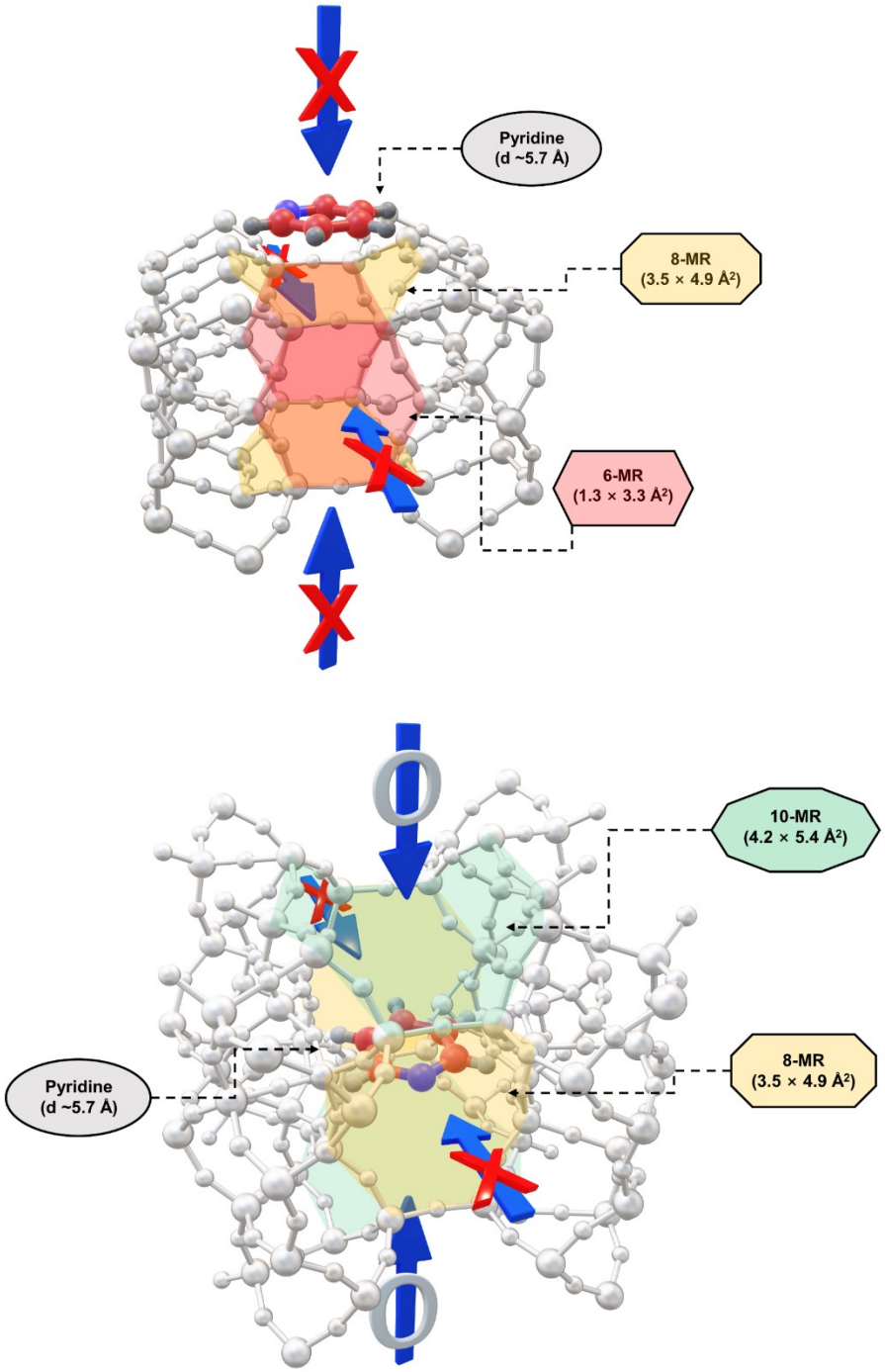

Fig S1. Schematic representations of NH_3-TPD and Pyridine IR analysis for FER. Pyridine can diffuse through 10-MR channel because of its molecular diameter (~5.7 Å) larger than 8-MR pores (3.5 × 4.9 $Å^2$), selectively adsorbing on acid sites in larger structures, which can distinguish the influence of non-8-MR acid sites.

a

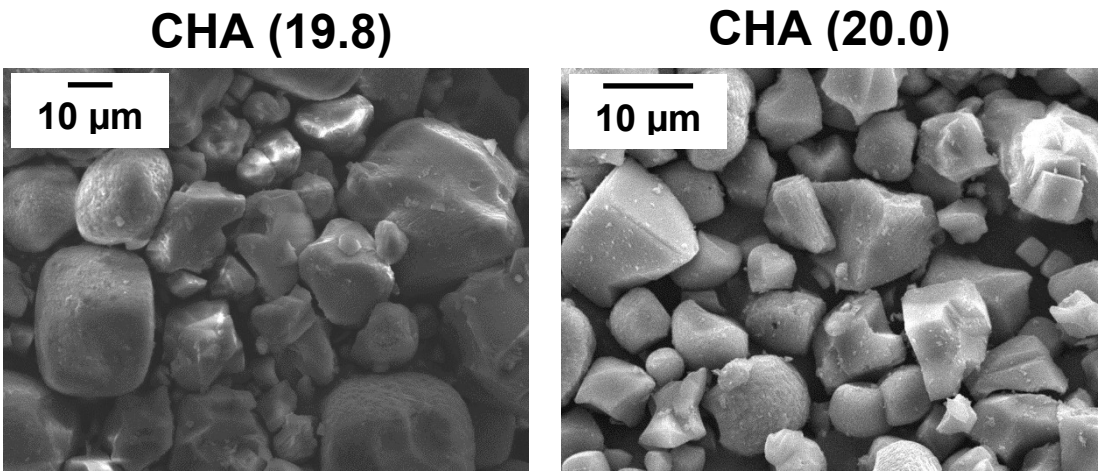

b

Zeolite	CHA	
Sample	CHA (19.8)	CHA (20.0)
Crystal phase	CHA	CHA
Si/Al molar ratio (SEM-EDS)	19.8	20.0
Particle size (μm)	10-40	3-15
Strong acid site density (mmol g^{-1})	1.346	1.329
MA generation rate (mol $kg_{cat}^{-1} h^{-1}$)	13.40	13.47
TOF (h^{-1})	9.95	10.13

c

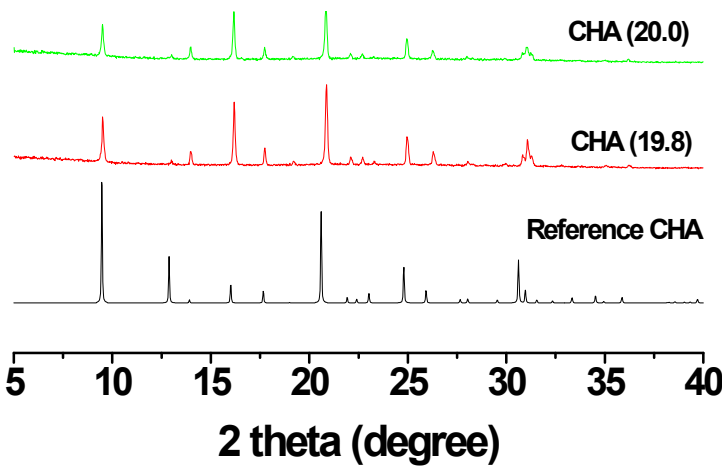

Fig S2. Characterizations of CHA zeolites with similar Si/Al ratios and different crystal sizes (CHA 19.8 vs. CHA 20.0) used to evaluate the impact of internal diffusion. (a) SEM images, (b) SEM-EDS, particle size from SEM images, and catalytic performances, and (c) XRD. Despite a significant difference in particle size, both samples exhibit comparable methyl acetate (MA) generation rates and turnover frequencies (TOFs) for DME carbonylation, suggesting that the reaction is not limited by intracrystalline diffusion, as further supported by the Weisz–Prater criterion.

Section 1

Criteria for Selecting Effective Brønsted Acid Sites for DFT Calculations

For each topology investigated in this study—CHA, FER, LTA, ERI, AEI, and STI—the preferred Al T-site was first identified, followed by an investigation of the oxygen sites where Brønsted acid is most likely to be stochastically distributed. The TxOy sites mentioned in this section are numbered according to the cif files of each zeolite topology from the IZA database. For a detailed structural examination, it is recommended to use visualization tools—VESTA, IRASPA, Crystalmaker etc.

CHA

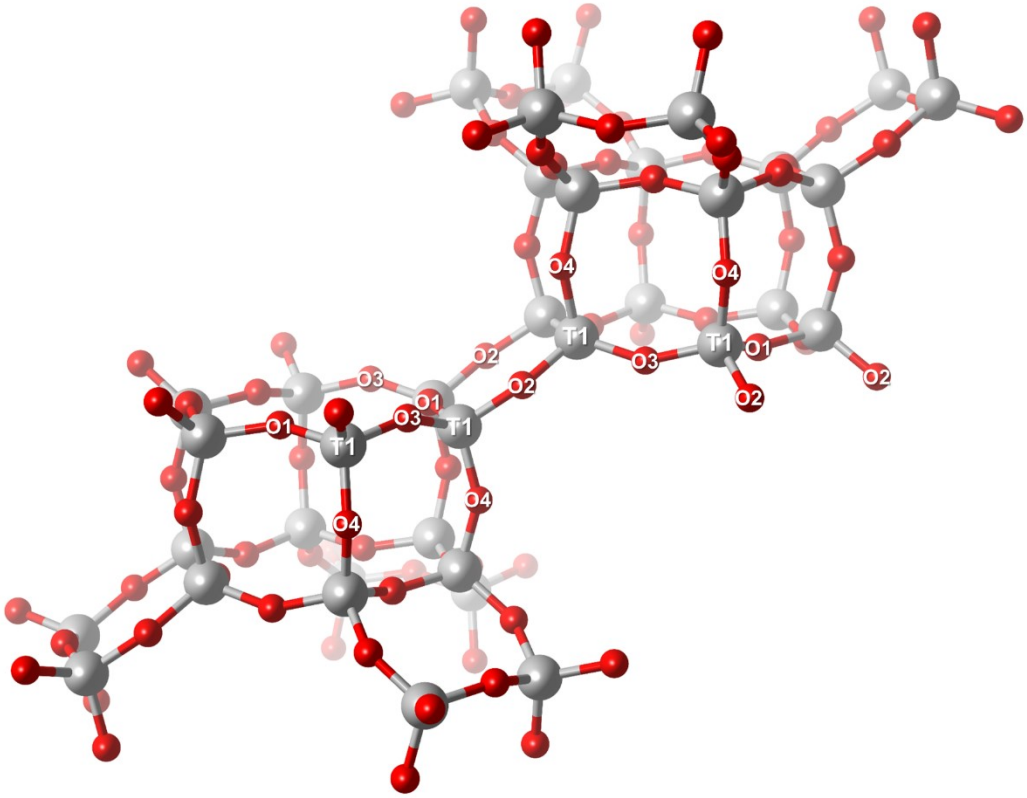

CHA has only one tetrahedral site (T-site), with four distinct oxygen atoms (O1, O2, O3, and O4) distributed around it. Previous research[1] indicates that the equilibrium proton coverage, or the probability of Brønsted acid site (BAS) distribution, follows the order O1 > O2 > O3 > O4. As the temperature of the CHA structure increases, this ranking order remains the same, but the ratios shift, indicating that the distribution of protons adjusts with temperature while maintaining the same overall hierarchy. O1 is located only on 6-MR and 4-MR rings in the framework, while O2, O3, and O4 are found on 8-MR, suggesting that O1 contributes less to the DME carbonylation reaction.

In this study, the maximum temperature to which CHA was exposed during the synthesis process was 853 K, at which O1 shows a fractional coverage of about 44%. At the reaction temperature of 438 K, this coverage increases to around 60%. Although it is possible to quantify the proportion of TxOy sites involved in the reaction through these indicators, determining the exact equilibrium proton coverage in

situ during actual reactions remains challenging. Only recently have studies begun considering the nuclear quantum effect in such simulations. While it is highly meaningful to identify the directly accessible proton sites—*i.e.*, the proton coverage at each oxygen site—using this method, it was not applied to all of the topologies investigated in this study (FER, LTA, ERI, AEI, STI). Furthermore, this approach would be too complex to apply on zeolites with multiple distinct T-sites. Therefore, in addition to the previously introduced research, we will refer to other studies on the criteria for selecting effective T-sites for each topology.

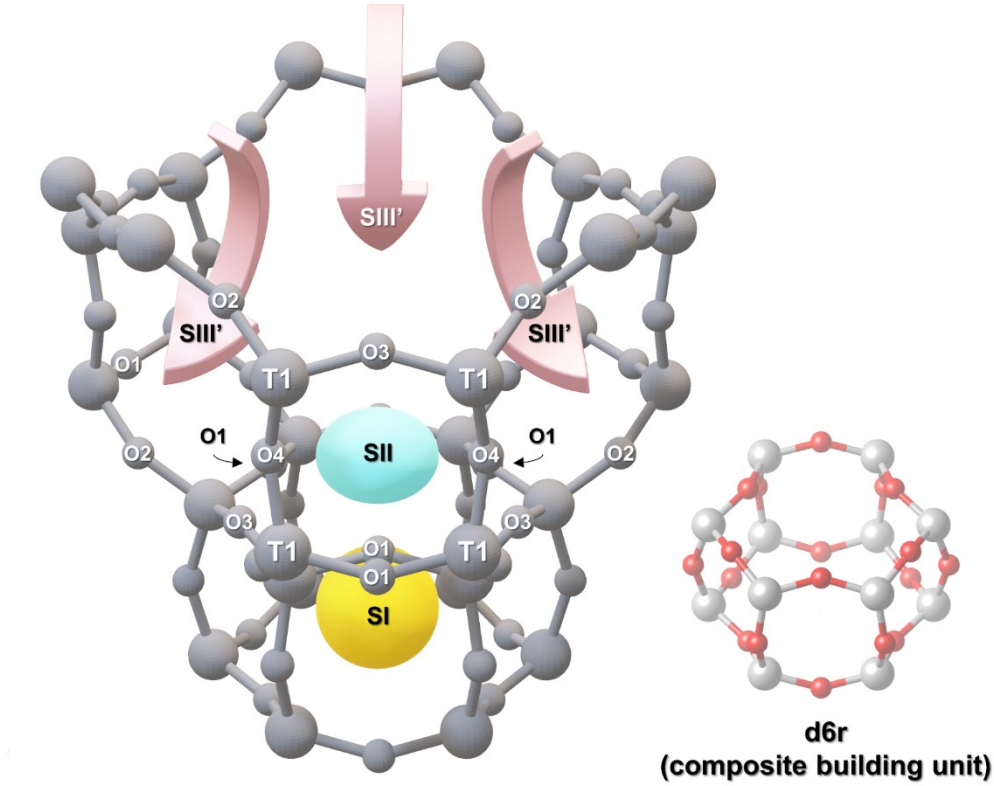

Since CHA has only one T-site, it is important to distinguish the preferred proton siting pattern as the Al content increases by examining different regions within the CHA cage. In previous studies[2, 3], as shown in the figure above, the CHA cage was divided into three zones to observe how the probability of proton siting changes, mainly driven by the shifting position of Na^+ (the counter cation during the synthesis phase) as Al substitution increases. In high-silica CHA (low Al ratio), consistent with prior research on proton coverage, Na^+ tends to be located in the SII region above the d6r structure. After ion exchange to form H-CHA, the likelihood of the proton being positioned at O1 increases. For O3, which is also part of the d6r structure, protons tend to form outside the d6r center and ultimately position themselves in the 8-MR pore due to the Al–O–Si atomic angle.

As more Al is substituted, additional Na^+ is required to balance the charge, causing Na^+ to occupy not only the SII site but also the SIII site. The likelihood of Na^+ occupying SIII increases as Al substitution rises. This phenomenon starts to become noticeable at a Si/Al ratio of 48 and becomes more pronounced as more Al is added to the CHA cage. Since SIII is located near the 8-MR pore, the number of protons that can be located in the 8-MR increases as well. This trend is consistently reflected in the NH_3-TPD results for the CHA group in this study, where the amount of strong acid associated with 8-MR Brønsted acid sites increases proportionally as the Si/Al ratio decreases.

FER

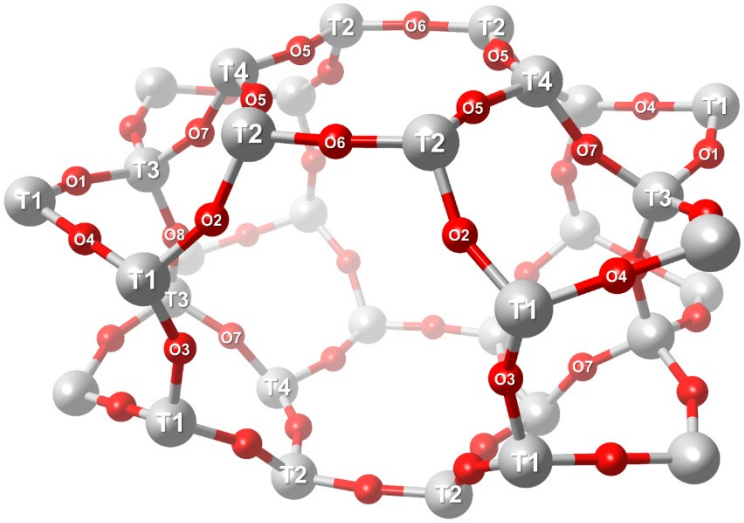

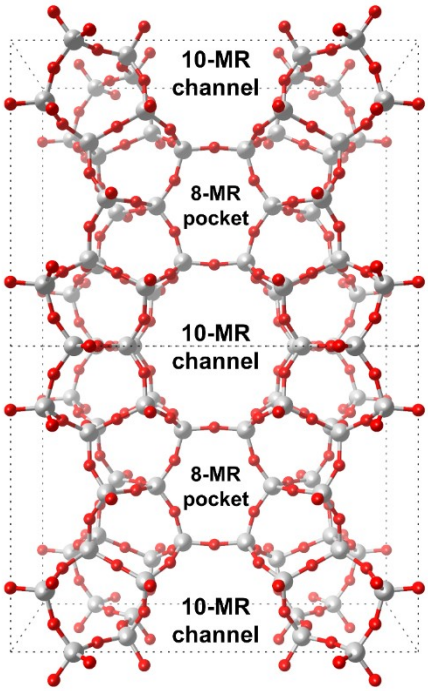

The active sites for DME carbonylation were found to be located in the 8-MR pocket of FER.[4, 5] Martucci et al.[6] identified two main Brønsted acid sites: T3(4)O7 and T1O3. The first proton site was on framework oxygen O7, which bridges T3 and T4, and is oriented toward the center of the ferrierite 8-MR pocket. The second site was on framework oxygen O3, which bridges two T1 tetrahedron cations.

Feng et al.[7] further investigated the activation energy for CO addition during the DME carbonylation process at these sites. At the T1O3 site, the activation energy for CO addition was not competitive compared to the activation energies for the adsorption of other substances (H_2O, CH_3OH, DME). However, at the T4O7 site, the activation energy for CO addition was significantly lower, that allowed CO to compete more effectively with other substances.

LTA

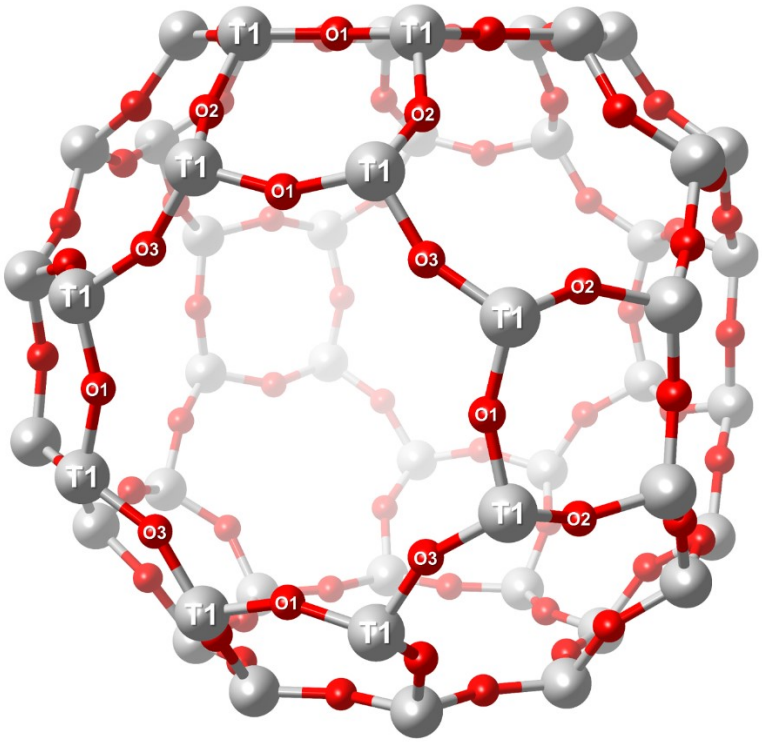

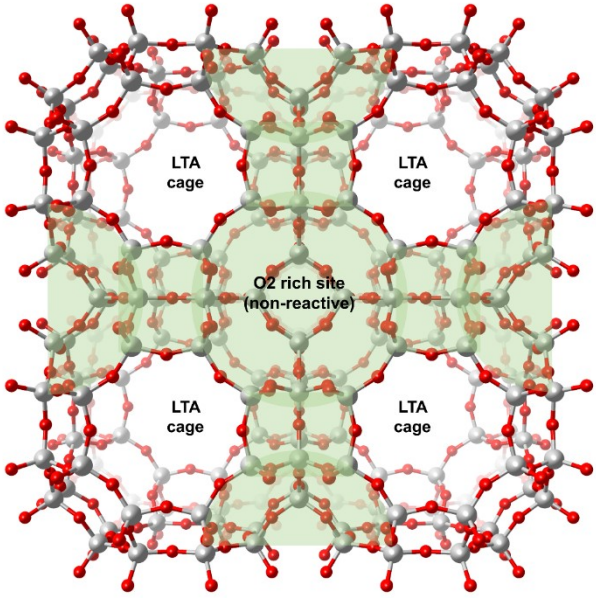

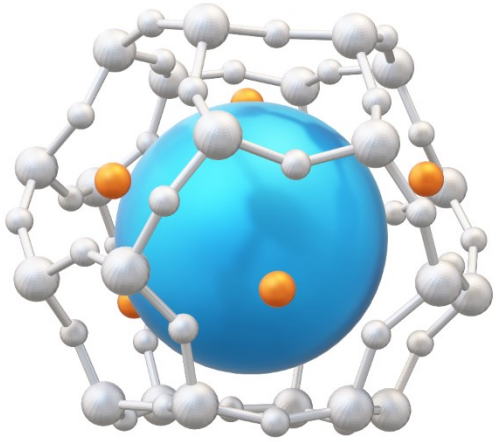

LTA also has only one tetrahedral site (T1), making it necessary to determine oxygen site in which the Brønsted acid site (BAS) is primarily distributed. Lemishko et al.[8] confirmed the distribution of these sites using the Inelastic Neutron Scattering (INS) method and identified the most BAS-dense site through DFT calculations. By comparing the experimentally confirmed fundamental vibration and first overtone

for LTA with a Si/Al ratio of 40 (synthesized) to the pattern calculated by DFT for a Si/Al ratio of 47 (modeled), they predicted that most BASs are located at the T1O2 site.

LTA has one LTA cage per unit cell, along with one sodalite cage and three d4rs (cubic with 8 T sites). Since the sodalite cages and d4rs barely contain 8-MR pores, they are non-reactive for the DME carbonylation reaction (referred to as green sites). According to Lemishko et al., T1O2 is the preferred site for BAS in high-silica LTA. The high probability of T1O2 being predominantly distributed in these non-reactive green sites suggests that DME carbonylation reactivity would be very low.

Typically, six Na^+ cations can exist within the sodalite cage (SOD Si/Al ratio = 1).[9-11] As the Si/Al ratio decreases (with more Al substitution), it becomes less likely for BAS to be located anywhere other than O2, because there is still space for additional Na^+ cations to occupy the sodalite cage. This behavior is very similar to that observed in CHA.

In CHA, Na^+ is preferentially located in the non-reactive d6r structure, but as that region becomes saturated with Na^+, other regions—including the reactive 8-MR—gradually become occupied by Na^+. This TxOy site substitution in the 8-MR has been discussed in the CHA section. While CHA has two non-reactive sites (SI) per unit cell, LTA can have up to eight such sites at the vertices of the unit cell. With an average of six Na^+ ions in LTA, even at a Si/Al ratio of 7 (= $Si_{42}Al_6O_{96}H_6$), the probability of BAS being located in these O2 sites remains very high.

ERI

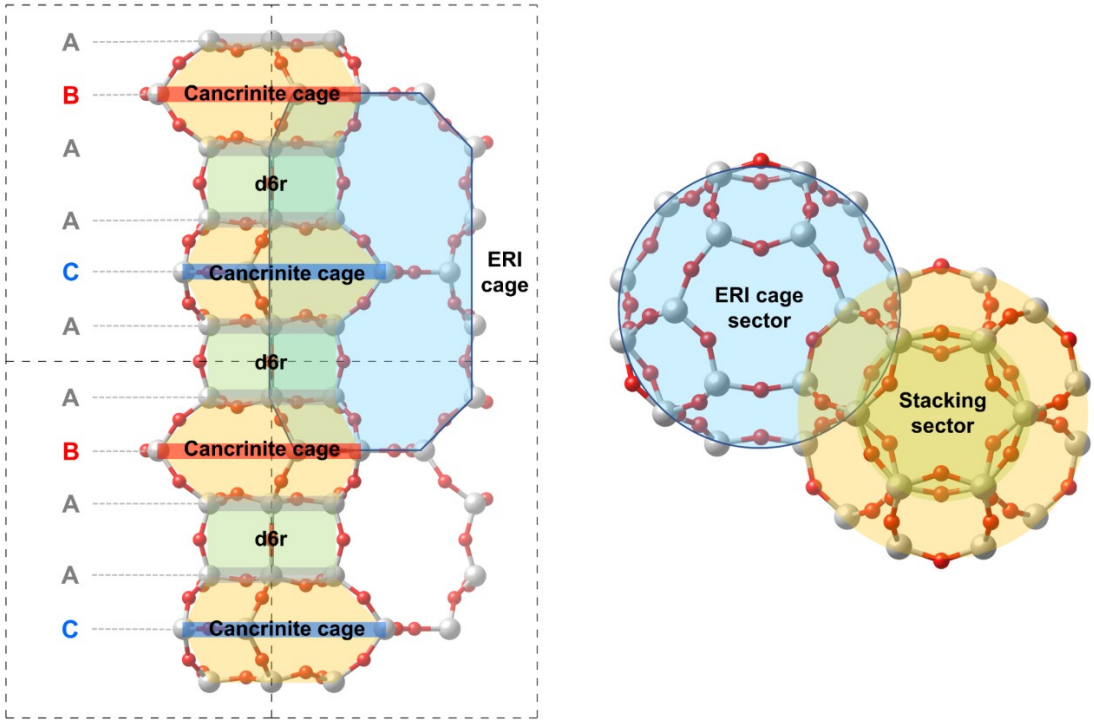

Similar to CHA, ERI also has a hexagonal unit cell, but the cage connections differ significantly due to the distinct arrangement of repeating structures. To reach the next closest equivalent ERI cage in the unit cell along the c-axis, ERI requires two connections via 8-MR. In contrast, CHA needs three connections via 8-MR to reach the nearest CHA cage with the same x and y coordinates. These differences highlight variations in cage density per unit cell between the two structures, which directly impact their catalytic properties. The unique stacking pattern of ERI, when compared to CHA, creates distinct environments for reactivity and diffusion within the pore system.

ERI is primarily divided into two sectors: the ‘Stacking sector’ and the ‘ERI cage sector.’ The d6r and cancrinite (CAN) cage structures alternate along the c-axis, with the CAN cages arranged in a zigzag pattern following the ‘AABAAC’ stacking sequence. The stacking sector sits alongside ERI cage sectors that are adjacent to it in six directions. The stacking sector contains only pores smaller than 8-MR, making it not only challenging for reactions to occur but also limiting it as a diffusion path for reactants. In contrast, the ERI cage sector provides more accessible reactive sites, illustrating a key structural difference between ERI and CHA: ERI’s coexistence of both reactive (ERI cage sector) and non-reactive (stacking sector) components within a single unit cell. If ERI had the same stacking pattern as CHA, the difference in reactivity between the two topologies would be attributed solely to the shape of the cage and the 8-MR eccentricity. This suggests that the stacking pattern itself plays a significant role in determining the performance of zeolite-based catalysts, particularly for reactions that take place in small pores, such as DME carbonylation.

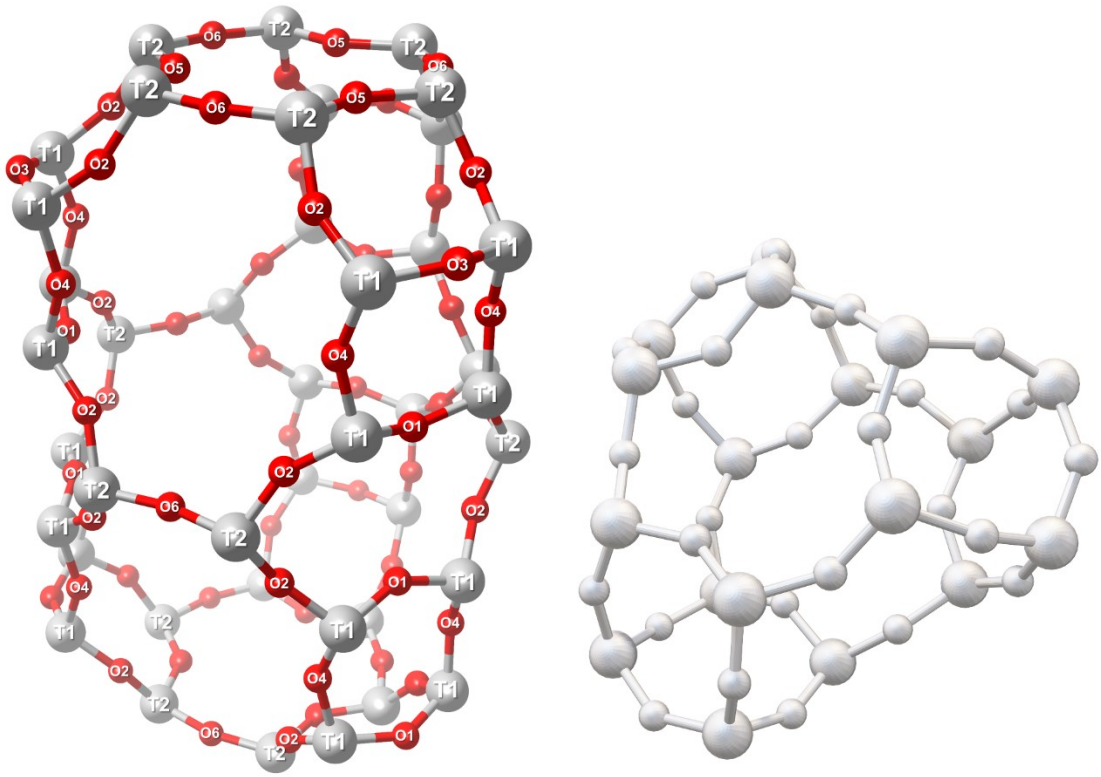

The catalytic performance of ERI is dependent on the occupancy of its two unique T-sites, T1 and T2. Previous works[12, 13] demonstrated that aluminum substitution in low Si/Al ratio ERI is non-random, with a preference for aluminum to occupy the T2 sites. In the stacking sector, d6r and cancrinite (CAN) cages compensate for aluminum at the T1 site, while the ERI cage compensates at the T2 site. However, when examining the occupancy ratio (R1/R2) of T1 and T2, the study found that R1/R2 ratio significantly decreased as the Si/Al ratio in ERI decreased. This indicates that aluminum is more selectively substituted at the T2 site, even though there are twice as many T1 sites per unit cell as T2. This implies that T1, which compensates for the d6r or CAN cages, is minimally replaced, while the remaining cations are arranged to compensate for the T2 site based on the spatial distribution of charge. This behavior mirrors the proton coverage occupancy shifting with charge arrangement previously discussed in the case of CHA.

ERI is a zeolite that is challenging to synthesize with high silica content, but recent studies have successfully synthesized it with a Si/Al ratio as high as 9. Due to this high silica content, it is difficult to observe a gradual pattern of preferred Al T site substitution in high-silica ERI, unlike CHA or LTA. However, since this study used only low-silica ERI (Si/Al = 5) as a test catalyst, it seems reasonable to apply the findings from previous studies directly. The impact of aluminum distribution, stacking pattern, and cage connectivity will ultimately play a key role in determining the performance of ERI as a catalyst, particularly for reactions in small-pore environments.

AEI

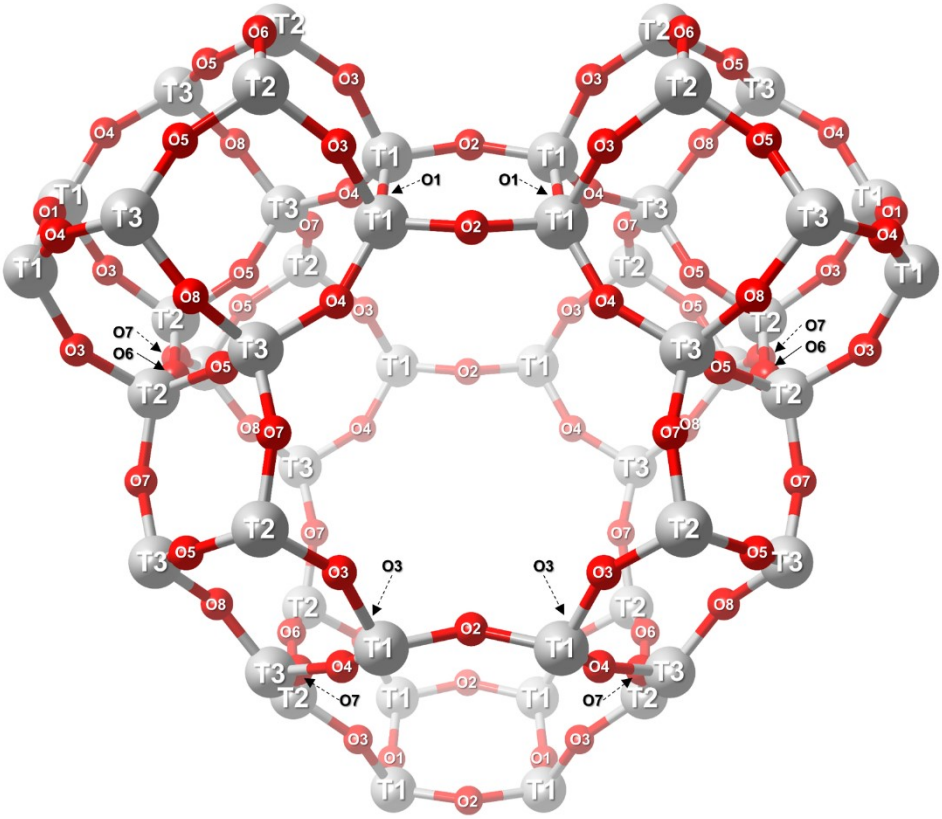

AEI is a zeolite similar to CHA, but with notable differences. Both zeolites form their unique channel structures through the continuous arrangement of d6r, but the crystallographic elements can be clearly distinguished by how the d6r units are arranged along the c-axis. Several studies have reported that AEI and CHA can be synthesized from raw materials capable of inducing d6r and other secondary building units, which serves as an important basis for selecting the preferred TxOy site in AEI. Unlike CHA, which has a single T-site, AEI contains three distinct T-sites and eight different O-sites, making the simulation of preferred TxOy sites more complex, with exponentially more possibilities.

Rather than simulating all the possibilities based on the number of Al atoms substituted per unit cell, it is necessary to consider the preferred positions of the counter cation during the synthesis process, as discussed earlier. In CHA, the SII site (above d6r) is initially preferred, but as more Al is substituted, the probability of SIII' occupation increases. A similar trend can be inferred in AEI, where the probability of Al being preferred near the 8MR pore increases as the counter cation Na^+ occupies those sites.

AEI has been widely applied in NH_3-SCR reactions, with various analytical tools used to quantify the paired aluminum sites contributing to reactivity. However, determining the specific locations in the structure where Al is predominantly located remains challenging. Since data alone may not be sufficient to fully concretize these findings, it seems necessary to infer the preferred sites through this method.

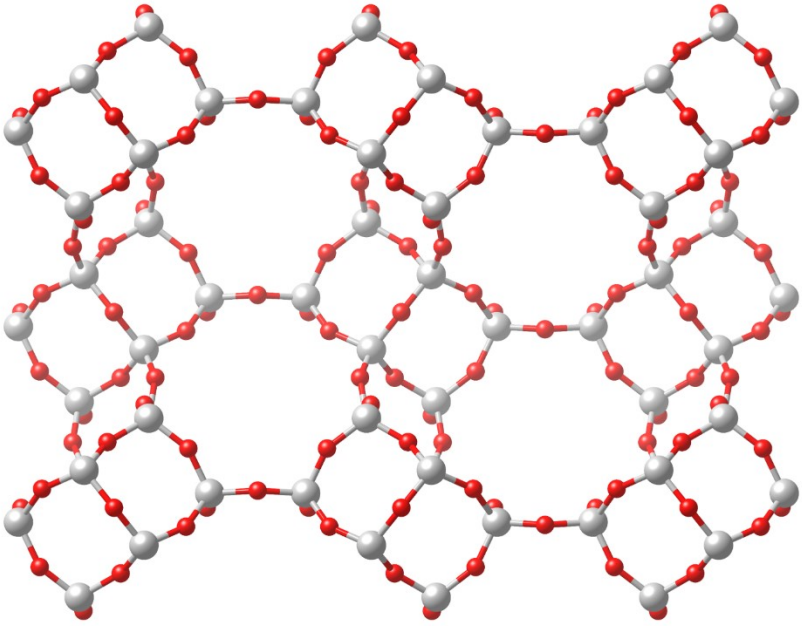

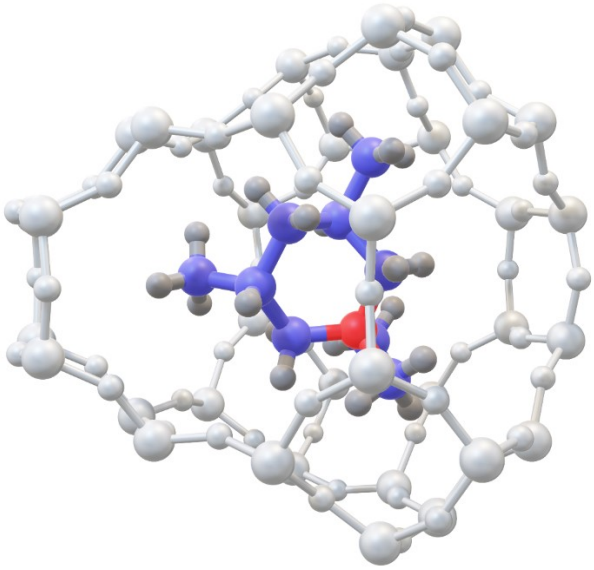

In this study, the primary objective was to investigate the activation energy of the CO addition reaction, which occurs after methylation, at the proton site located in the 8-MR. Therefore, we selected the T1O2 site, one of the TxOy sites that form the 8-MR, and examined the activation energies for both CO addition and H_2O addition processes at this site.

STI

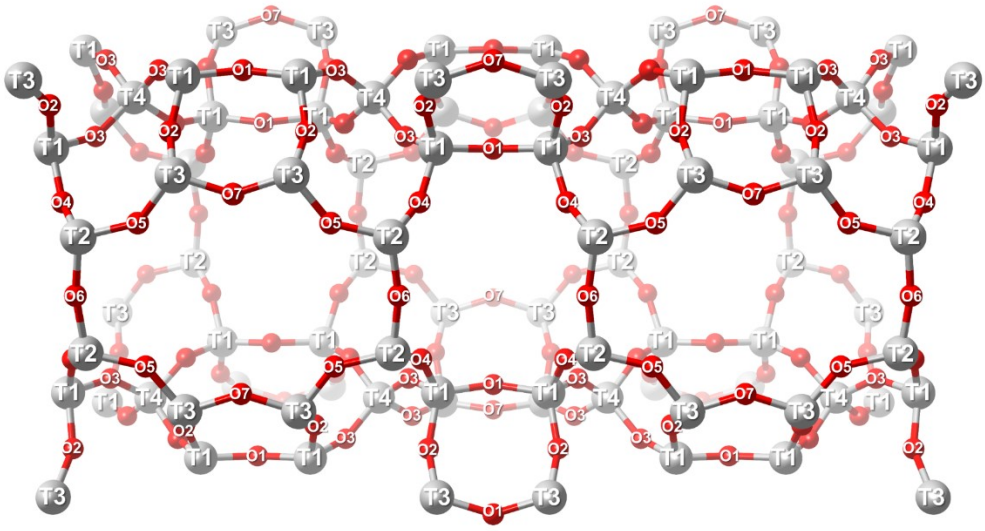

Stilbite (STI) holds an important place in the history of zeolite research as one of the earliest known natural zeolites. It was part of the mineral group that led Swedish mineralogist Axel Fredrik Cronstedt to first coin the term "zeolite" in 1756, after observing that the mineral released steam when heated. Stilbite, like other zeolites, has a unique framework structure, consisting of four tetrahedral (T) sites and seven unique oxygen (O) sites. Its discovery was pivotal in the early exploration of zeolite properties and their industrial applications.

Due to the numerous T and O sites in STI structures, there are few studies that clearly identify the preferred Al T site. A case study on possible Al T sites using global minima structures with varying Si/Al ratios—based on the number of aluminum atoms substituted at tetrahedral T sites—similar to the approach used for CHA or LTA[14], where energy potentials are compared for each case, is challenging to apply to STI because of the vast number of configurations to be considered.

Instead, like an approach in AEI, it is more feasible to determine the Al distribution based on the preferred sitting of the counter cations that influence the zeolite structure. However, STI exhibits a stronger host-guest interaction between the OSDA and the framework during synthesis compared to AEI regarding to the distance between zeolite framework (host) and OSDA (guest molecule). Therefore, it is more appropriate to determine the Al distribution in relation to the OSDA location within the zeolite framework during synthesis, as Al atoms are more likely to be sited in which partial positive charges can be effectively compensated.

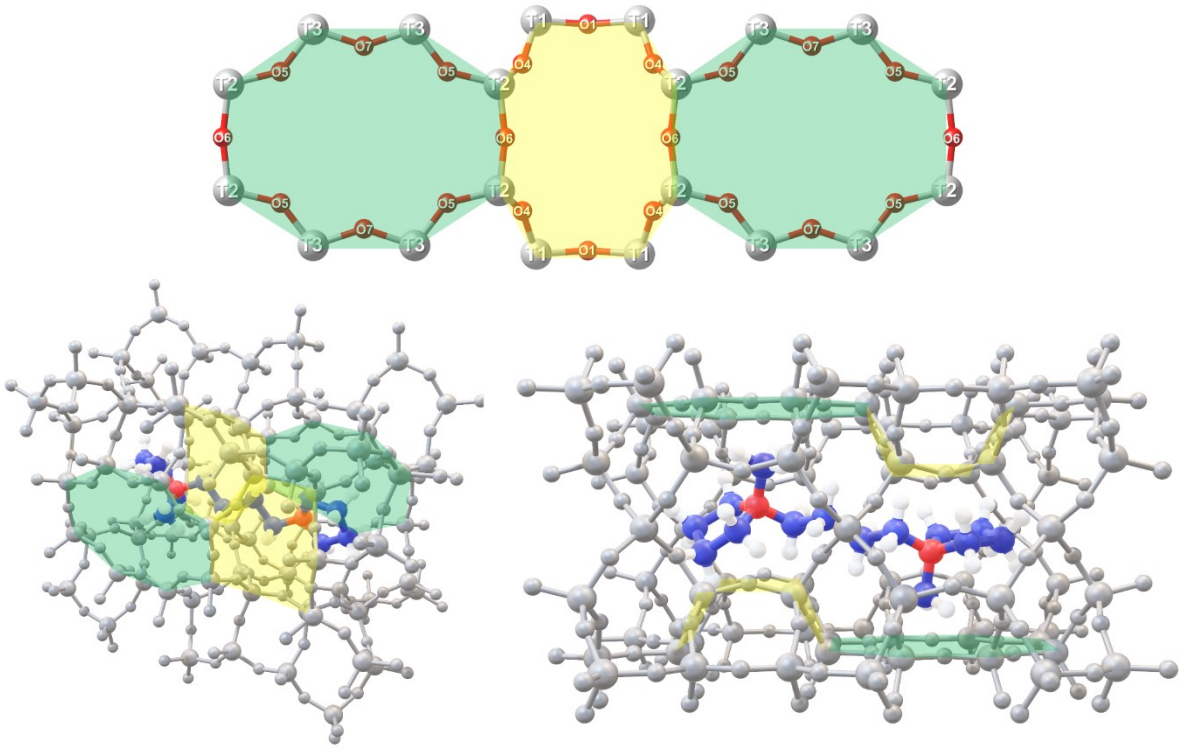

As shown in the figure above, STI consists of two types of 8-MRs arranged sequentially along the 10-MR channel direction. Each site is composed exclusively of T2 and T3 sites (green), or T1 and T2 sites (yellow). The OSDA used in the synthesis process, 1,4-bis(N-methylpyrrolidinium)butane (1,4-MPB), has a positively charged N^+ group positioned closer to the 8-MR which contains T2 and T3 sites (green). This suggests a higher probability that Brønsted acid sites will be distributed at the oxygen sites corresponding to the T2 and T3 locations. Accordingly, it is likely that the Brønsted acid site is distributed at one of the oxygen sites connected to T2 or T3. In this study, T2O5 was selected as the representative scattered point for STI.

Section 2

Syntheses of Organic Structure-directing Agents (OSDAs)

Materials

1,2-dimethylimidazole (98%, Thermo Fischer Scientific), 4-methylbenzyl chloride (98%, Sigma-Aldrich), 3,5-dimethylpiperidine (mixture of *cis* and *trans*) (Sigma-Aldrich), Iodomethane (99%, Sigma-Aldrich), Potassium bicarbonate (99.5%, Daejung chemical), 1,4-dibromobutane (98%, Alfa Aesar), and N-methylpyrrolidine (99%, Sigma-Aldrich) were used as-received without further purification.

Organic Syntheses

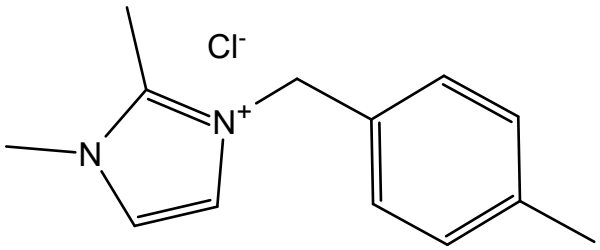

1,2-dimethyl-3-(4-methylbenzyl)imidazolium chloride (12DM34MBI$^+$Cl$^-$) was synthesized by the S_N2 reaction between 1,2-dimethylimidazole and 4-methylbenzyl chloride.[15] 14.4 g of 1,2-dimethylimidazole (150 mmol) was dissolved in 200 ml of toluene and heated to 45 °C with stirring. 21.1 g of 4-methylbenzyl chloride (150 mmol) was added dropwise. The reaction mixture was heated to 105 °C and allowed to run for 24 hours. The desired product precipitated because it is insoluble in toluene. The solid was separated by filtration, rinsed with copious amounts of diethyl ether, and dried in a vacuum at ambient temperature.

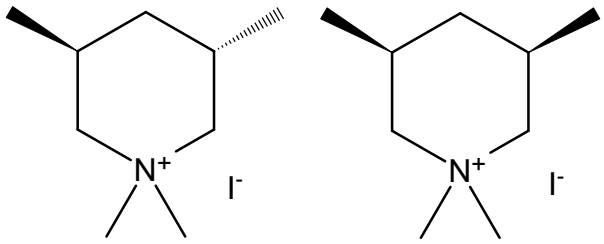

One-to-one-ratio *cis*/*trans* mixture of N,N,3,5-tetramethylpiperidinium ion was synthesized by the S_N2 reaction between 3,5-dimethylpiperidine (mixture of *cis* and *trans*) (DMP) and iodomethane (CH_3I). The reaction was carried out by mixing DMP, iodomethane, and potassium bicarbonate ($KHCO_3$) in a molar ratio of 1:4:4 with chloroform as a solvent. (*Cautions: Iodomethane must be gradually introduced over 24 hours using a dropping funnel to keep the reaction temperature from increasing too quickly. The reaction chamber should be wrapped in foil and used as a light shield to prevent the iodide in the reaction solution from generating electrons in response to light, resulting in a side reaction.*) After the reaction was completed, the solution was filtered through a nylon membrane filter, and chloroform was removed from the filtrate using a rotary evaporator to get N,N,3,5-tetramethylpiperidinium iodide (TMPI). This was dissolved in diethyl ether, filtered again, and then dried in a vacuum oven for more than 12 hours.

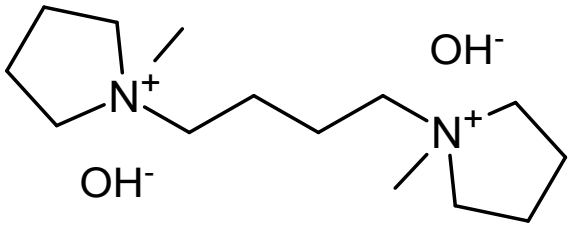

The divalent 1,4-bis(N-methylpyrrolidinium)butane (1,4-MPB) cation was produced by refluxing 1,4-dibromobutane with an excess of N-methylpyrrolidine in acetone overnight. The excess amine was extracted with acetone before recrystallization in methanol-diethyl ether mixtures. Due to its hygroscopic properties, this diquaternary ammonium salt must be kept in a desiccator before being used as an OSDA for synthesizing zeolites.

Ion-exchange and Titration

The aforementioned organic halides were converted into hydroxides, if necessary. The organic salts were dissolved in distilled water and combined with strong base anion exchange resin (TRILITE® MA-15OH (Samyang)). For each 100 mmol of OSDA halide, 600 mL of distilled water and 300 mL of resin were used to ion-exchange. The mixture was stirred for 24 hours at room temperature. The used resin was separated using filtration. The solution phase was collected in a round bottom flask and concentrated with a rotary evaporator. The concentration of OSDA hydroxide was determined by the usual titration method with a 0.01 N HCl solution (Daejung chemical).

Syntheses of Molecular Sieves

Materials

All materials for synthesizing small-pore molecular sieve materials were used as-received without further purifications from the stated vendors. The water contents of the solid sources were determined by temperature gravimetric analysis (TGA). Aluminum sources used were aluminum isopropoxide (98%, Sigma-Aldrich), sodium aluminate (54.4 wt. % Na_2O, 32.6 wt. % of Al_2O_3, 13.0 wt. % of water, Daejung chemical), pseudoboehmite (Catapal B, 27.4 wt. % of water, Vista specialty chemicals), and aluminum nitrate nonahydrate (98%, Sigma-Aldrich). For AEI synthesis, zeolite Y was employed as the silicon and aluminum sources. Zeolyst CBV500 (Si/Al ratio = 2.6, 14.3 wt. % of water). Silica sources were colloidal silica (Ludox AS-40, Sigma-Aldrich), fumed silica (Cab-O-Sil M-5, Thermo Fisher Scientific), and tetraethyl orthosilicate (TEOS, 99.9%, Alfa Aesar). For alkali hydroxide mineralizing agents, sodium hydroxide (50% aqueous solution, Daejung chemical), and Potassium hydroxide (25% aqueous solution, Daejung chemical) were mainly used. For STI synthesis, sodium fluoride (97%, Daejung chemical) was adopted for anion balancing with sodium hydroxide.

The following OSDAs were used as-received from the stated vendors: N,N,N-Trimethyl-1-adamantamonium hydroxide (CAS RN 53075-09-5, 25 wt. % in H_2O, Sachem), pyrrolidine (99%, Sigma-Aldrich), tetramethylammonium hydroxide (TMAOH, 10 wt. % in H_2O, TCI), tetraethylammonium hydroxide (TEAOH, 35 wt. % in H_2O, Sachem), and hexamethonium bromide (HMBr, Sigma-Aldrich).

The following OSDAs were synthesized according to the procedures provided in the previous section: 1,2-dimethyl-3-(4-methylbenzyl)imidazolium hydroxide (12DM34MBI$^+$OH$^-$), one-to-one-ratio *cis*/*trans* mixture of N,N,3,5-tetramethylpiperidinium hydroxide (TMPOH), 1,4-bis(N-methylpyrrolidinium)butane dihydroxide (1,4-MPB$(OH)_2$).

General Procedures

Unless otherwise stated, all zeolites were prepared using the method presented herein. The aluminum source was dissolved in a basic aqueous solution mixture of alkali hydroxide and OSDA. The mixture was stirred until translucent. Next, the silicon source was added to the mixture and stirred at room temperature for 24 h. The gel for the zeolites prepared above was placed in a 40 mL PTFE (polytetrafluoroethylene) liner for a steel autoclave and crystallized (hydrothermally synthesized) under the conditions described in the following section. The collected product sieve was rinsed twice with distilled water and acetone respectively and centrifuged (5,000 rpm, 10×4 min). The separated solid sample was dried overnight in a convection oven set at 100 °C. The as-synthesized samples were then calcined in flowing breathing-grade air to eliminate impurities, including the OSDA, by burning at a 1 °C/min ramp to 150 °C, holding at 150 °C for 3 hours, and a 1 °C/min ramp to 580 °C, holding there for 6 hours. The calcined samples went through ammonium exchange, substituting Na^+ with NH_4^+ as the charge-balancing cation. This procedure involves agitating 1 g of sample in 100 mL of 1 M NH_4NO_3 solution at 80 °C for approximately 8×3 hours. The ammonium-exchanged sample was finally rinsed and dried as stated previously.

Synthesis Conditions (Zeolites)

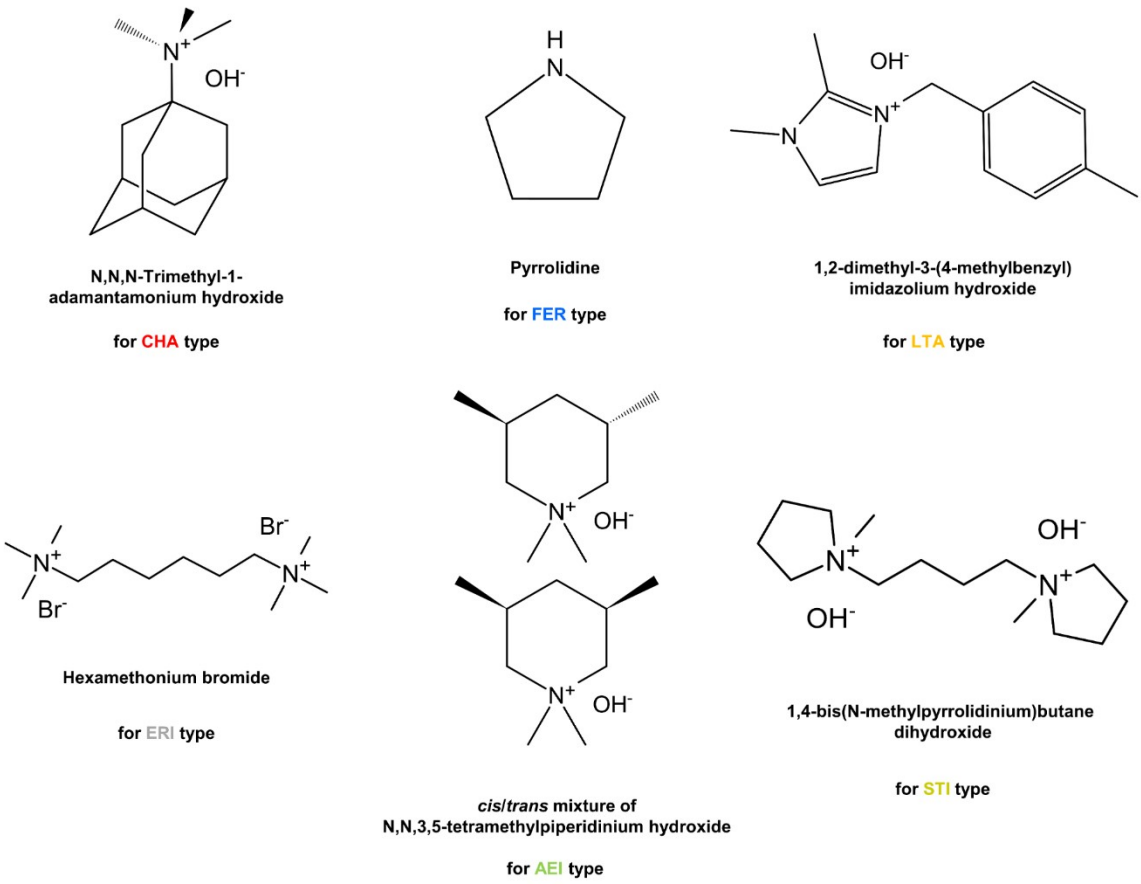

Fig S3. Schematic illustrations of the representative organic materials used to synthesize investigated 8-MR possessing zeolites in this work.

The main OSDAs used to synthesize zeolites are schematically illustrated in Figure S5.

CHA-type zeolites (SSZ-13s) were prepared by using commercial OSDA N,N,N-Trimethyl-1-adamantamonium hydroxide. The desired amount of Ludox AS-40, aluminum isopropoxide, sodium hydroxide as a mineralizer, OSDA, and deionized water was mixed together in a PTFE liner and let them homogenize clearly for 1 day. The final gel composition is 1 SiO_2 : x Al_2O_3 : 0.2 OSDA : 0.2 NaOH : 40 H_2O. The alumina content, x, was varied from 0.014 to 0.083. The gel was crystallized at 160 °C and 60 rpm for 7–14 days.

FER-type zeolites (ZSM-35s) were synthesized using commercial pyrrolidine as OSDA. The desired amount of fumed silica, NaOH, $NaAlO_2$ (sodium aluminate), and deionized water was agitated in PTFE liner and mixed vigorously. Note that $NaAlO_2$ was analyzed by TGA (thermogravimetric analysis) to confirm the portion of water and ICP-OES for quantifying the accurate elemental ratio of Na and Al. The final gel composition was 1 SiO_2 : x Al_2O_3 : 0.911 OSDA : 0.283 NaOH : 40 H_2O, where the alumina content, x, was varied from 0.02 to 0.05. After stirring at room temperature for 1 day, the crystallization was performed in a 160 °C rotating oven under rotation (48 rpm) for 7 days.

High silica LTA series were synthesized in fluoride media with 1,2-dimethyl-3-(4-methylbenzyl)imidazolium hydroxide (12DM34MBI$^+$OH$^-$) and TMAOH as a co-OSDA.[15] The necessary amounts of TEOS and aluminum isopropoxide were hydrolyzed in a mixture of 12DM34MBI$^+$OH$^-$ and TMAOH solution by stirring at room temperature for 1 day. Next, surplus water and alcohol species produced during hydrolysis were evaporated under flowing air. Finally, hydrogen fluoride (HF, 45 wt. % in H_2O, Sigma-Aldrich) was applied dropwise to the gel. (*Caution: HF is a hazardous chemical that can inflict deadly burns and permanent damage to human skin, tissue, and bone. It must be handled with suitable personal protective equipment (PPE), such as a lab coat, respirator, full-face shield, acid apron, long-sleeve nitrile gloves, and so on, with proper ventilation in a fume hood.*) The viscous translucent gel became powdery after the addition of HF. The resulting fluoride gel was then dried under a fume hood for two days. The necessary amount of distilled water was added to achieve the desired gel composition. Finally, Pure-silica LTA (ITQ-29) was added as the seed. The final gel composition was 1 SiO_2 : x Al_2O_3 : 0.45 12DM34MBI$^+$OH$^-$: y TMAOH : 0.5 HF : 5 H_2O, with the alumina content, x, ranging from 0.01 to 0.133 and the co-OSDA content, y, varying from 0.001 to 0.0133. Crystallization started in a static oven at 125 °C for 1–10 weeks. Increasing aluminum contents in gels required longer durations.

ERI-type zeolite (UZM-12s) were synthesized using commercial OSDA, hexamethonium bromide (HMBr). Desired amount of colloidal silica (Ludox AS-40), pseudoboehmite (Catapal B), potassium hydroxide and TEAOH as the co-OSDA were hydrolyzed in a mixture of water based hexamethonium bromide solution by agitating at room temperature for 24 hours. The final gel composition was 1 SiO_2 : 0.044 Al_2O_3 : 0.063 KOH : 0.813 TEAOH : 0.125 $HMBr_2$: 29.563 H_2O. After being stirred to be homogenized, the synthesis mixture was charged into Teflon-lined 40-mL autoclaves and heated at 100 °C, with rotating (60 rpm), for 7–14 days. The final catalysts obtained had variations, but were obtained with a Si/Al ratio of approximately ~5 (by SEM-EDS analysis).

AEI-type zeolites (SSZ-39s) were synthesized by converting commercial Y zeolite using a one-to-one-ratio *cis*/*trans* mixture of N,N,3,5-tetramethylpiperidinium hydroxide (TMPOH) as the OSDA.[16] Desired amounts of NaOH, fumed silica, OSDA, and deionized water were mixed in a PTFE liner and homogenized by vigorous agitation of magnetic stirring bar. Next, a desired amount of Zeolyst CBV500 was dispersed in the mixture. Further aging steps at room temperature did not influence the results and the step progressed for 24 hours to be homogenized. The final gel composition was 1 SiO_2 : x Al_2O_3 : 0.14 OSDA : 0.57 NaOH : 28 H_2O where the alumina content, x, was varied from 0.005 to 0.05. The crystallization was performed in a 140 °C rotating oven under rotation (60 rpm) and finished when all as-synthesized gel aliquots were identified as AEI zeolite structure.

STI-type zeolites (TNU-10s) were made in the presence of 1,4-bis(N-methylpyrrolidinium)butane dihydroxide (1,4-MPB$(OH)_2$) using gels prepared by combining sodium hydroxide, sodium fluoride, aluminum nitrate ($Al(NO_3)_3 \cdot 9H_2O$), fumed silica, and deionized water. The final composition of the synthesis mixture was 1 SiO_2 : x Al_2O_3 : 0.15 OSDA : 0.7 NaOH : 0.3 NaF : 40 H_2O where the alumina content, x, was varied from 0.008 to 0.017. After stirring at room temperature for 24 hours, the final synthesis mixture was transferred to 40 mL PTFE liners, sealed in autoclaves and heated at 160 °C under rotation (60 rpm) for 7–14 days.

Section 3

Characterization of Materials

Powder X-ray Diffraction (PXRD) Profiles of synthesized zeolite catalysts

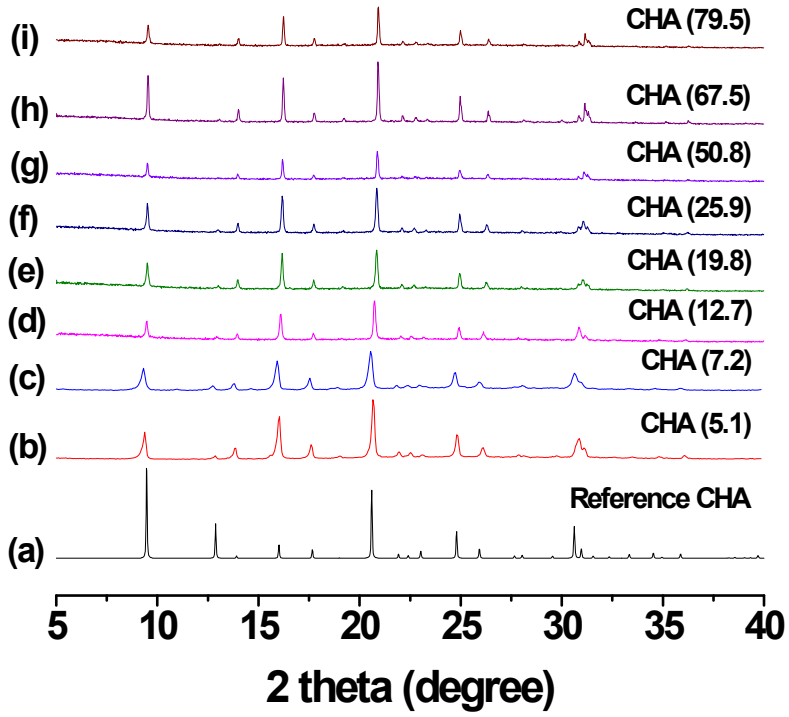

Fig S4. PXRD profiles of CHA type catalysts. The Si/Al ratio of each catalyst is given in parentheses except a profile of reference sample: (a) Reference CHA, (b) CHA (5.1), (c) CHA (7.2), (d) CHA (12.7), (e) CHA (19.8), (f) CHA (25.9), (g) CHA (50.8), (h) CHA (67.5), and (i) CHA (79.5).

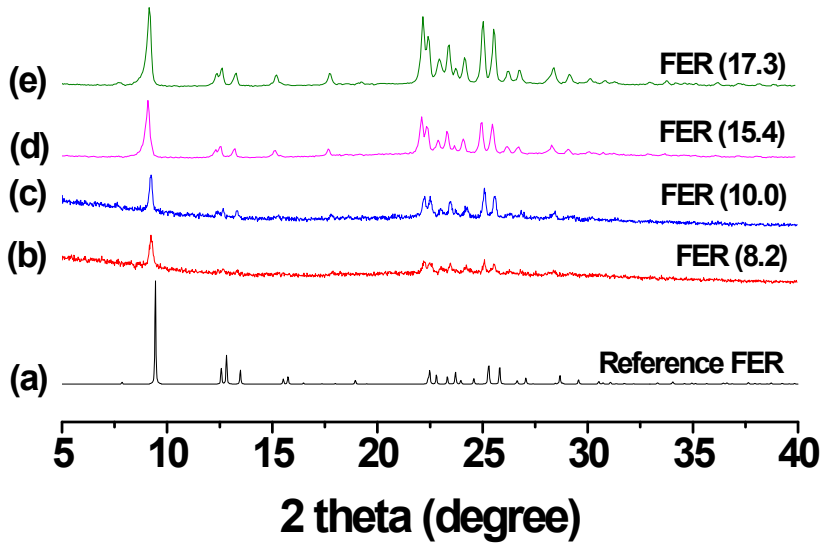

Fig S5. PXRD profiles of FER type catalysts. The Si/Al ratio of each catalyst is given in parentheses except a profile of reference sample: (a) Reference FER, (b) FER (8.2), (c) FER (10.0), (d) FER (15.4), and (e) FER (17.3).

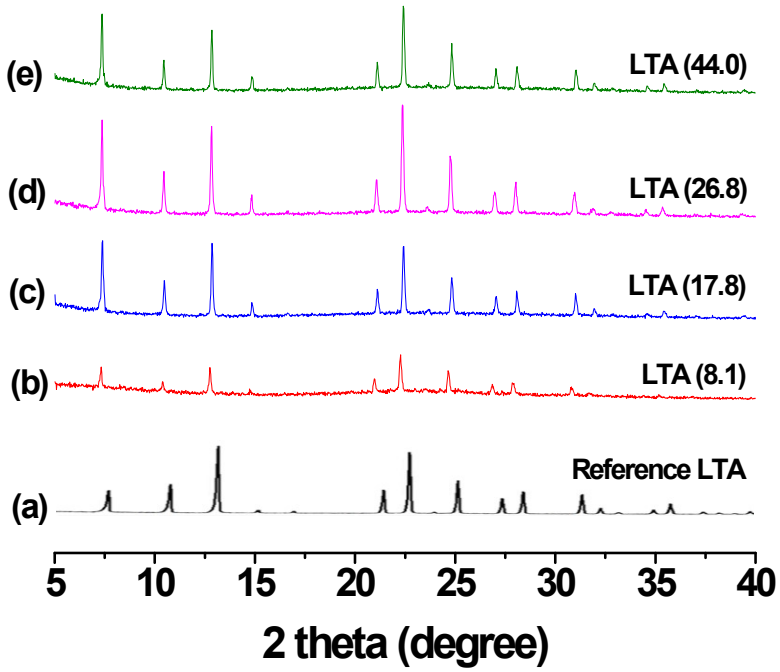

Fig S6. PXRD profiles of LTA type catalysts. The Si/Al ratio of each catalyst is given in parentheses except a profile of reference sample: (a) Reference LTA, (b) LTA (8.1), (c) LTA (17.8), (d) LTA (26.8), and (e) LTA (44.0).

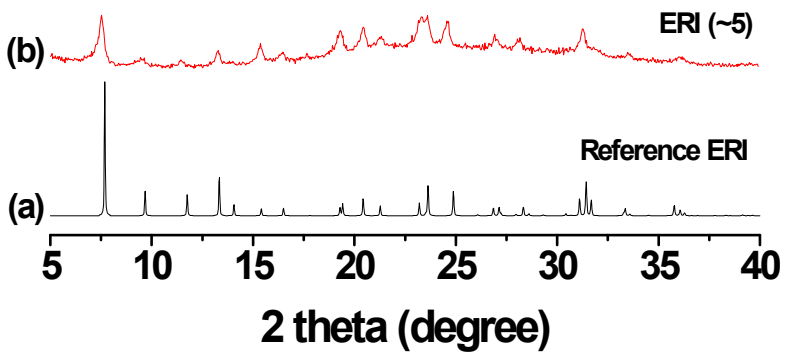

Fig S7. PXRD profiles of ERI type catalysts. The Si/Al ratio of each catalyst is given in parentheses except a profile of reference sample: (a) Reference ERI, and (b) ERI (~5).

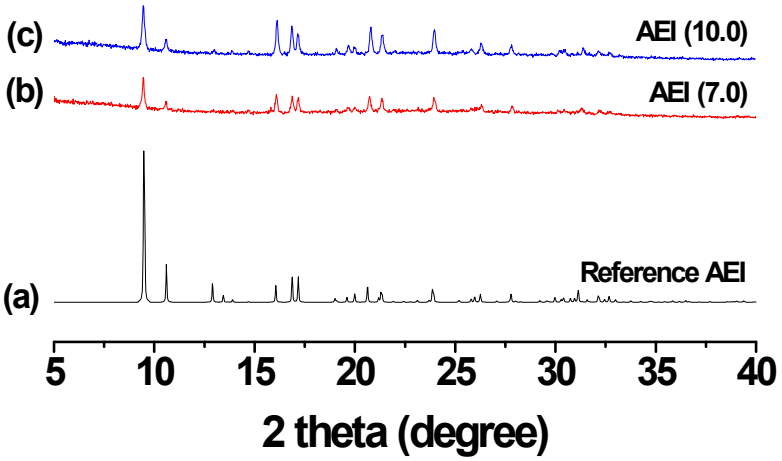

Fig S8. PXRD profiles of AEI type catalysts. The Si/Al ratio of each catalyst is given in parentheses except a profile of reference sample: (a) Reference AEI, (b) AEI (7.0), and (c) AEI (10.0).

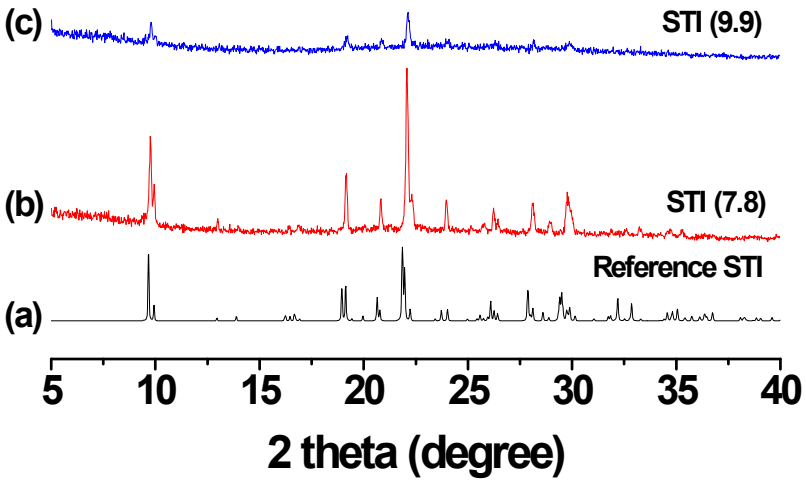

Fig S9. PXRD profiles of STI type catalysts. The Si/Al ratio of each catalyst is given in parentheses except a profile of reference sample: (a) Reference STI, (b) STI (7.8), and (c) STI (9.9).

Scanning Electron Microscope (SEM) Images

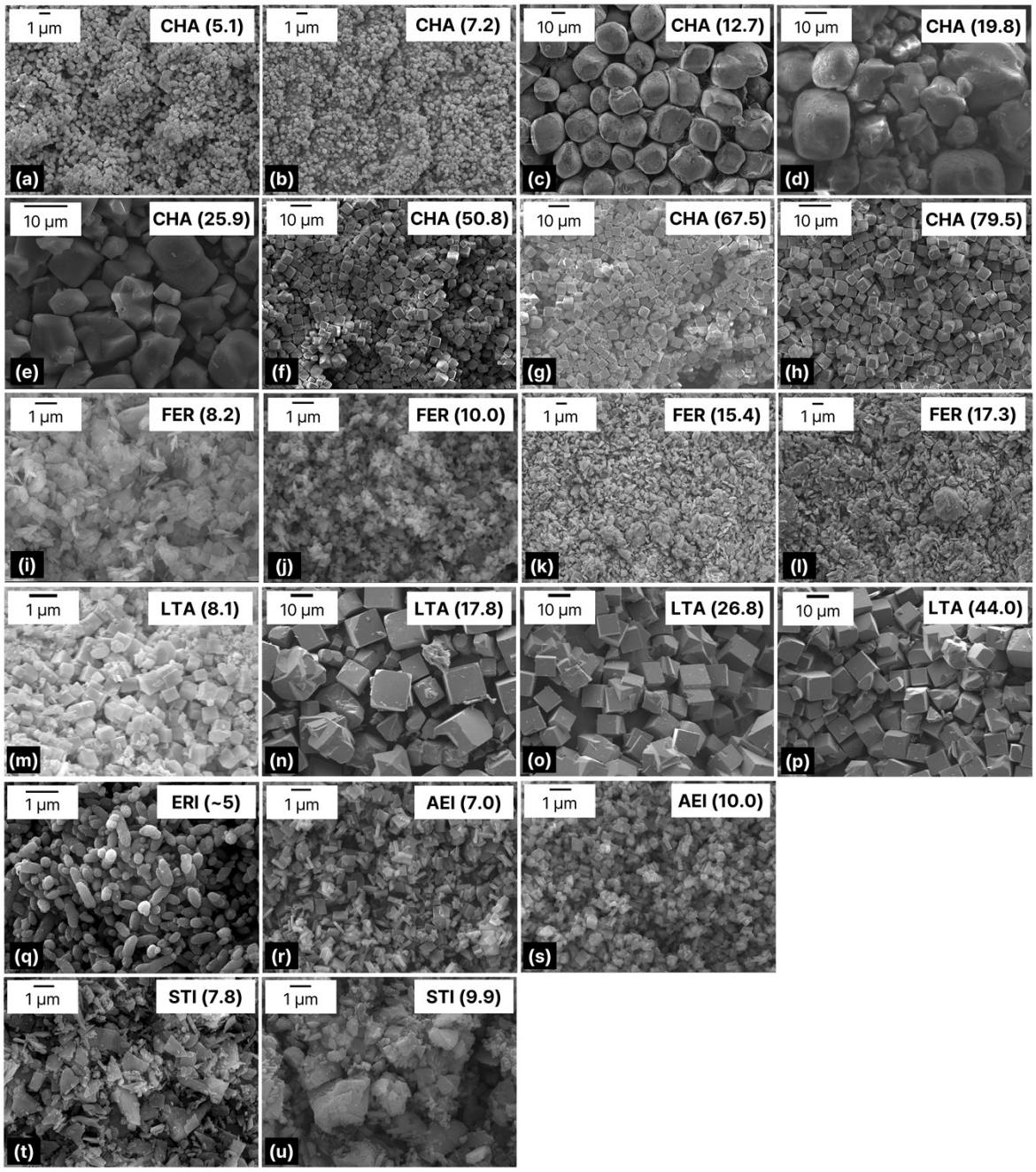

Fig S10. Scanning Electron Microscope images of the catalysts shown in this work, the Si/Al ratio of each catalyst is given in parentheses: (a) CHA (5.1), (b) CHA (7.2), (c) CHA (12.7), (d) CHA (19.8), (e) CHA (25.9), (f) CHA (50.8), (g) CHA (67.5), (h) CHA (79.5), (i) FER (8.2), (j) FER (10.0), (k) FER (15.4), (l) FER (17.3), (m) LTA (8.1), (n) LTA (17.8), (o) LTA (26.8), (p) LTA (44.0), (q) ERI (~5), (r) AEI (7.0), (s) AEI (10.0), (t) STI (7.8), and (u) STI (9.9).

BET analyses of synthesized zeolite catalysts

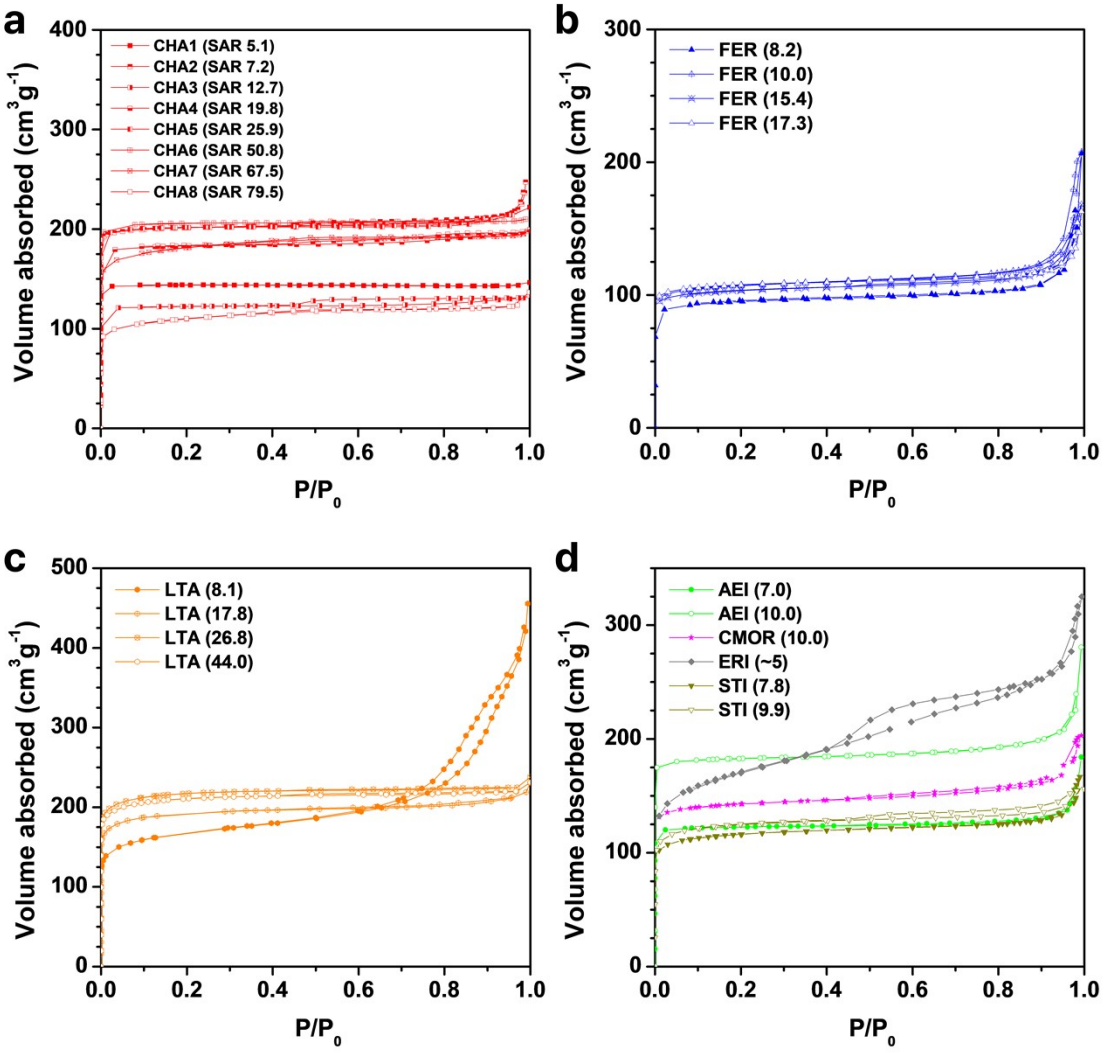

Fig S11. N_2 adsorption-desorption isotherms of investigated zeolite catalysts, the Si/Al ratio of each catalyst is given in parenthese: (a) CHA series, (b) FER series, (c) LTA series, and (d) the others (AEI, CMOR, ERI, and STI).

Table S1. BET surface area, total pore volume (V_{total}), and micro pore volume (V_{micro}) of investigated zeolite catalysts.

Catalysts	BET surface area ($m^2\ g^{-1}$)	V_{total} ($cm^3\ g^{-1}$)	V_{micro} ($cm^3\ g^{-1}$)
CHA (5.1)	605	0.607	0.143
CHA (7.2)	833	0.310	0.265
CHA (12.7)	505	0.382	0.188
CHA (19.8)	756	0.279	0.112
CHA (25.9)	837	0.312	0.172
CHA (50.8)	860	0.319	0.262
CHA (67.5)	712	0.292	0.172
CHA (79.5)	424	0.206	0.091
FER (8.2)	379	0.286	0.117
FER (10.0)	325	0.321	0.143
FER (15.4)	313	0.260	0.140
FER (17.3)	325	0.252	0.147
LTA (8.1)	634	0.660	0.108
LTA (17.8)	756	0.339	0.155
LTA (26.8)	863	0.339	0.196
LTA (44.0)	832	0.327	0.205
ERI (~5)	548	0.503	0.147
AEI (7.0)	512	0.272	0.086
AEI (10.0)	772	0.415	0.231
STI (7.8)	353	0.258	0.149
STI (9.9)	488	0.192	0.109
CMOR (10.0)	430	0.314	0.195

Acid properties of tested zeolite catalysts

NH_3-temperature-programmed desorption (NH_3-TPD) profiles of the selected zeolite catalysts. Each weak, moderate, and strong acid site are deconvoluted by Gauss-Newton algorithm with damped least-squares (DLS) method (3-distribution). Black peak: weak acid, Red peak: moderate acid, Blue peak: strong acid.

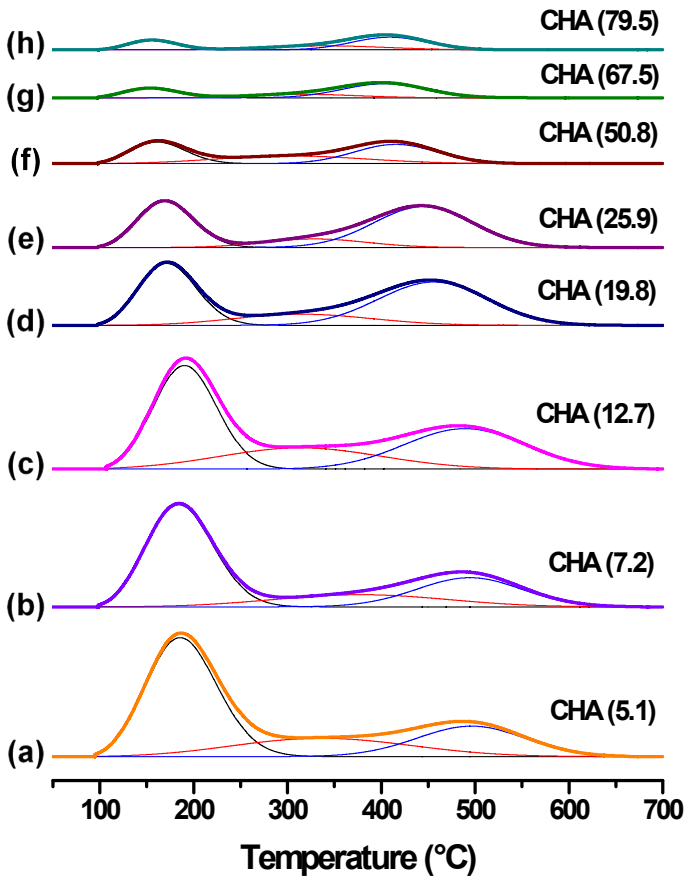

Fig S12. NH_3-TPD profiles of CHA type catalysts: (a) CHA (5.1), (b) CHA (7.2), (c) CHA (12.7), (d) CHA (19.8), (e) CHA (25.9), (f) CHA (50.8), (g) CHA (67.5), and (h) CHA (79.5).

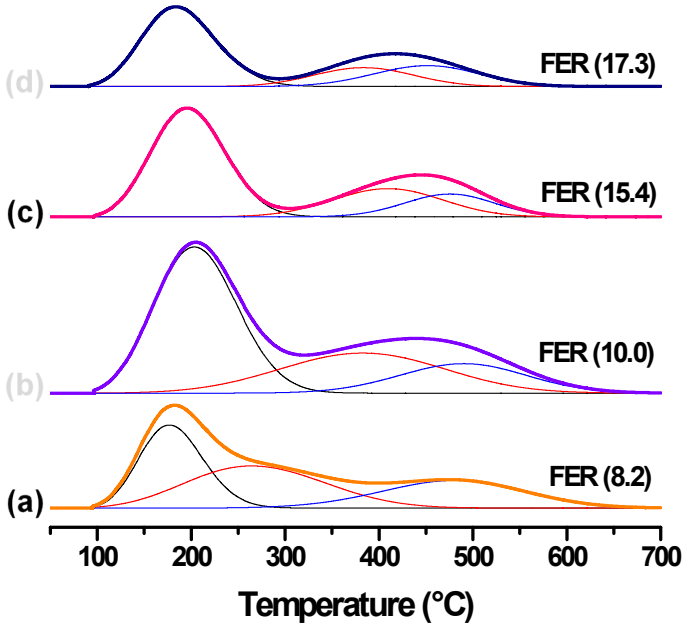

Fig S13. NH_3-TPD profiles of FER type catalysts: (a) FER (8.2), (b) FER (10.0), (c) FER (15.4) and (d) FER (17.3).

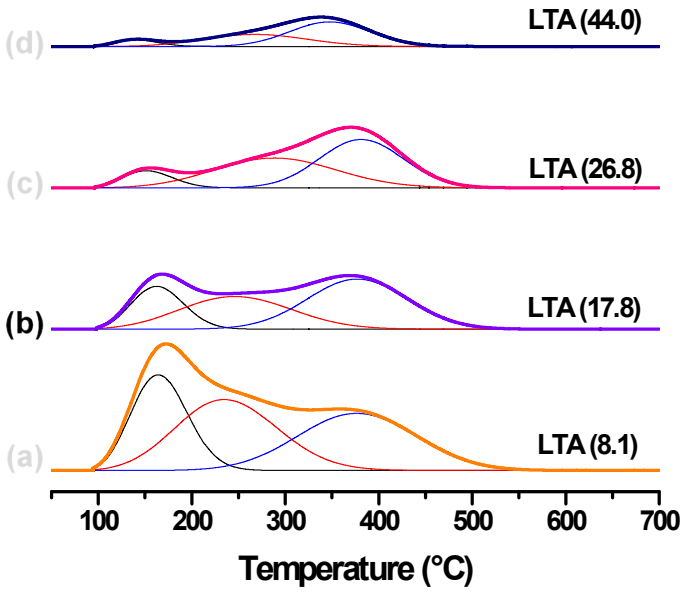

Fig S14. NH_3-TPD profiles of LTA type catalysts: (a) LTA (8.1), (b) LTA (17.8), (c) LTA (26.8), and (d) LTA (44.0).

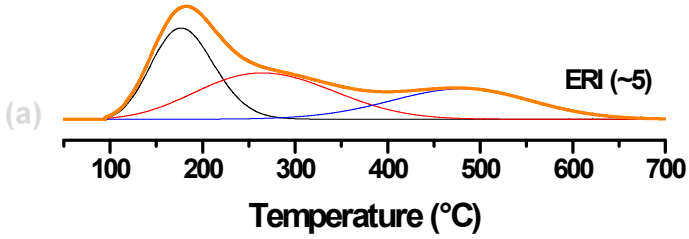

Fig S15. NH_3-TPD profiles of ERI type catalyst: (a) ERI (~5).

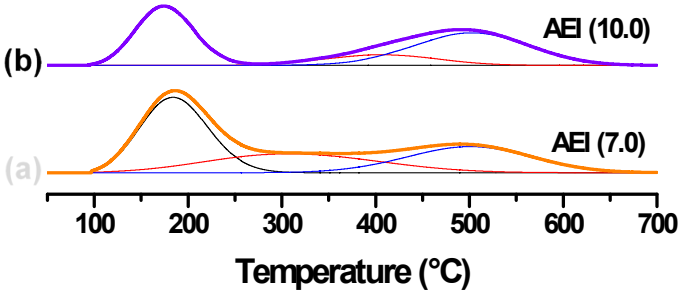

Fig S16. NH_3-TPD profiles of AEI type catalysts: (a) AEI (7.0), and (b) AEI (10.0).

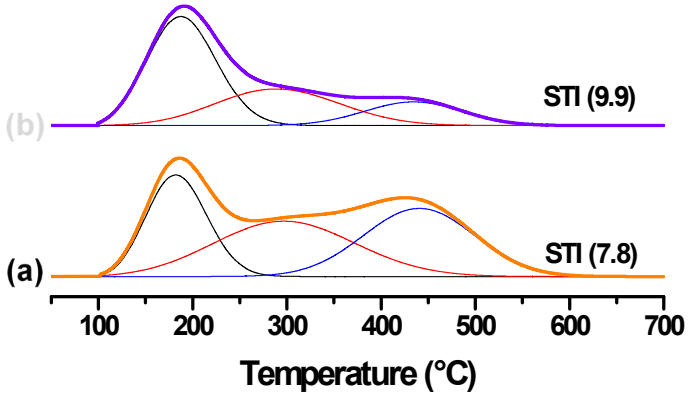

Fig S17. NH_3-TPD profiles of STI type catalysts: (a) STI (7.8), and (b) STI (9.9).

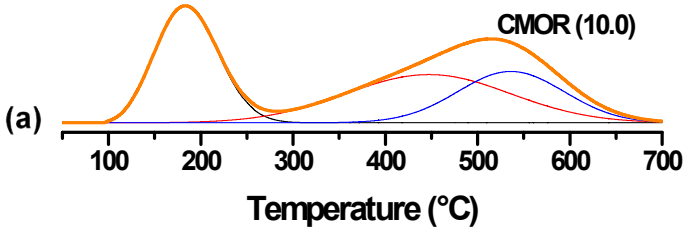

Fig S18. NH_3-TPD profiles of MOR type catalyst: (a) CMOR (10.0) (commercial MOR,).

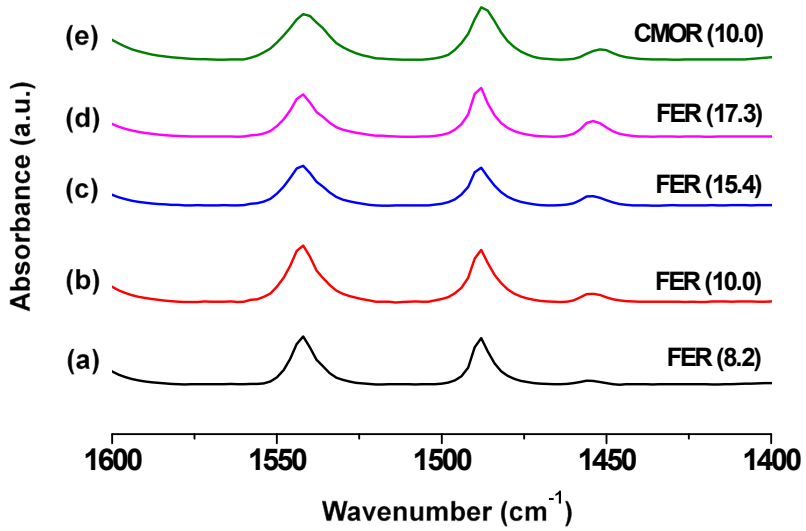

Fig S19. Pyridine Fourier-transform Infrared (Py-IR) absorption spectra of FER and MOR type catalysts at the desorption temperature of 165 °C: (a) FER (8.2), (b) FER (10.0), (c) FER (15.4), (d) FER (17.3), and (e) CMOR (10.0) (commercial MOR,).

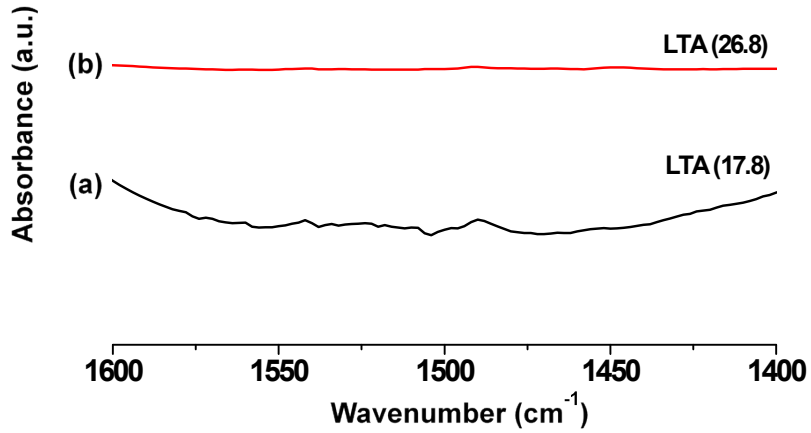

Fig S20. Pyridine Fourier-transform Infrared (Py-IR) absorption spectra of LTA type catalysts at the desorption temperature of 165 °C: (a) LTA (17.8) and LTA (26.8).

Table S2. Acid density properties of selected zeolites. The analysis was primarily conducted via NH_3-TPD. For zeolites possessing larger pores than 8-MR, Py-IR was additionally performed. By subtracting the results from Py-IR from those obtained via NH_3-TPD, the actual 8-MR base density was derived.

Zeolite	NH_3-TPD	Py-IR
	W/M/S (mmol/g)	B/L (mmol/g)
CHA (5.1)	2.477/0.837/0.864	N/A
CHA (7.2)	1.995/0.554/0.822	N/A
CHA (12.7)	1.829/0.933/1.314	N/A
CHA (19.8)	1.141/0.437/1.346	N/A
CHA (25.9)	0.740/0.223/1.030	N/A
CHA (50.8)	0.356/0.306/0.416	N/A
CHA (67.5)	0.170/0.106/0.333	N/A
CHA (79.5)	0.134/0.119/0.231	N/A
FER (8.2)	3.276/0.578/1.097	0.183/0.009
FER (10.0)	2.545/1.304/0.757	0.259/0.019
FER (15.4)	1.666/0.601/0.406	0.193/0.025
FER (17.3)	1.362/0.351/0.418	0.189/0.041
LTA (8.1)	0.662/0.800/0.694	N/A
LTA (17.8)	0.271/0.392/0.544	N/A
LTA (26.8)	0.107/0.532/0.368	N/A
LTA (44.0)	0.038/0.218/0.189	N/A
ERI (~5)	1.239/1.177/0.819	N/A
AEI (7.0)	1.829/0.913/1.389	N/A
AEI (10.0)	1.508/0.433/1.394	N/A
STI (7.8)	0.844/1.006/0.956	N/A
STI (9.9)	1.609/0.887/0.448	N/A
CMOR (10.0)	2.226/2.089/1.644	0.275/0.030

Section 4

The long-term reactivity data for whole reaction time on stream (TOS)

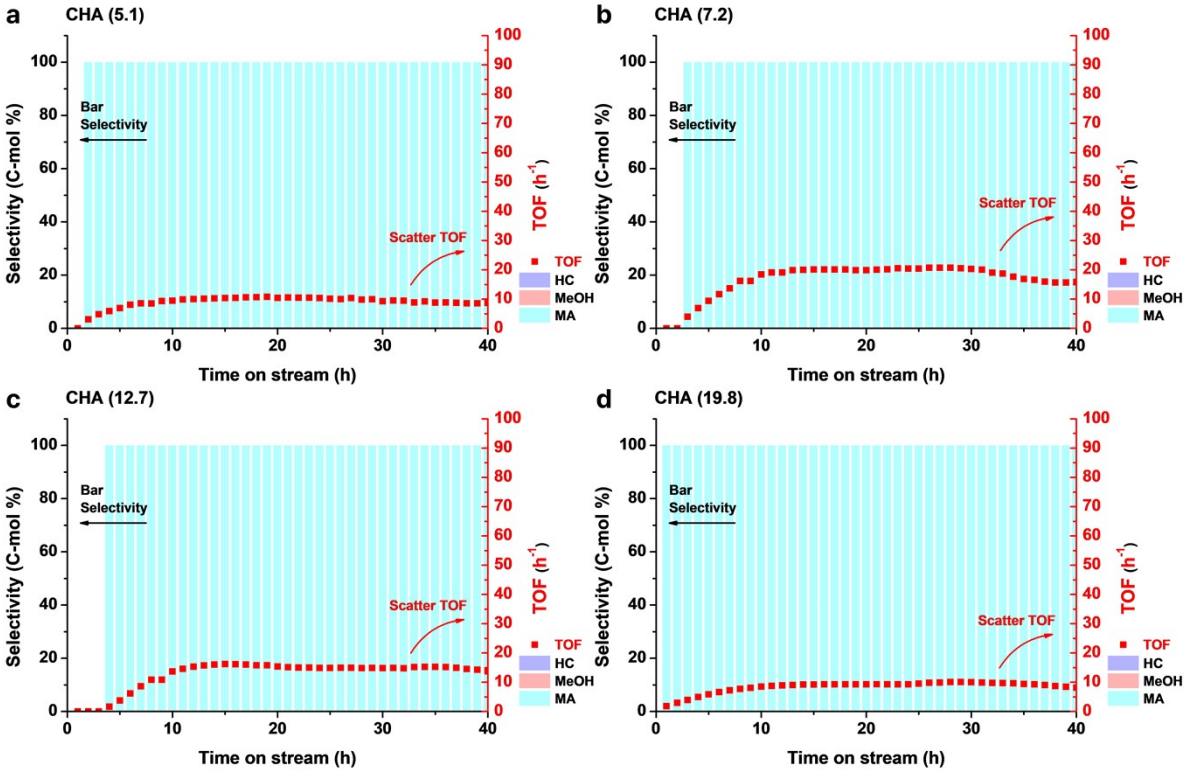

Fig S21. The long-term reactivity profiles for whole reaction time on stream (~40 h) of the investigated catalysts. The scatter plots show turnover frequencies (TOFs) for each of catalysts and the bar charts show selectivity but only generating methyl acetate (MA) with the bar color of cyan (see the legend of product selectivity on the bottom right hand corner: (a) CHA (5.1), (b) CHA (7.2), (c) CHA (12.7), and (d) CHA (19.8).

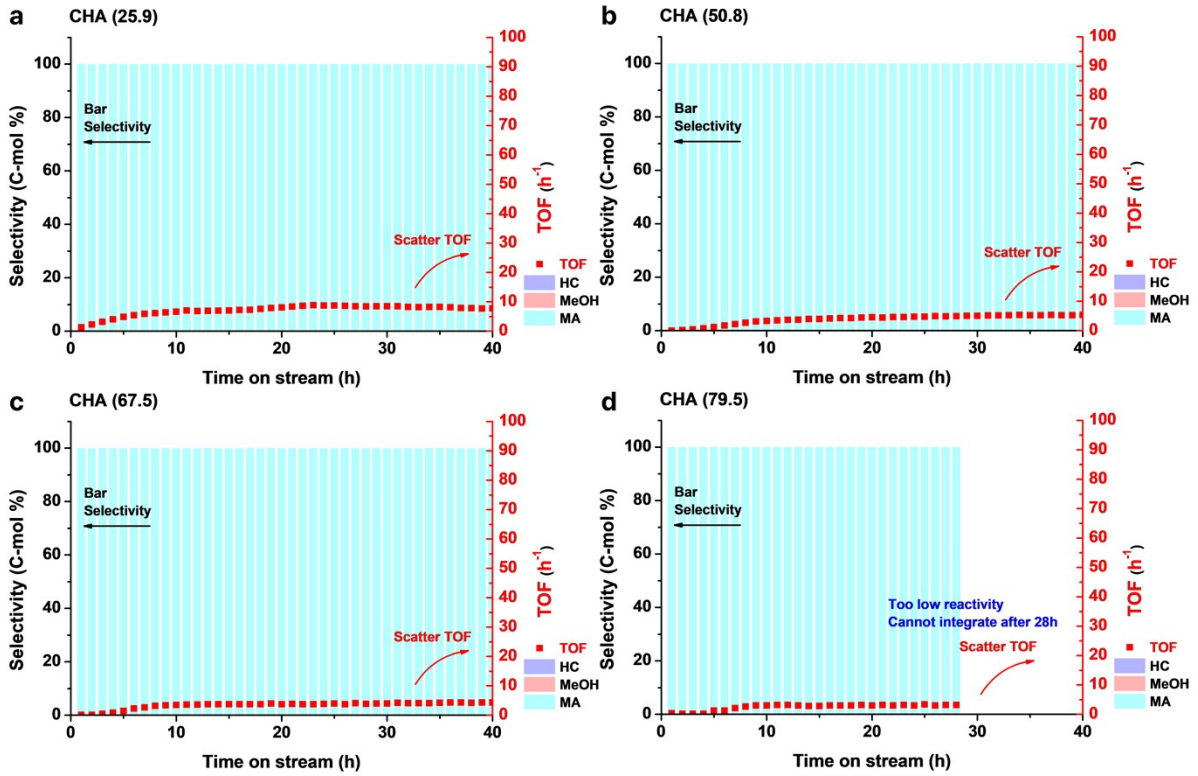

Fig S22. The long-term reactivity profiles for whole reaction time on stream (~40 h) of the investigated catalysts. The scatter plots show turnover frequencies (TOFs) for each of catalysts and the bar charts show selectivity but only generating methyl acetate (MA) with the bar color of cyan (see the legend of product selectivity on the bottom right hand corner: (a) CHA (25.9), (b) CHA (50.8), (c) CHA (67.5), and (d) CHA (79.5).

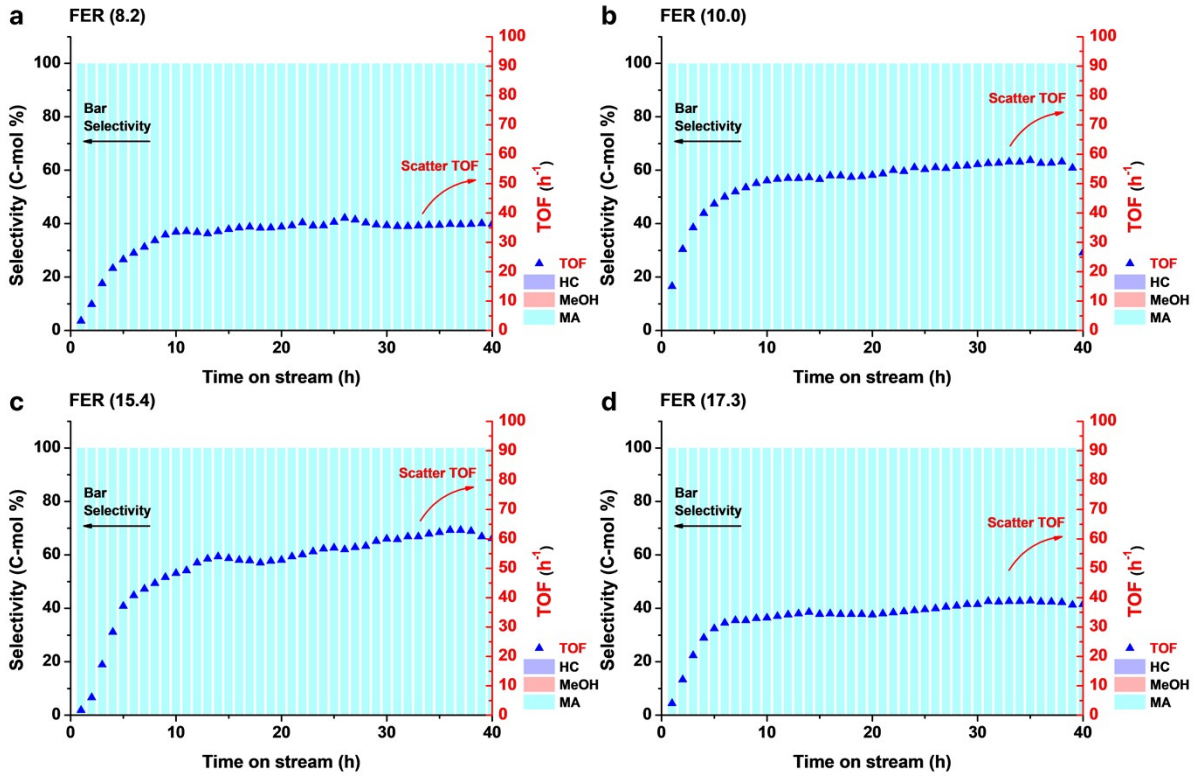

Fig S23. The long-term reactivity profiles for whole reaction time on stream (~40 h) of the investigated catalysts. The scatter plots show turnover frequencies (TOFs) for each of catalysts and the bar charts show selectivity but only generating methyl acetate (MA) with the bar color of cyan (see the legend of product selectivity on the bottom right hand corner: (a) FER (8.2), (b) FER (10.0), (c) FER (15.4), and (d) FER (17.3).

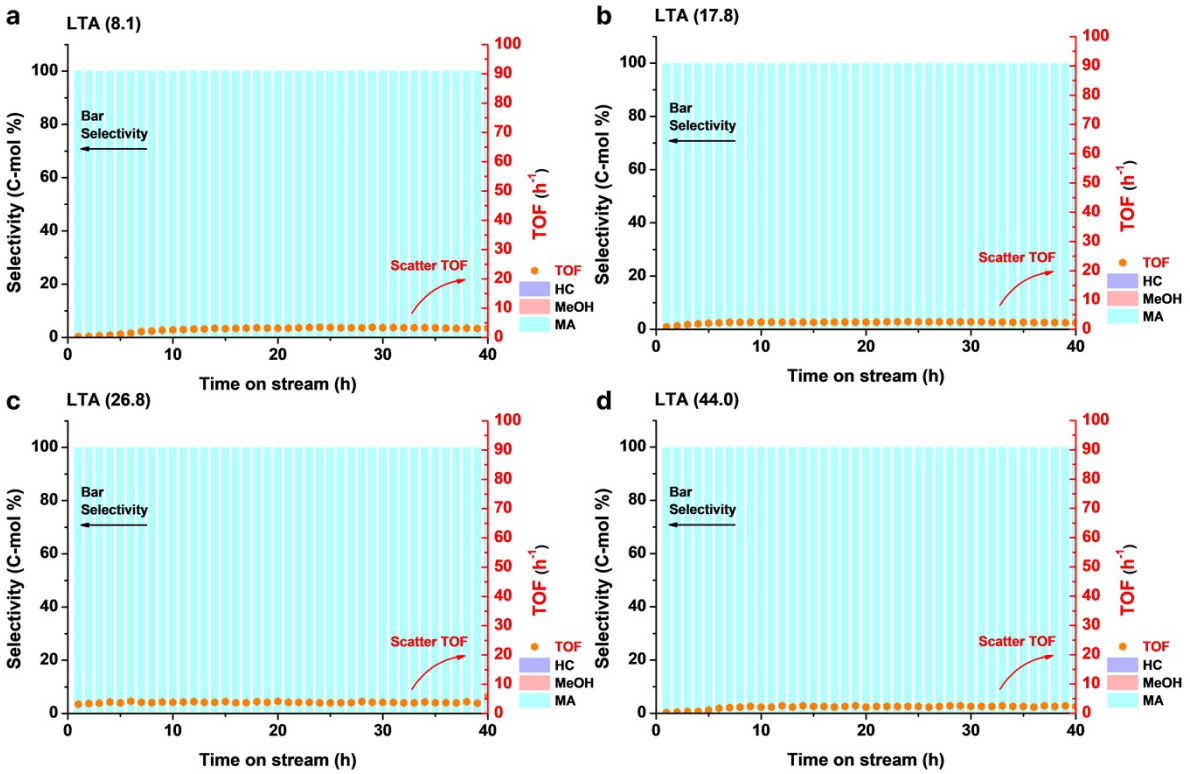

Fig S24. The long-term reactivity profiles for whole reaction time on stream (~40 h) of the investigated catalysts. The scatter plots show turnover frequencies (TOFs) for each of catalysts and the bar charts show selectivity but only generating methyl acetate (MA) with the bar color of cyan (see the legend of product selectivity on the bottom right hand corner: (a) LTA (8.1), (b) LTA (17.8), (c) LTA (26.8), and (d) LTA (44.0).

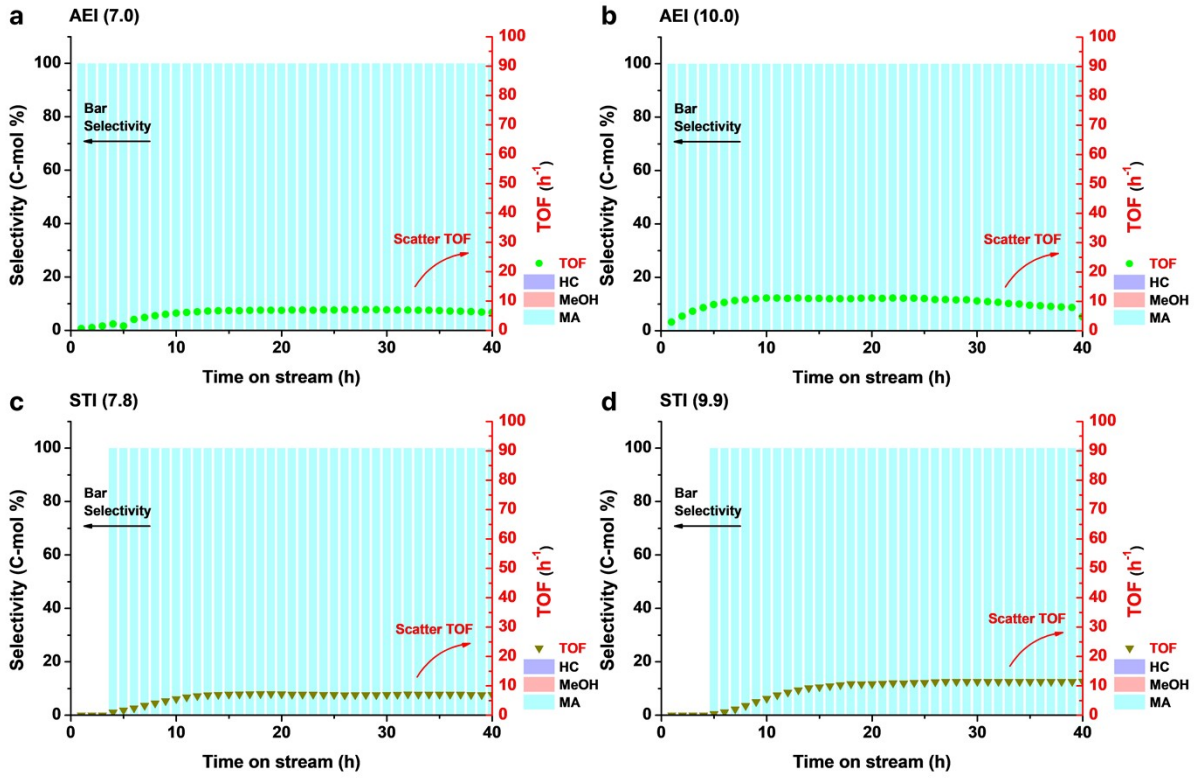

Fig S25. The long-term reactivity profiles for whole reaction time on stream (~40 h) of the investigated catalysts. The scatter plots show turnover frequencies (TOFs) for each of catalysts and the bar charts show selectivity but only generating methyl acetate (MA) with the bar color of cyan (see the legend of product selectivity on the bottom right hand corner: (a) AEI (7.0), (b) AEI (10.0), (c) STI (7.8), and (d) STI (9.9).

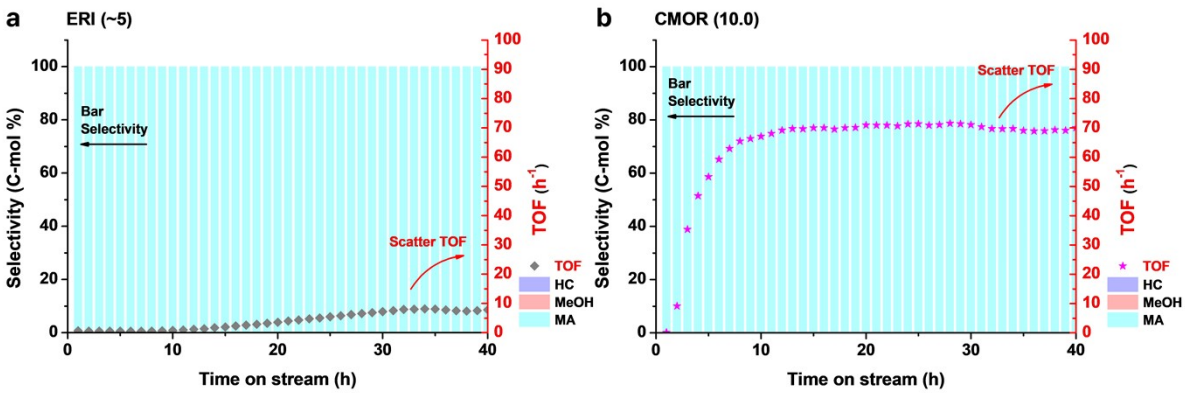

Fig S26. The long-term reactivity profiles for whole reaction time on stream (~40 h) of the investigated catalysts. The scatter plots show turnover frequencies (TOFs) for each of catalysts and the bar charts show selectivity but only generating methyl acetate (MA) with the bar color of cyan (see the legend of product selectivity on the bottom right hand corner: (a) ERI (~5), and (b) CMOR (10.0).

Section 5

Energy descriptor derived from DFT calculation

Energy diagram (methylation step)

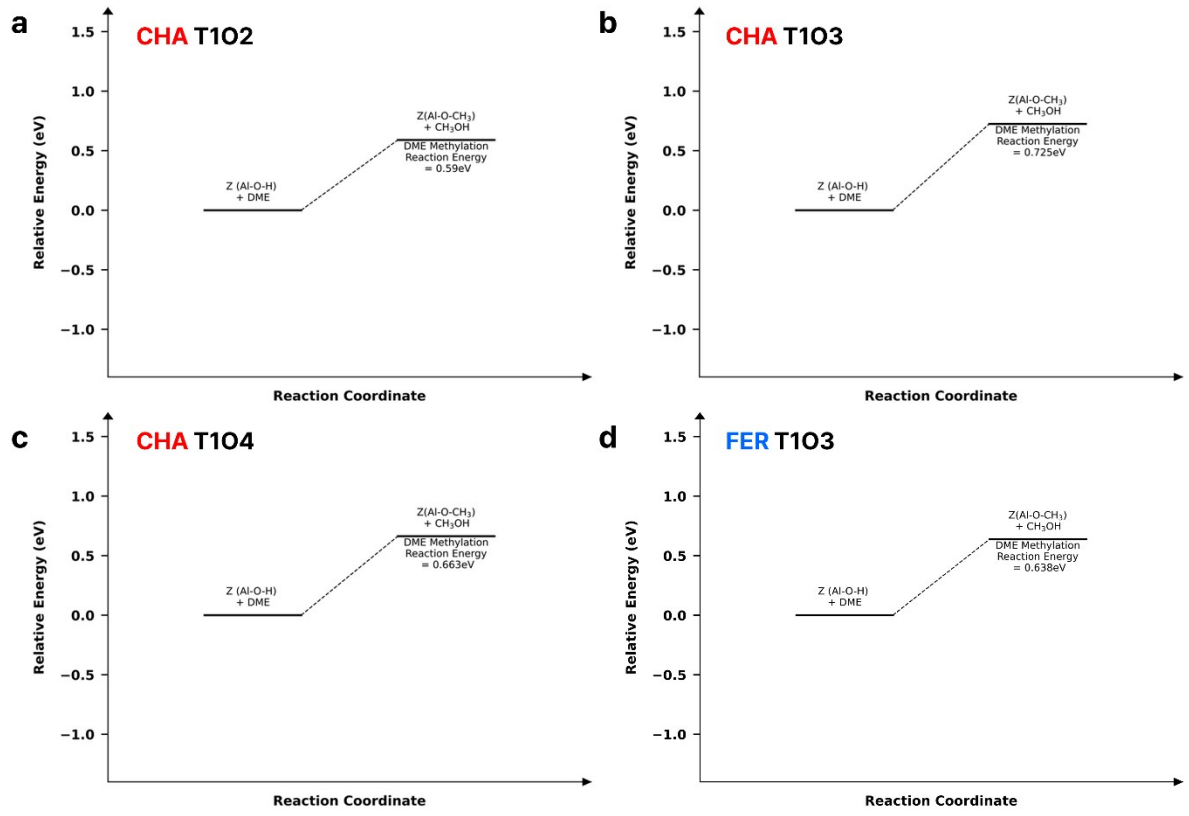

Fig S27. Methylation step energy diagram (reaction enthalpy) for the investigated TxOy site of the selected 8-MR zeolites: (a) CHA T1O2, (b) CHA T1O3, (c) CHA T1O4, and (d) FER T1O3.

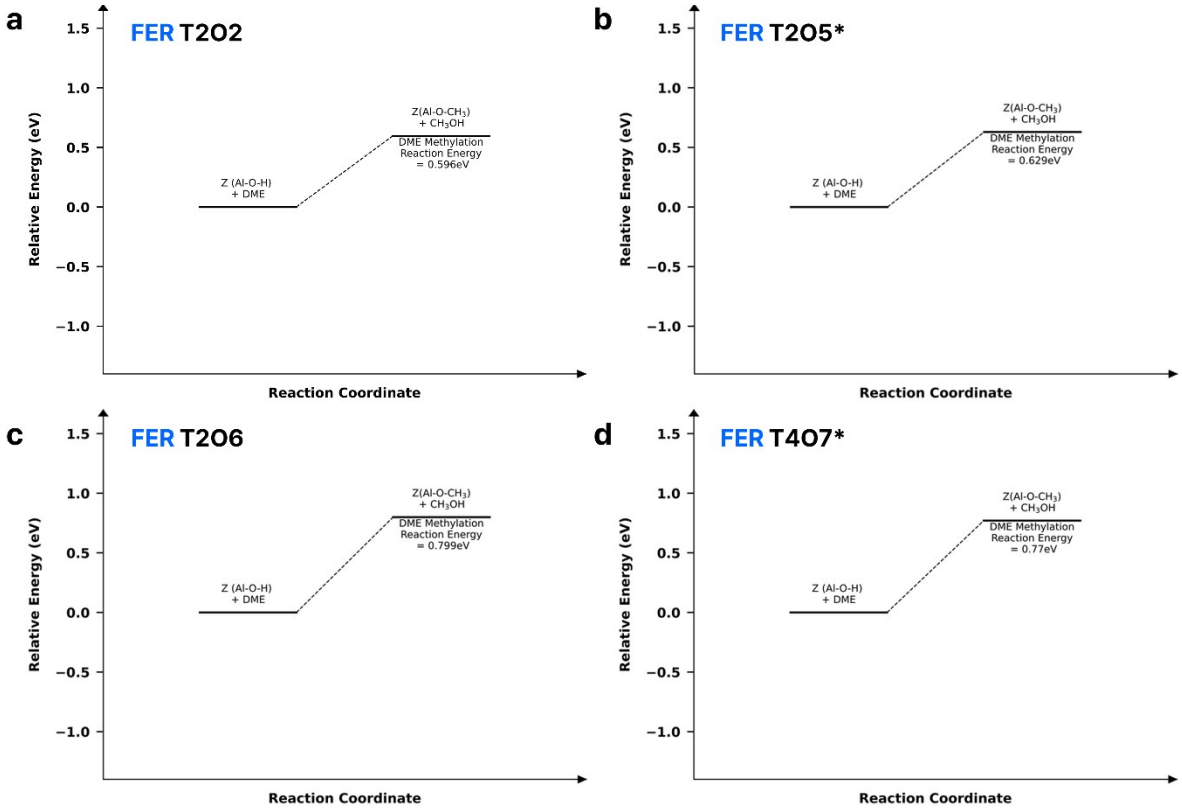

Fig S28. Methylation step energy diagram (reaction enthalpy) for the investigated TxOy site of the selected 8-MR zeolites: (a) FER T2O2, (b) FER T2O5, (c) FER T2O6, and (d) FER T4O7.

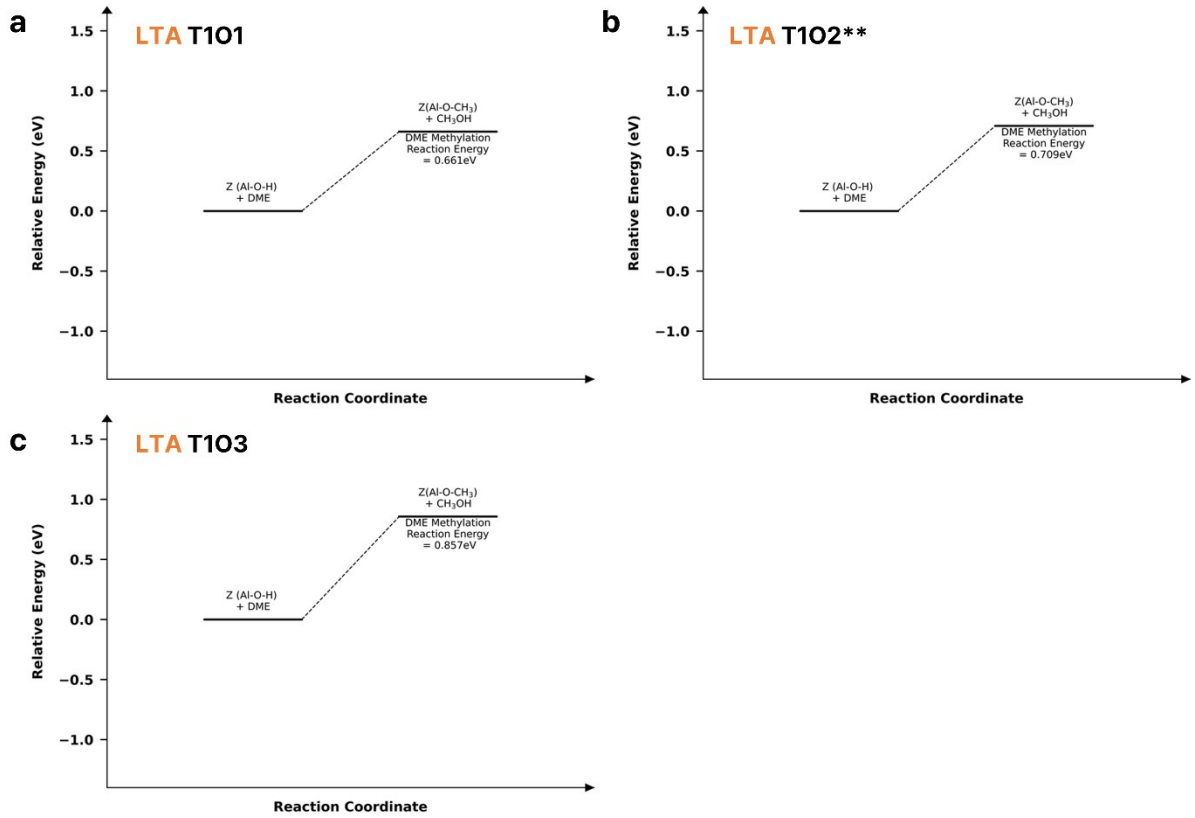

Fig S29. Methylation step energy diagram (reaction enthalpy) for the investigated TxOy site of the selected 8-MR zeolites: (a) LTA T1O1, (b) LTA T1O2, and (c) LTA T1O3.

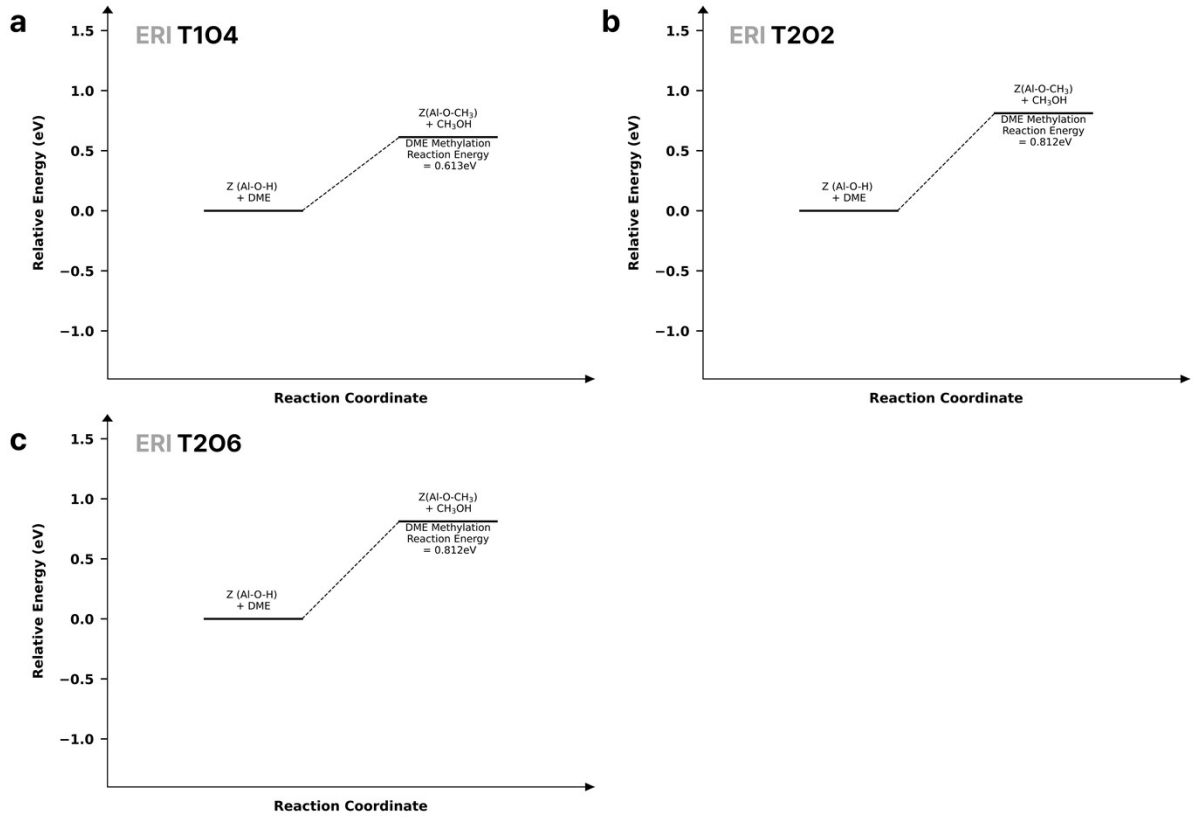

Fig S30. Methylation step energy diagram (reaction enthalpy) for the investigated TxOy site of the selected 8-MR zeolites: (a) ERI T1O4, (b) ERI T2O2, and (c) ERI T2O6

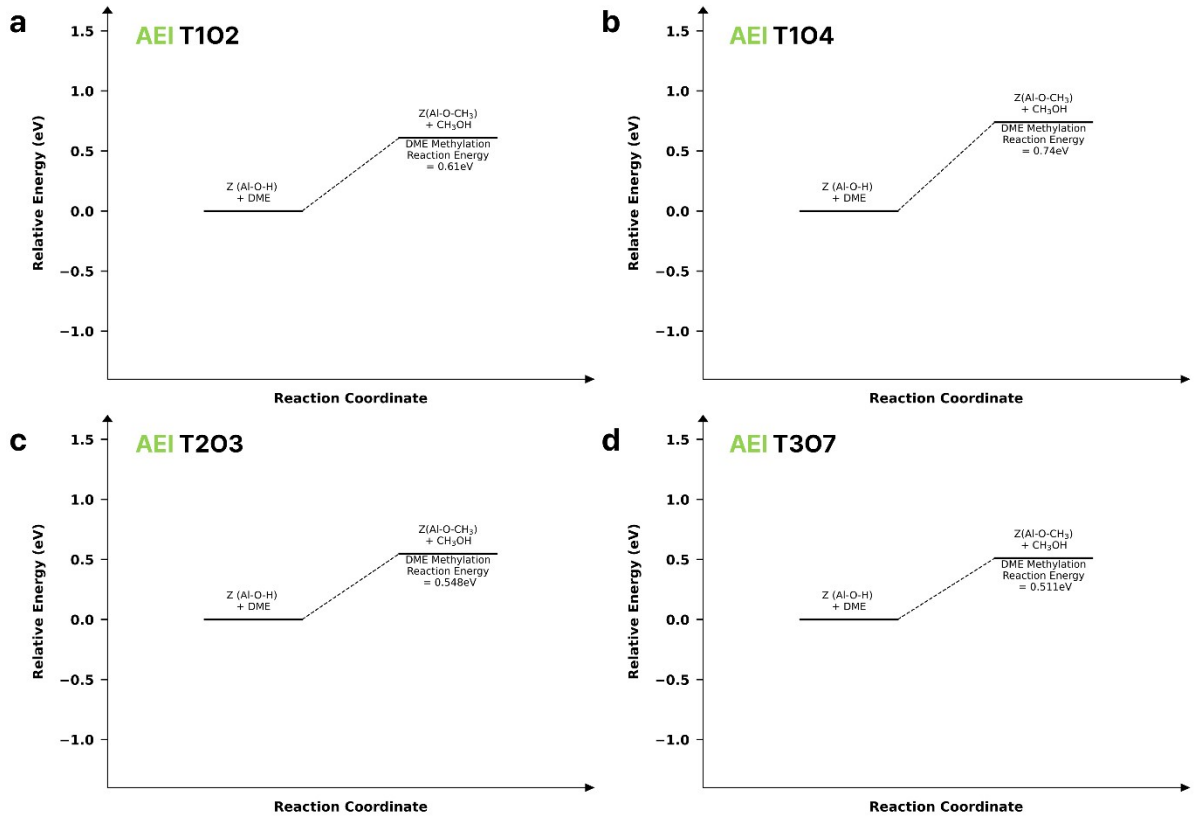

Fig S31. Methylation step energy diagram (reaction enthalpy) for the investigated TxOy site of the selected 8-MR zeolites: (a) AEI T1O2, (b) AEI T1O4, (c) AEI T2O3, and (d) AEI T3O7.

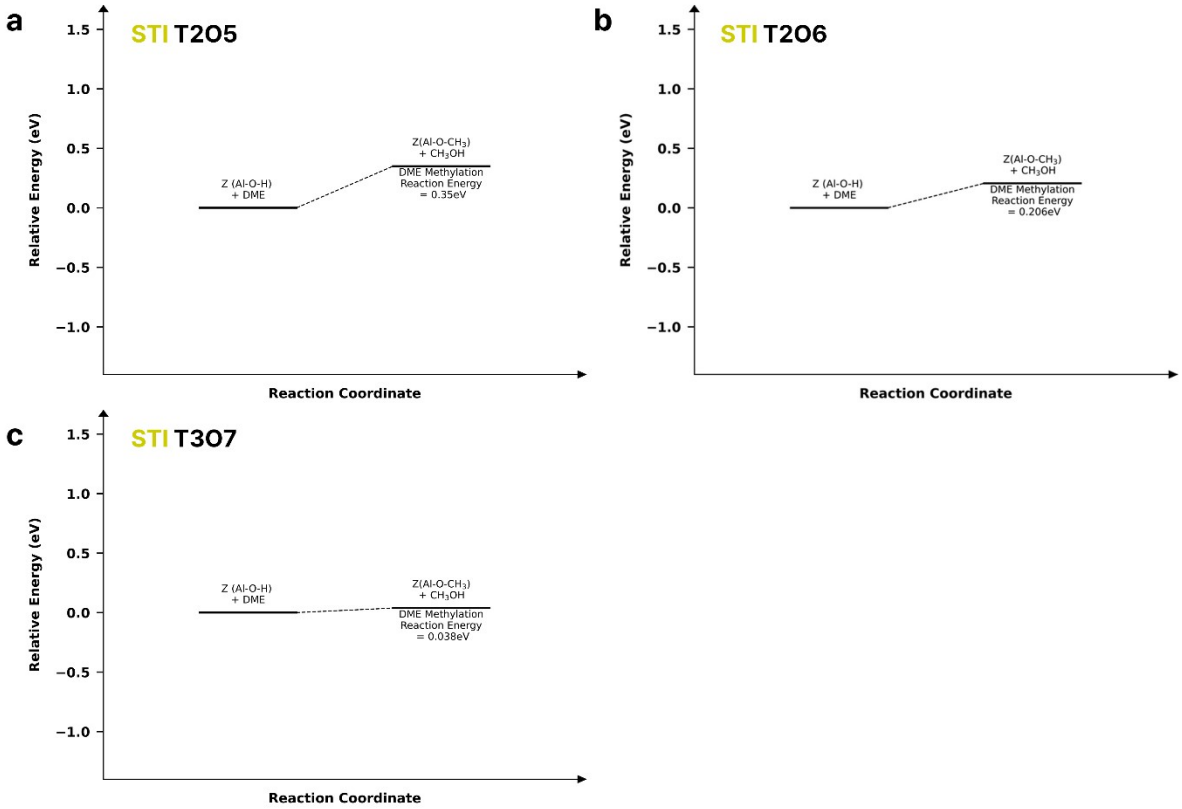

Fig S32. Methylation step energy diagram (reaction enthalpy) for the investigated TxOy site of the selected 8-MR zeolites: (a) STI T2O5, (b) STI T2O6, and (c) STI T3O7.

.

Energy diagram (CO addition step)

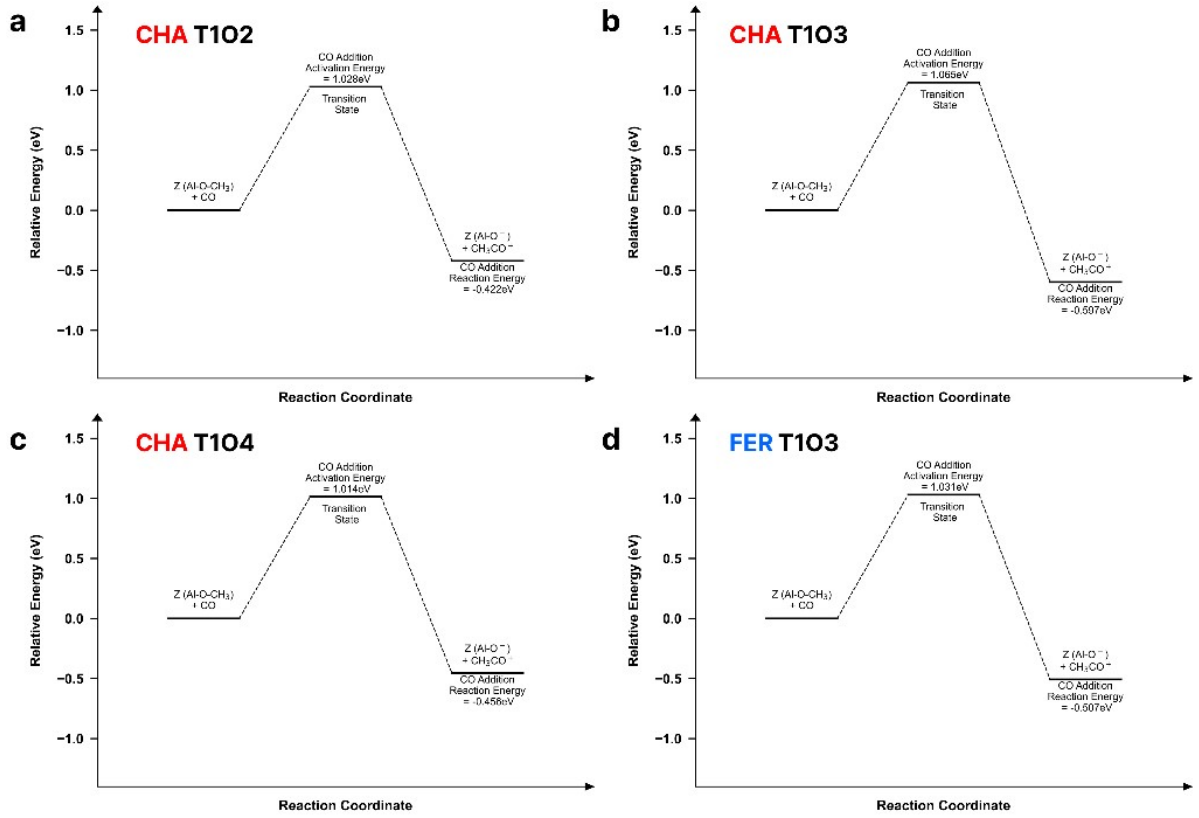

Fig S33. CO addition step energy diagram (reaction enthalpy and activation energy) for the investigated TxOy site of the selected 8-MR zeolites: (a) CHA T1O2, (b) CHA T1O3, (c) CHA T1O4, and (d) FER T1O3.

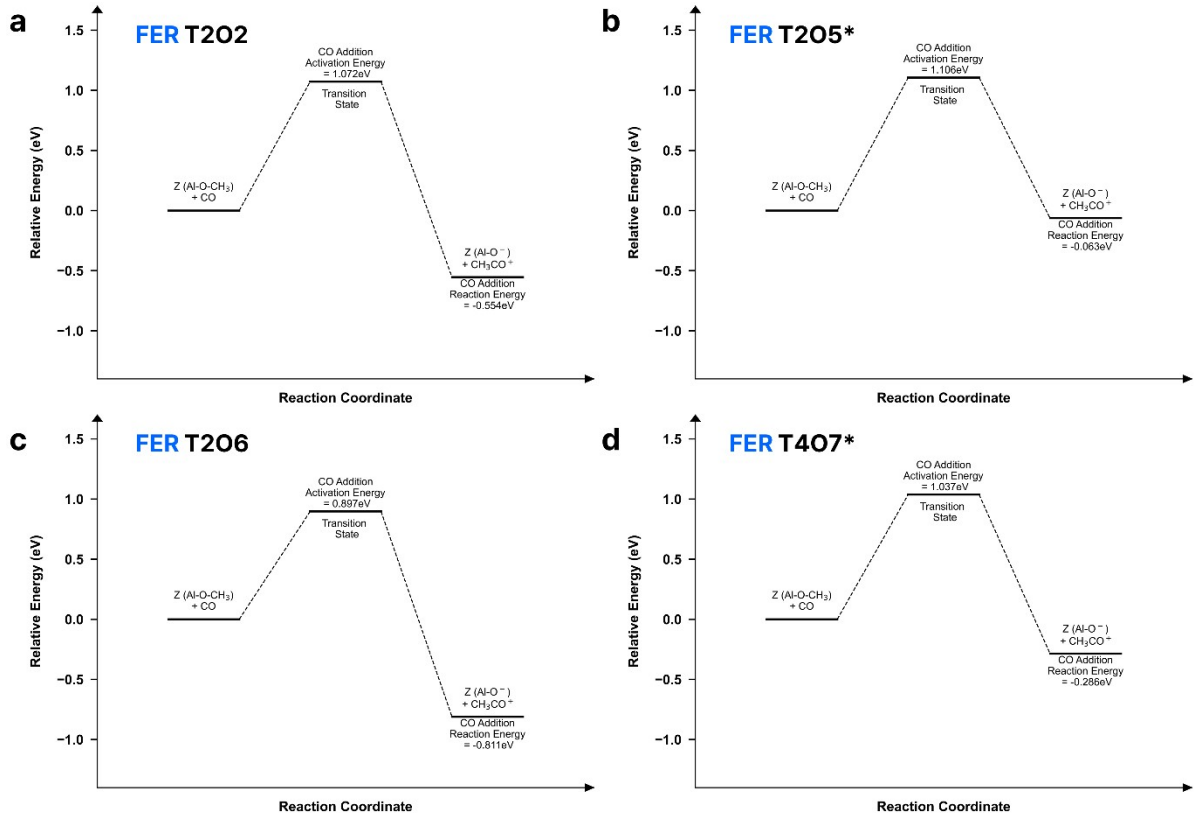

Fig S34. CO addition step energy diagram (reaction enthalpy and activation energy) for the investigated TxOy site of the selected 8-MR zeolites: (a) FER T2O2, (b) FER T2O5, (c) FER T2O6, and (d) FER T4O7.

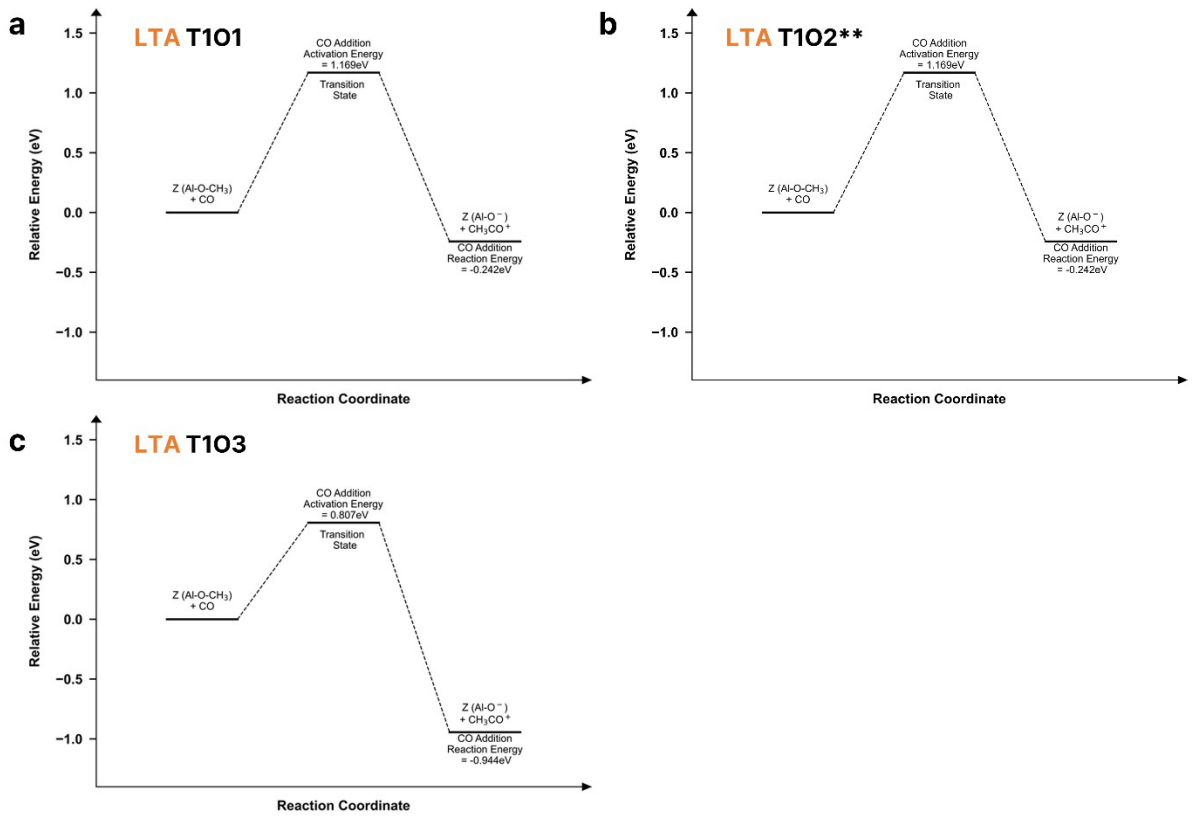

Fig S35. CO addition step energy diagram (reaction enthalpy and activation energy) for the investigated TxOy site of the selected 8-MR zeolites: (a) LTA T1O1, (b) LTA T1O2, and (c) LTA T1O3.

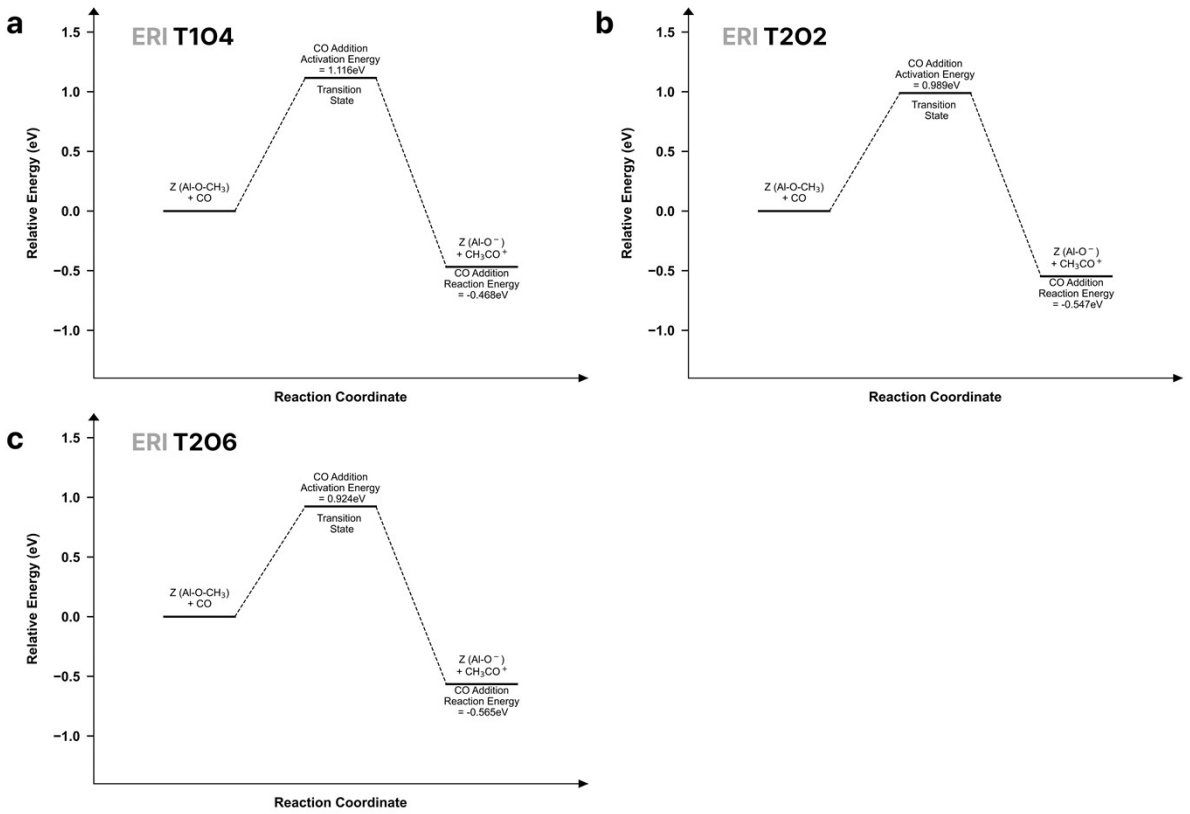

Fig S36. CO addition step energy diagram (reaction enthalpy and activation energy) for the investigated TxOy site of the selected 8-MR zeolites: (a) ERI T1O4, (b) ERI T2O2, and (c) ERI T2O6.

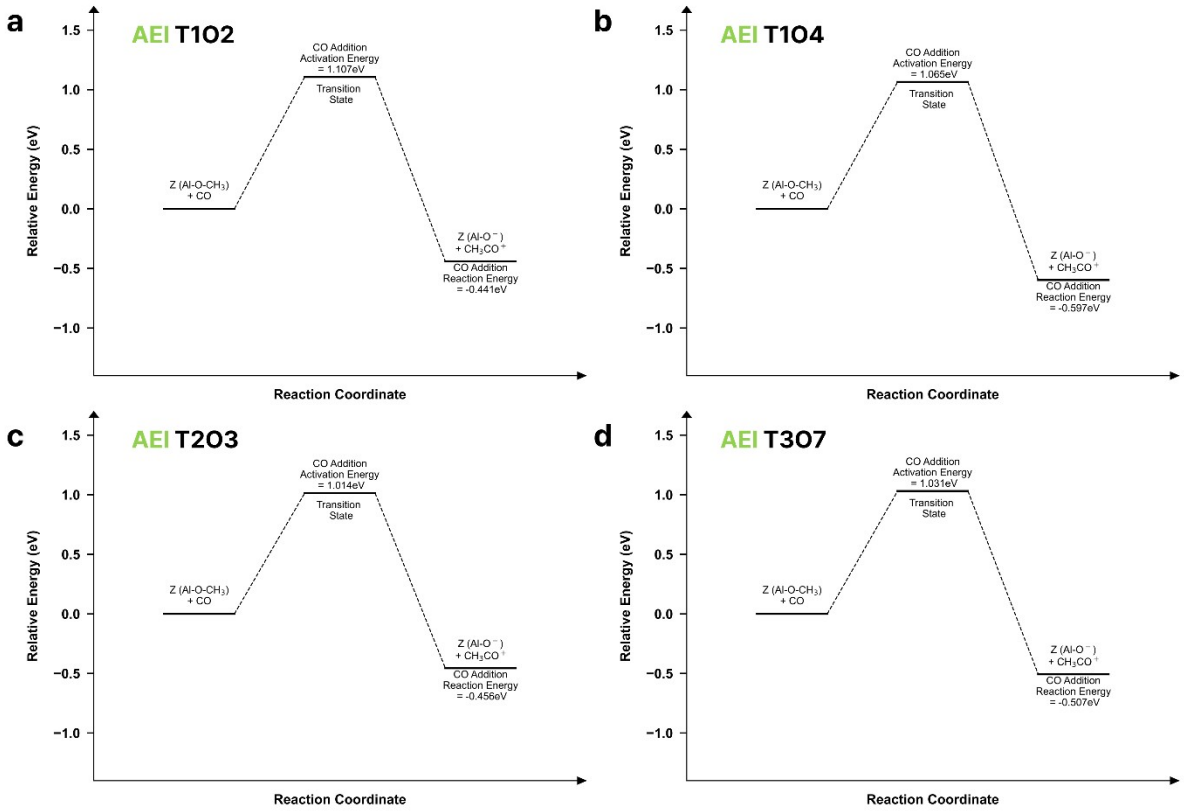

Fig S37. CO addition step energy diagram (reaction enthalpy and activation energy) for the investigated TxOy site of the selected 8-MR zeolites: (a) AEI T1O2, (b) AEI T1O4, (c) AEI T2O3, and (d) AEI T3O7.

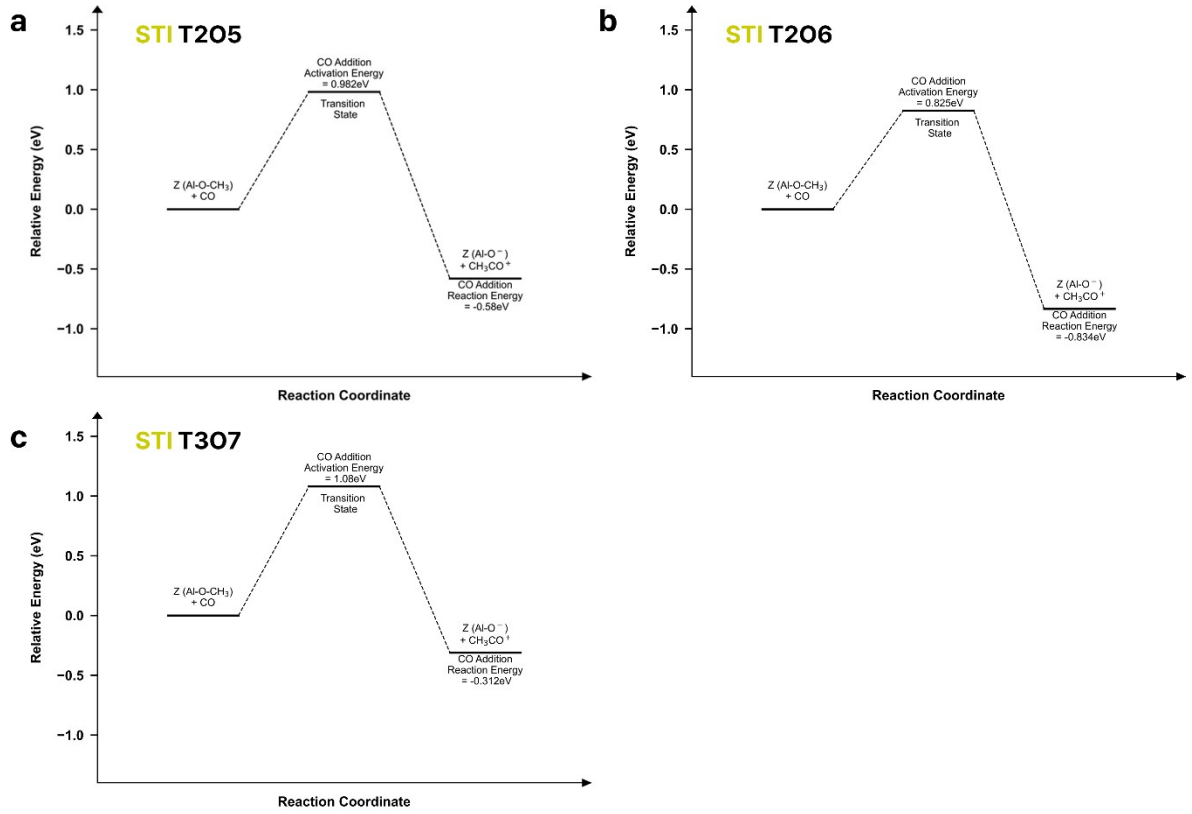

Fig S38. CO addition step energy diagram (reaction enthalpy and activation energy) for the investigated TxOy site of the selected 8-MR zeolites: (a) STI T2O5, (b) STI T2O6, and (c) STI T3O7.

Energy diagram (H_2O addition step for SI Section 6)

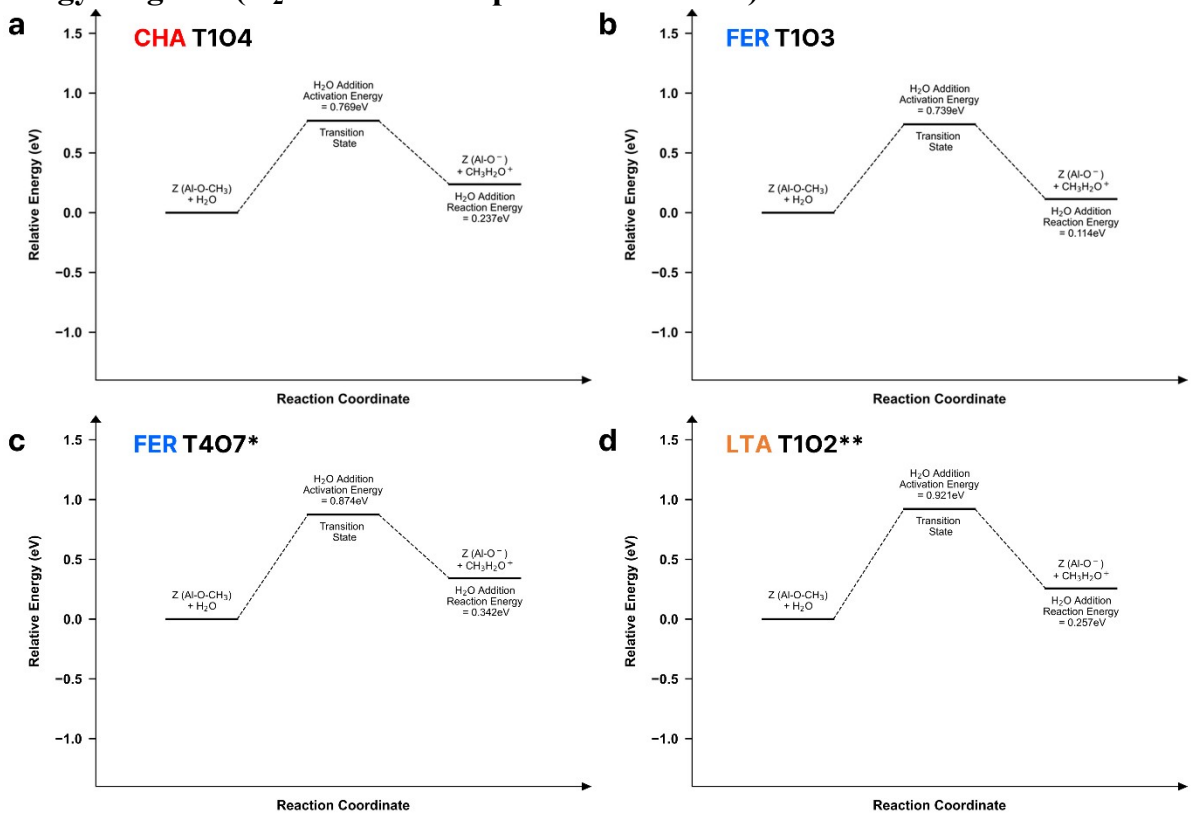

Fig S39. H_2O addition step (competitive reaction of CO addition) energy diagram (reaction enthalpy and activation energy) for the investigated TxOy site of the selected 8-MR zeolites: (a) CHA T1O4, (b) FER T1O3, (c) FER T4O7, and (d) LTA T1O2.

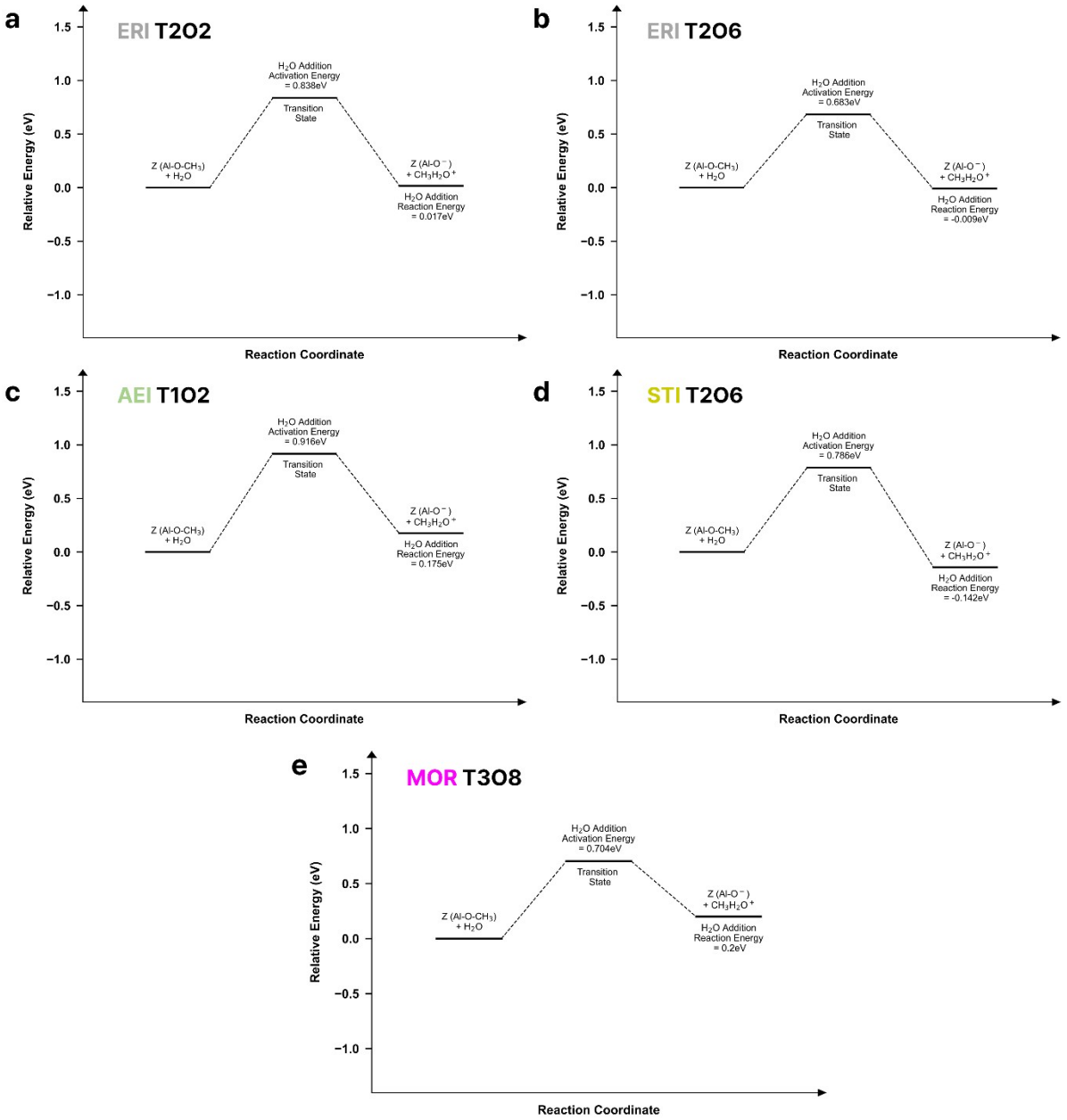

Fig S40. H_2O addition step (competitive reaction of CO addition) energy diagram (reaction enthalpy and activation energy) for the investigated TxOy site of the selected 8-MR zeolites: (a) ERI T2O2, (b) ERI T2O6, (c) AEI T1O2, (d) STI T2O6, and MOR T3O8.

Energy diagram (full scheme of DME carbonylation process)

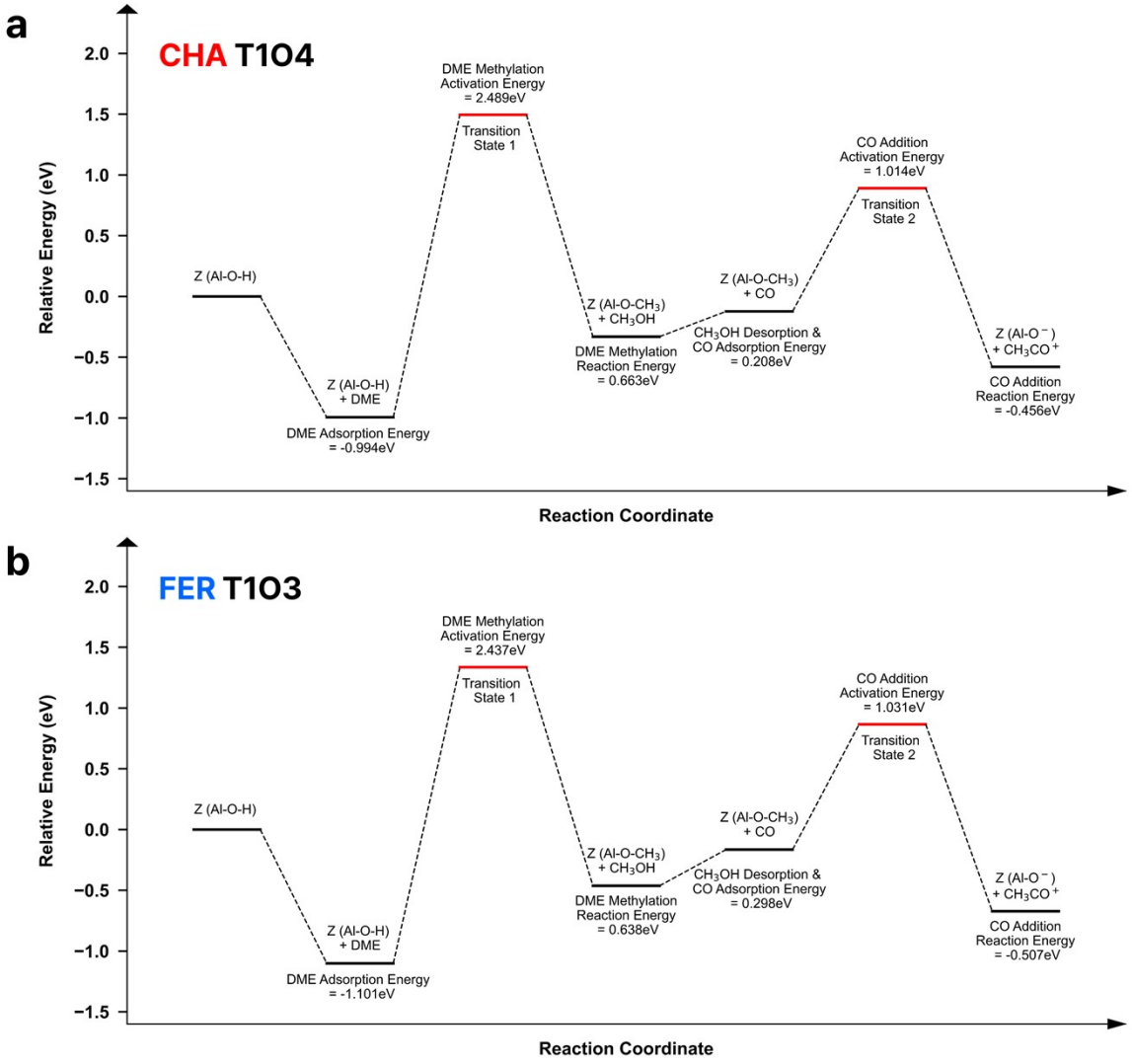

Fig S41. Full scheme of two key steps on DME carbonylation (methylation and CO addition step) energy diagram for some investigated TxOy site of the selected 8-MR zeolites: (a) CHA T1O4, (b) FER T1O3.

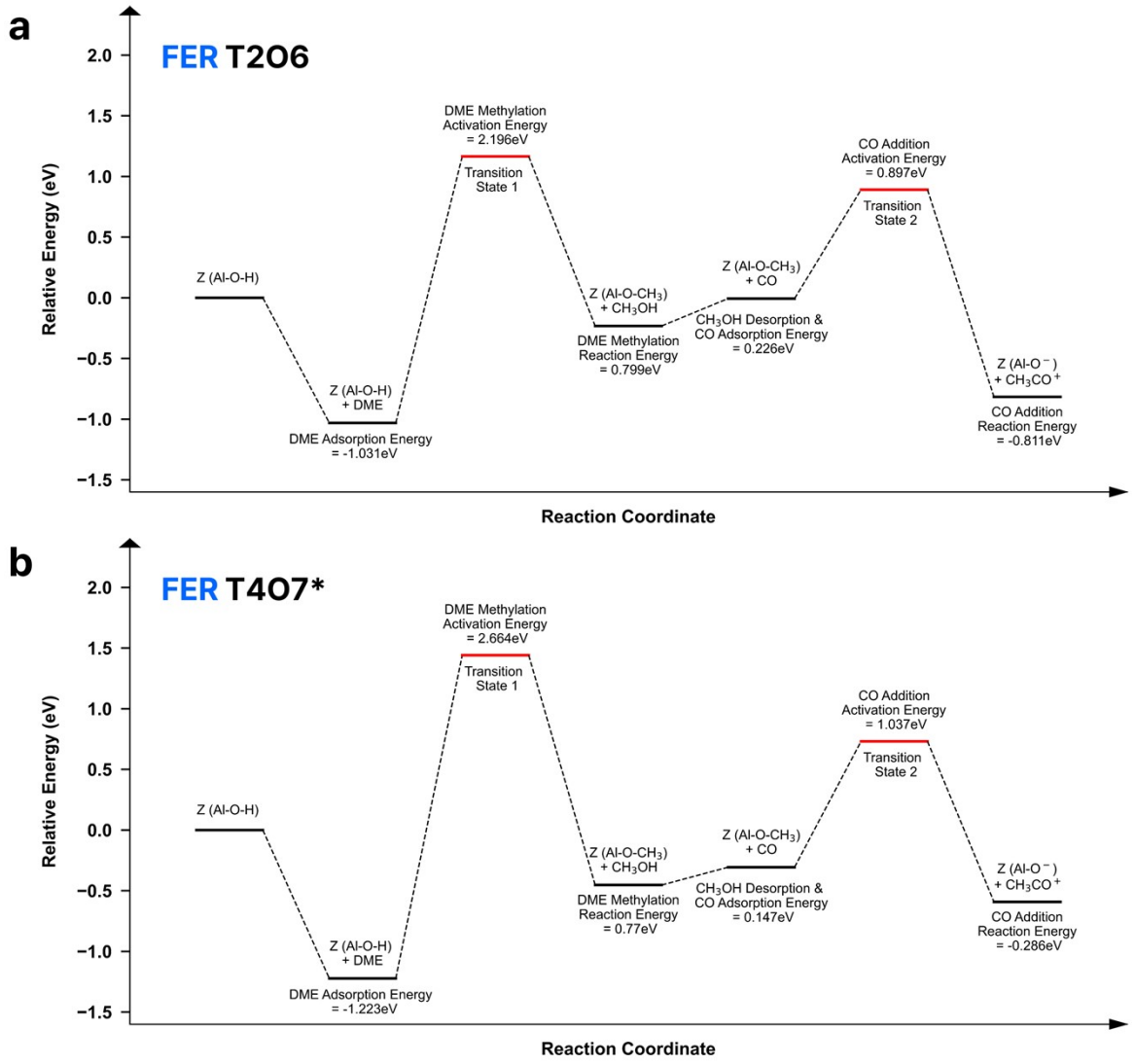

Fig S42. Full scheme of two key steps on DME carbonylation (methylation and CO addition step) energy diagram for some investigated TxOy site of the selected 8-MR zeolites: (a) FER T2O6, (b) FER T4O7.

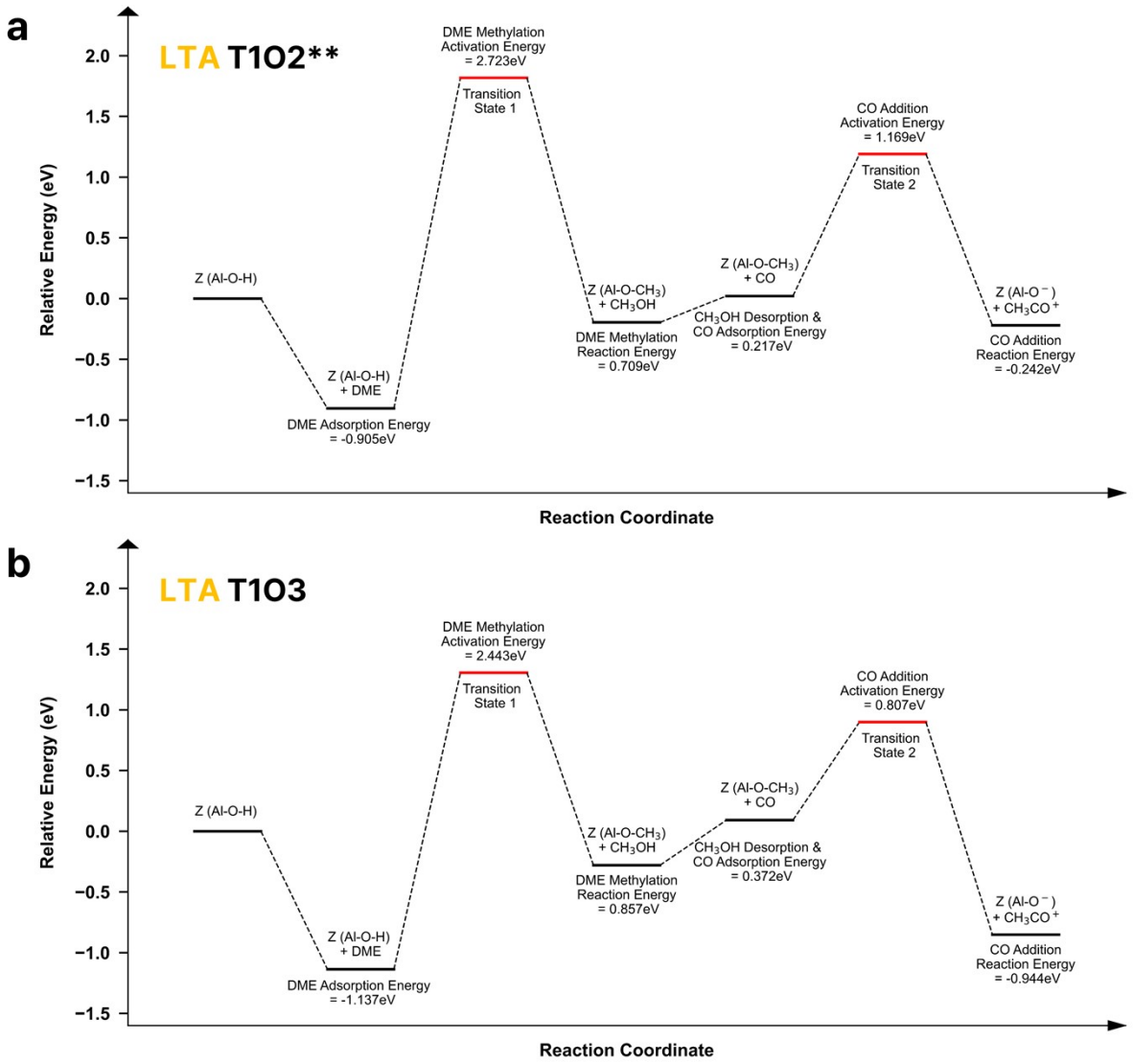

Fig S43. Full scheme of two key steps on DME carbonylation (methylation and CO addition step) energy diagram for some investigated TxOy site of the selected 8-MR zeolites: (a) LTA T1O2, (b) LTA T1O3.

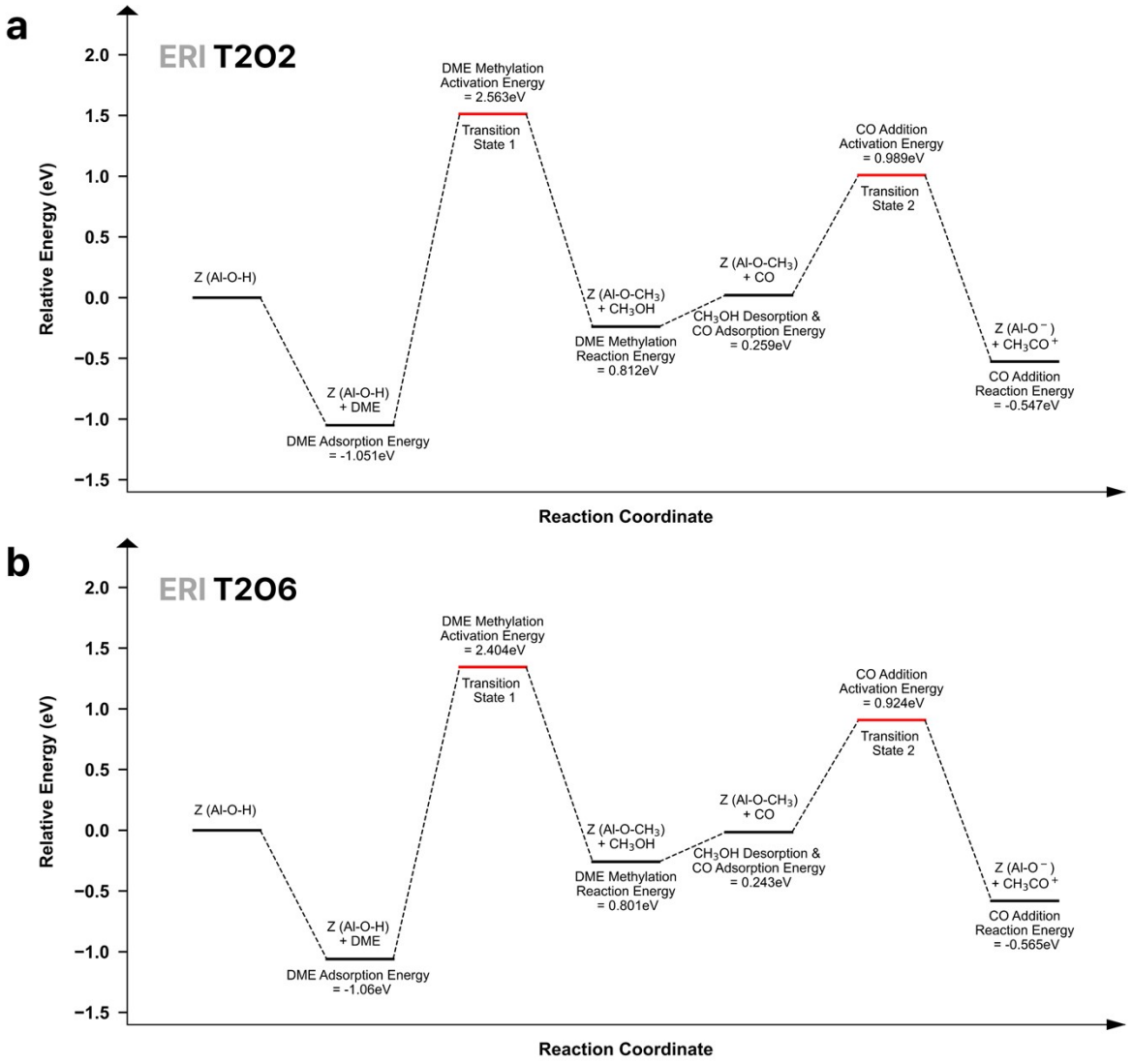

Fig S44. Full scheme of two key steps on DME carbonylation (methylation and CO addition step) energy diagram for some investigated TxOy site of the selected 8-MR zeolites: (a) ERI T2O2, (b) ERI T2O6.

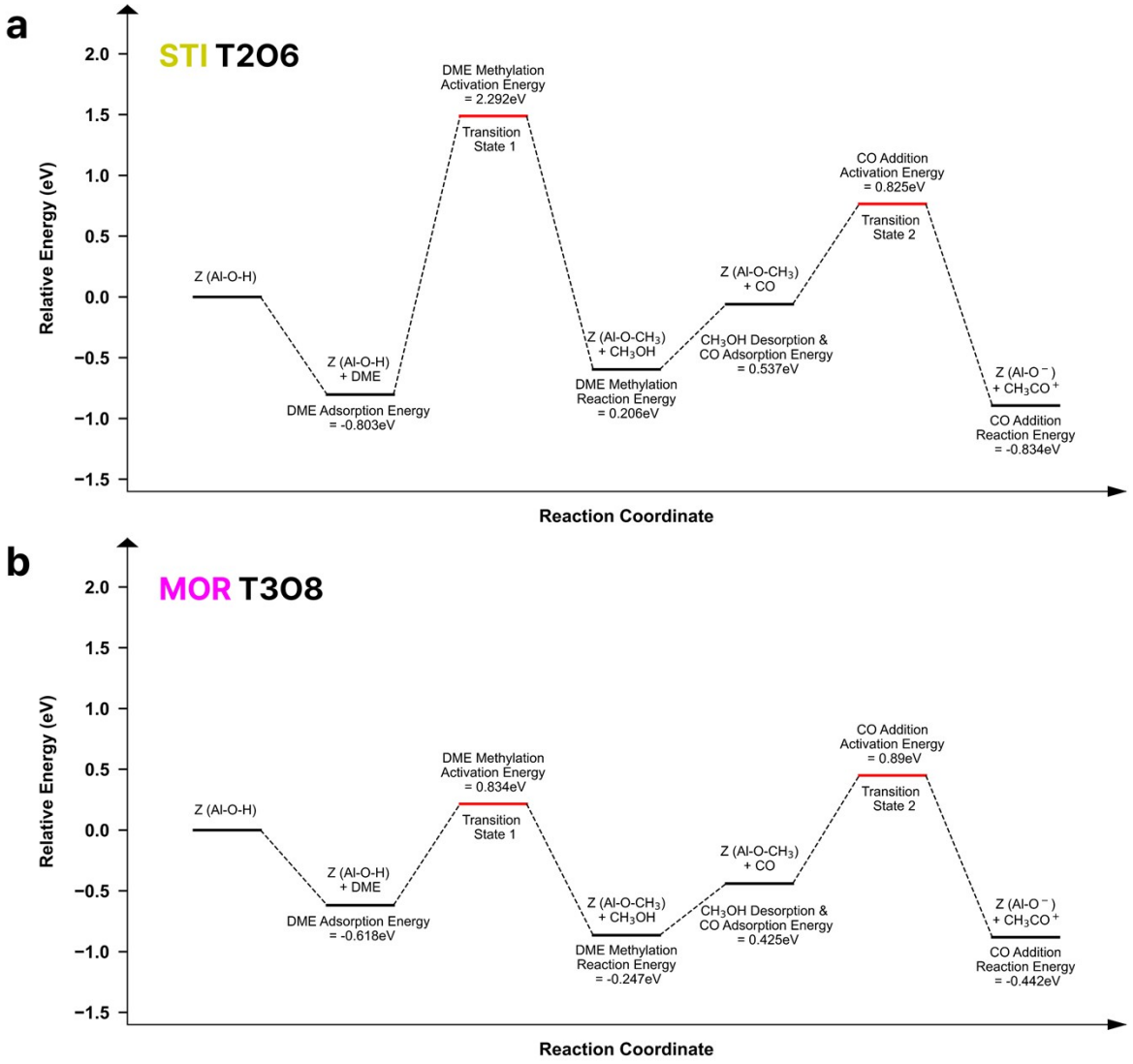

Fig S45. Full scheme of two key steps on DME carbonylation (methylation and CO addition step) energy diagram for some investigated TxOy site of the selected 8-MR zeolites: (a) STI T2O6, (b) MOR T3O8.

Structural descriptors for tested topologies

Table S3. Information of zeolite T site and O site and the orientation of surface methyl group (SMG) when substituted at the TxOy site.

Zeolite	T site	O site	Sharing with other T sites	8-ring siting	Methyl group orientation
CHA	T1	O1	None		Above 6-ring
		O2	None	○	Center of CHA-cage
		O3	None	○	8-ring pore
		O4	None	○	8-ring pore
FER	T1	O1	T3		Intersection of 10-ring and 8-ring
		O2	T2	○	Intersection of 10-ring and 8-ring
		O3	None	○	Intersection of 10-ring and 8-ring
		O4	None		8-ring pocket
	T2	O2	T1	○	Vicinal to 10-ring channel
		O5	T4		Above 6-ring
		O6a	None	○	Above 6-ring
		O6b	None	○	Vicinal to 10-ring channel
	T3	O1	T1		Intersection of 10-ring and 8-ring
		O7	T4		8-ring pocket
		O8	None		8-ring pocket
	T4	O5	T2		Above 6-ring
		O7	T3		8-ring pocket
LTA	T1	O1	None	○	8-ring pore
		O2	None		Above 6-ring
		O3	None	○	8-ring pore
ERI	T1	O1	None		Intersection of 6-ring and 8-ring
		O2	T2	○	8-ring pore
		O3	None		Above 6-ring
		O4	None	○	8-ring pore
	T2	O2	T1	○	8-ring pore
		O5	None		Above 6-ring
		O6	None	○	Center of ERI-cage
AEI	T1	O1	None		Above 6-ring
		O2	None		Center of AEI-cage
		O3	T2		8-ring pore
		O4	T3		8-ring pore
	T2	O3	T1		8-ring pore
		O5	T3		Above 6-ring
		O6	None		8-ring pore
		O7	T3		Center of AEI-cage
	T3	O4	T1		8-ring pore
		O5	T2		Above 6-ring
		O7	T2		Center of AEI-cage
		O8*	None		8-ring pore
STI	T1	O1	None		Vicinal to 10-ring channel
		O2	T3		Vicinal to 10-ring channel
		O3	T4		10-ring main channel
		O4	T2		10-ring main channel
	T2	O4	T1		10-ring main channel
		O5	T3		On the planary 8-ring
		O6	None		On the boat-shape 8-ring
	T3	O2	T1		Vicinal to 10-ring channel
		O5	T2		On the planary 8-ring
		O7	None		On the planary 8-ring
	T4	O3	T1		10-ring main channel
MOR	T3	O8	None		8-ring side pocket

* Equivalent to AEI T1O3 site.

Methyl group substitution on Brønsted acid site

[Atom color] Brown: Carbon, Pink: Hydrogen, Gray: Silicon, Cyan: Aluminum, Red: Oxygen.

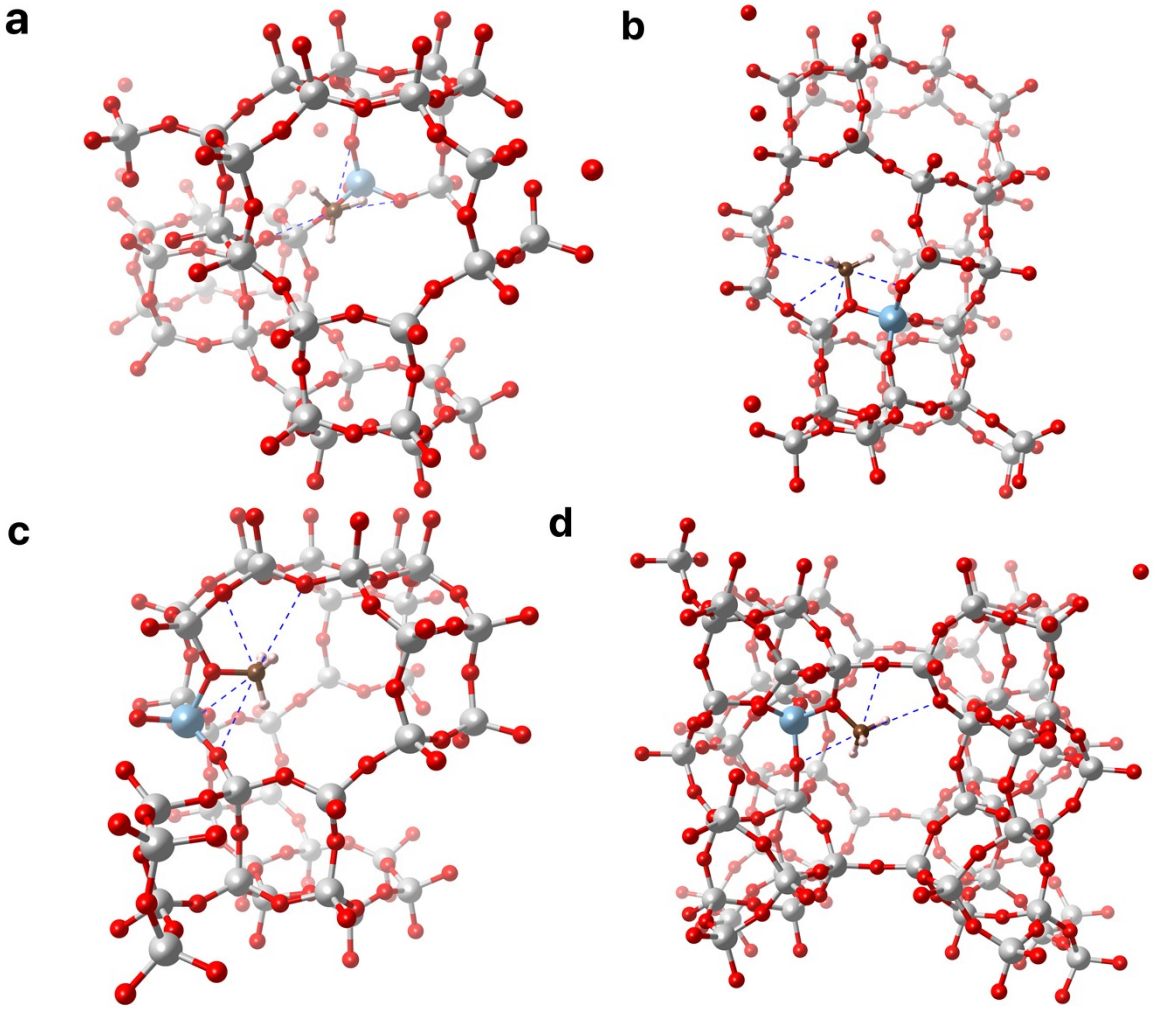

Fig S46. Framework geometries of the surface methyl group (SMG) for the investigated zeolites' TxOy sites including close-contact oxygen atoms (connected with blue dot lines): (a) CHA T1O2, (b) CHA T1O3, (c) CHA T1O4, and (d) FER T1O2.

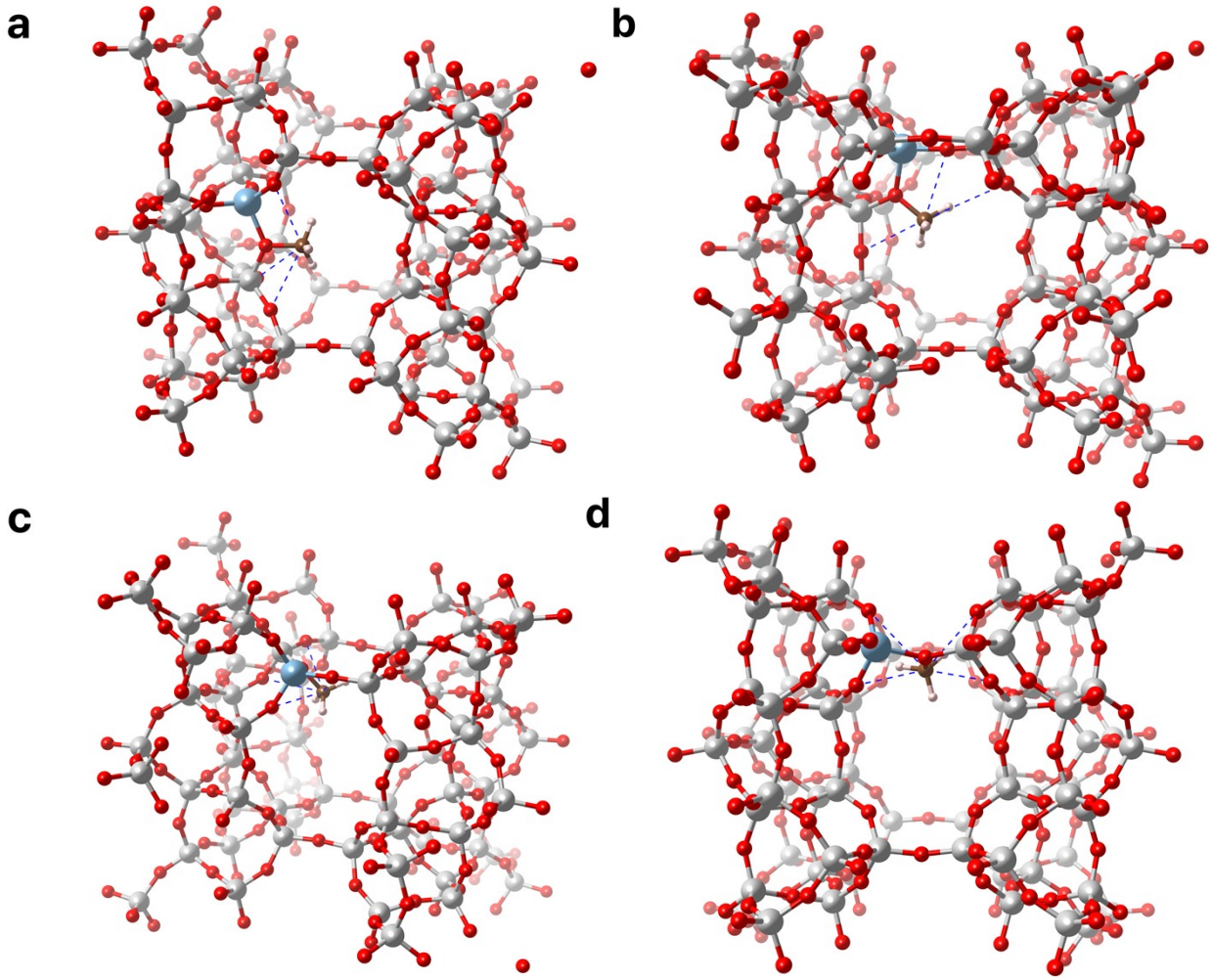

Fig S47. Framework geometries of the surface methyl group (SMG) for the investigated zeolites' TxOy sites including close-contact oxygen atoms (connected with blue dot lines): (a) FER T1O3, (b) FER T2O2, (c) FER T2O5, and (d) FER T2O6b (heading to 10-MR channel, see Table S3).

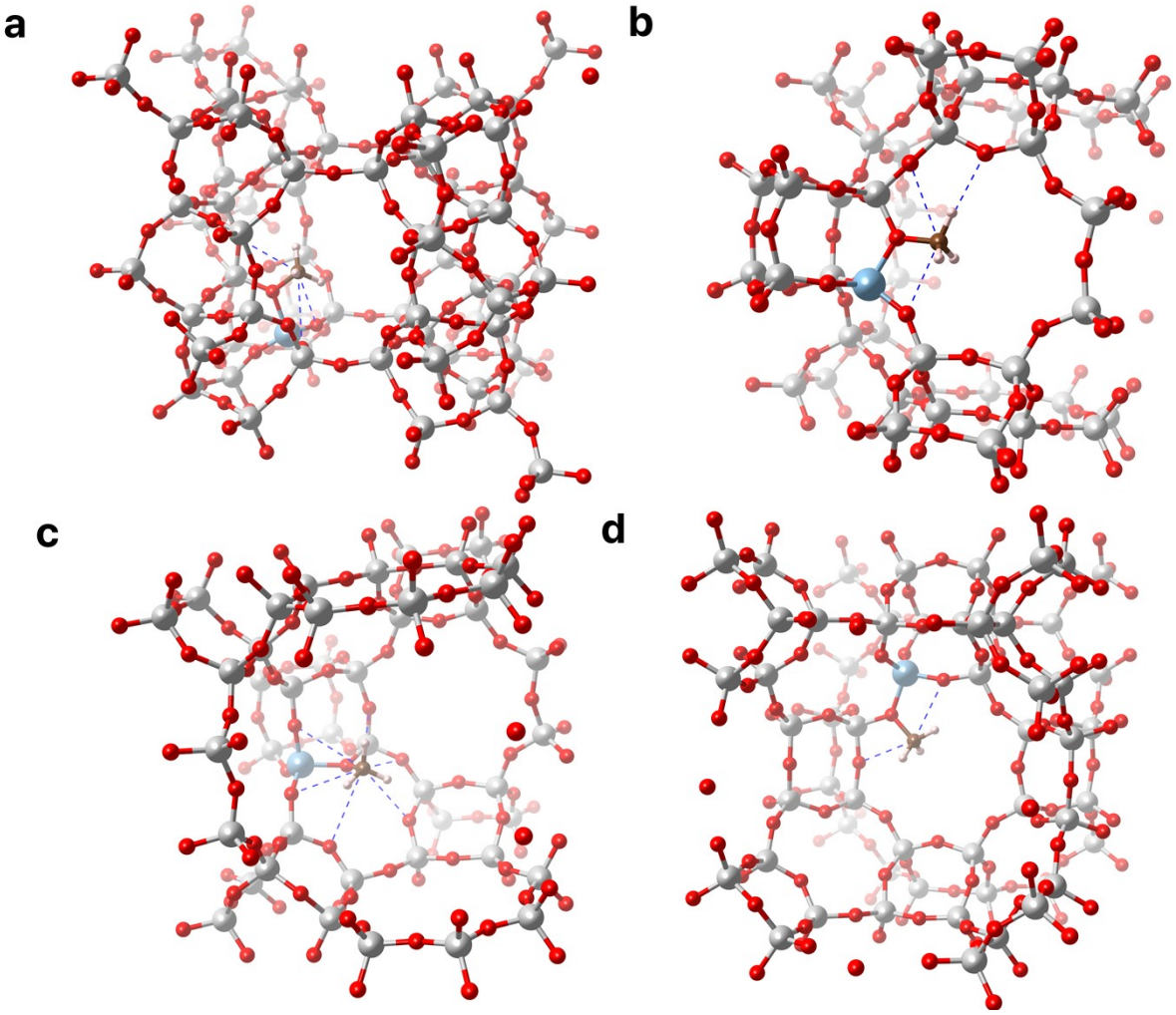

Fig S48. Framework geometries of the surface methyl group (SMG) for the investigated zeolites' TxOy sites including close-contact oxygen atoms (connected with blue dot lines): (a) FER T4O7, (b) LTA T1O1, (c) LTA T1O2, and (d) LTA T1O3.

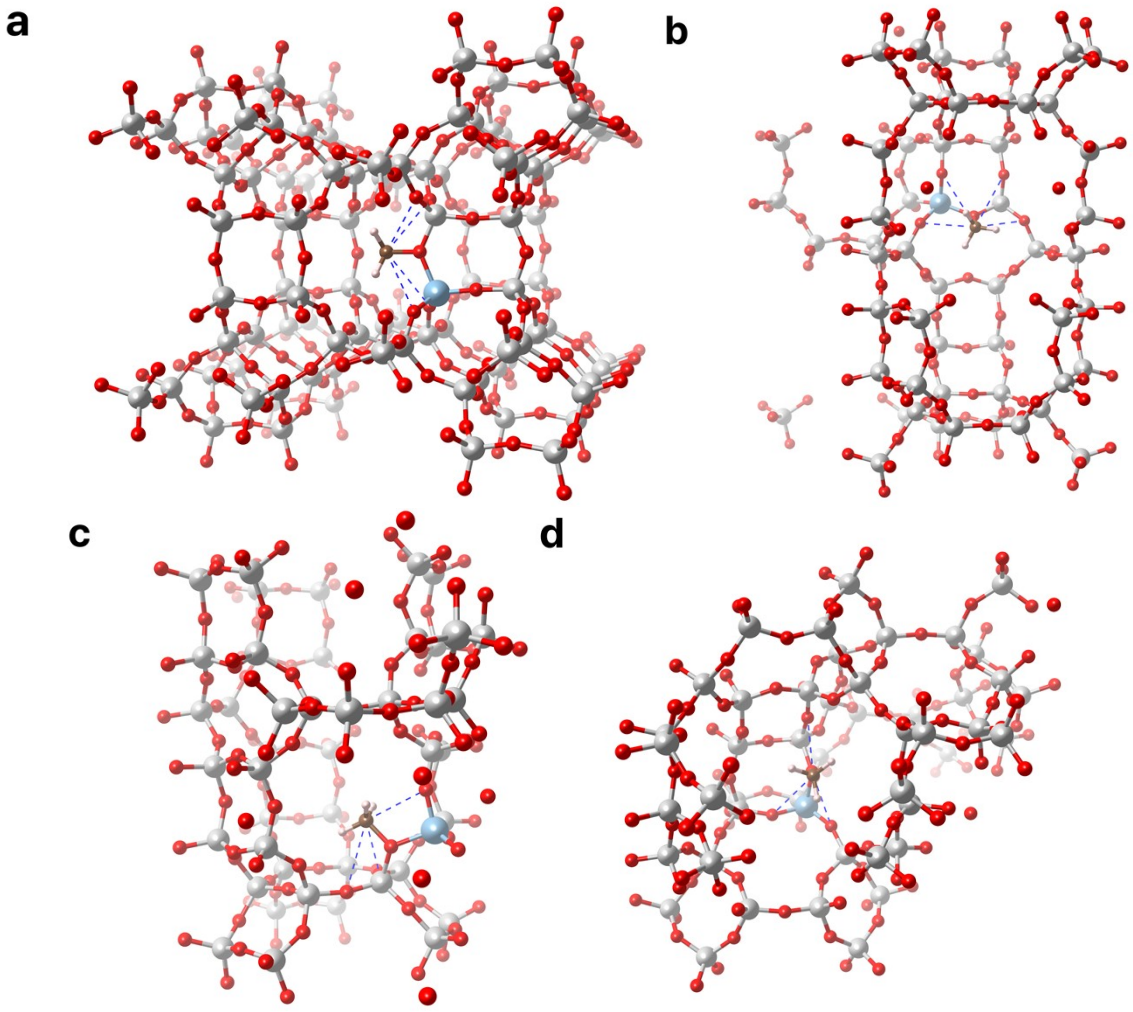

Fig S49. Framework geometries of the surface methyl group (SMG) for the investigated zeolites' TxOy sites including close-contact oxygen atoms (connected with blue dot lines): (a) MOR T3O8, (b) ERI T1O1, (c) ERI T1O2, and (d) ERI T2O2.

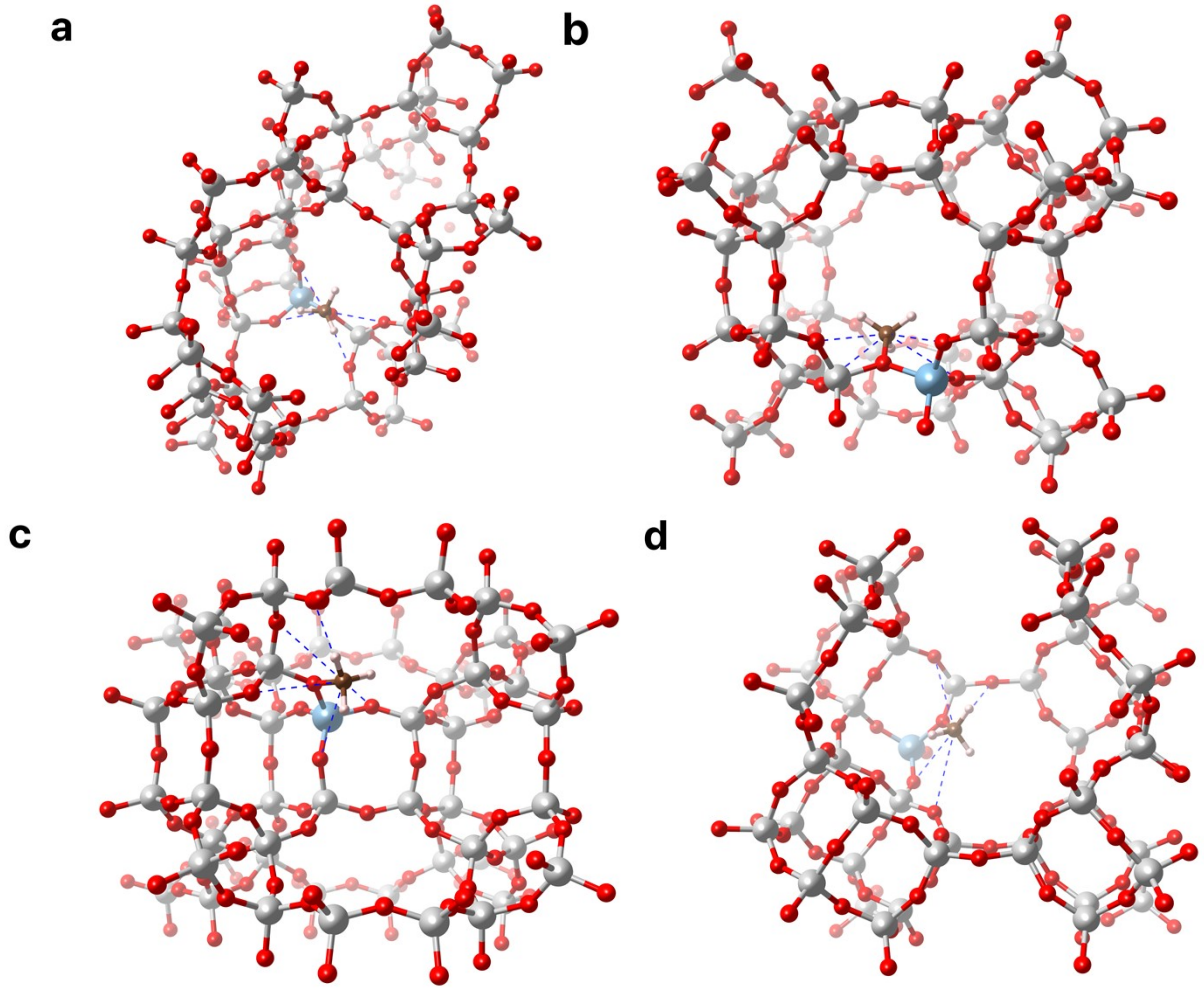

Fig S50. Framework geometries of the surface methyl group (SMG) for the investigated zeolites' TxOy sites including close-contact oxygen atoms (connected with blue dot lines): (a) ERI T2O6, (b) AEI T1O2, (c) AEI T1O4, and (d) AEI T2O3.

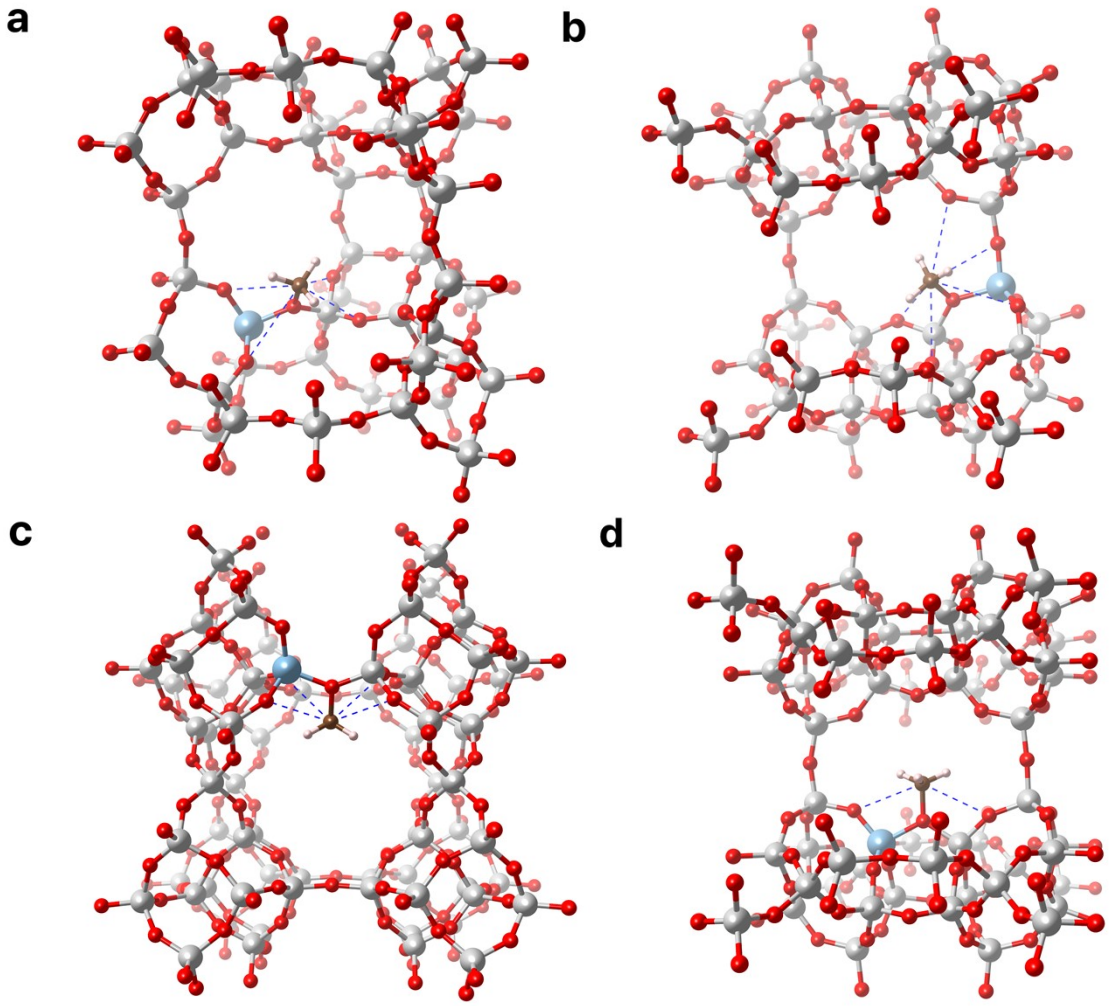

Fig S51. Framework geometries of the surface methyl group (SMG) for the investigated zeolites' TxOy sites including close-contact oxygen atoms (connected with blue dot lines): (a) AEI T3O7, (b) STI T2O5, (c) STI T2O6, and (d) STI T3O7.

Section 6

Pathway Competition: CO vs H_2O on the Surface methyl group

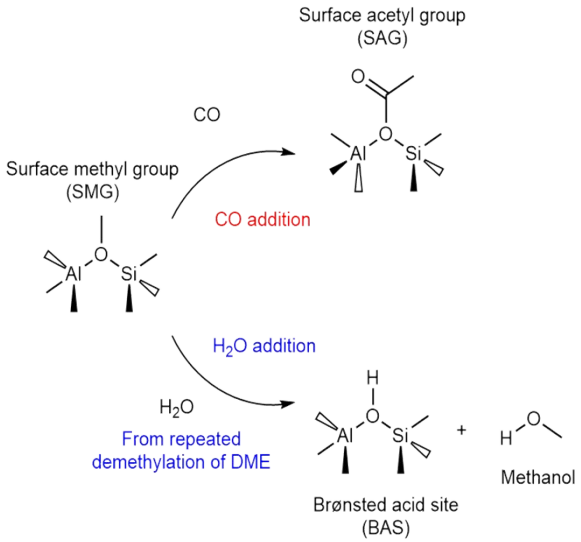

Fig S52. Competitive addition reaction pathway of CO and H_2O after surface methyl group (SMG) formation.

According to Boronat et al.[17], the initial adsorption of CH_3OR (R = CH_3 or H) on BAS within MOR or FER zeolites produces cationic intermediates, such as $CH_3OH_2^+$ or $CH_3OCH_4^+$. These intermediates subsequently decompose into ROH (H_2O or CH_3OH) molecules and a surface methyl group (SMG) bound to the TxOy site (see **Eq. 1 and 2**). The ability of a given zeolite topology to stabilize these intermediates during DME carbonylation is expected to influence its turnover frequency (TOF). To explore this further, we now examine the SMGs on the TxOy sites under study, aiming to clarify their function in the overall DME carbonylation mechanism.

$$CH_3OCH_3 + [Z\text{–}O(H)] \rightleftarrows CH_3OH + [Z\text{–}O(CH_3)] \quad \textbf{(Eq.1)}$$

$$CH_3OH + [Z\text{–}O(H)] \rightleftarrows H_2O + [Z\text{–}O(CH_3)] \quad \textbf{(Eq.2)}$$

Table S4. DFT-calculated activation energy ($\mathbf{E_a}$), reaction enthalpy ($\Delta\mathbf{E}$), and the ratio of the reaction rate constants for CO and H_2O addition pathways ($\frac{k_{CO}}{Ak_{H_2O}}$) at effective TxOy sites of selected zeolites.

Zeolite	Site	CO addition		H_2O addition		$k_{CO}/Ak_{H_2O}(\times 10^3)$
		$\mathbf{E_a}$ (eV)	$\Delta\mathbf{E}$ (eV)	$\mathbf{E_a}$ (eV)	$\Delta\mathbf{E}$ (eV)	
CHA	T1O4	1.014	-0.456	0.769	0.237	1.52
FER	T1O3	1.031	-0.507	0.739	0.114	0.44
	T4O7	1.037	-0.286	0.874	0.342	13.42
LTA	T1O2*	1.169	-0.242	0.921	0.257	1.41
ERI	T2O2	0.989	-0.547	0.739	0.114	18.54
	T2O6	0.924	-0.565	0.683	-0.009	1.67
AEI	T1O2	1.105	-0.445	0.916	0.175	6.27
STI	T2O6	0.825	-0.834	0.786	-0.142	353.08
MOR	T3O8	0.890	-0.442	0.704	0.200	7.31

*LTA T1O2 site is not belonged into 8-MR but address in this study as a special case, based on reports[8] that aluminum most preferred on the T1O2 site. See the Section 1 of this Supporting

As previously mentioned, although DME carbonylation can proceed efficiently via the CO addition to the pre-formed SMG, alternative reaction pathways become relevant when multiple nucleophilic reactants (e.g., CH_3OH and H_2O) are present. These species, generated through repeated demethylation steps of DME, increase the susceptibility of the SMG to competing side reactions. As shown in Fig. S52 above, H_2O addition inhibits the catalytic reaction by reversing the pathway after SMG formation back to the Brønsted acid site (BAS), thereby initializing the overall DME carbonylation mechanism. Therefore, simply examining the DFT-derived energy levels for each effective TxOy site (see **Maintext Section 2.2**) is insufficient for comparing TOF across different zeolite frameworks. It is critical to evaluate how favorably CO addition competes with the primary alternative pathway: H_2O addition.

Before the catalyst tests, each zeolite sample was pretreated at 500 °C for 1 hour under 1 bar N_2 to eliminate any previously adsorbed contaminants. Consequently, any H_2O detected during the reaction is attributed to its production in the methylation step. Thus, the competitive H_2O addition pathway is not merely a theoretical possibility but requires thorough examination under the reaction condition of this study.

Table S3 displays the activation energy ($\mathbf{E_a}$) and enthalpy ($\Delta\mathbf{E}$) for H_2O addition at each TxOy site. Notably, although CO addition consistently exhibits higher activation energies than H_2O addition, H_2O addition has a higher enthalpy relative to CO addition. Thus, the generation of H_2O from DME demethylation and its interference with the CO addition necessitate a quantitative evaluation of how the main CO addition pathway might be impeded by H_2O addition.

By examining the difference between the CO addition activation energy (E_{aCO}) and the H_2O addition activation energy (E_{aH_2O}), we can estimate the relative pathway selectivity for each zeolite group using the classic Arrhenius equation, which elucidates how activation energy influences rate constants.

$$k_{CO} = A_{CO}\, e^{\frac{-E_{aCO}}{k_B T}} \qquad \textbf{(Eq. 3)}$$

$$k_{H_2O} = A_{H_2O}\, e^{\frac{-E_{aH_2O}}{k_B T}} \quad \textbf{(Eq. 4)}$$

In **Eq. 3 and 4**, k_B is Boltzmann constant, and A_{CO} and A_{H_2O} are pre-exponential factors for the CO and H_2O addition pathways, respectively.

Each pre-exponential factor depends on temperature; however, since all reactions were conducted at the same temperature (165 °C), these factors can be treated as constant. Thus, the ratio $\frac{k_{CO}}{Ak_{H_2O}}$ provides a simplified quantitative measure of how readily CO addition occurs relative to H_2O addition at a specific TxOy site.

$$\frac{k_{CO}}{k_{H_2O}} = \frac{A_{CO}}{A_{H_2O}} e^{\left(\frac{-E_{aCO}}{k_B T} - \frac{-E_{aH_2O}}{k_B T}\right)} = A e^{-\frac{1}{k_B T}\left(E_{aH_2O} - E_{aCO}\right)} \quad \textbf{(Eq. 5)}$$

$$\frac{k_{CO}}{Ak_{H_2O}} = e^{-\frac{1}{k_B T}\left(E_{aH_2O} - E_{aCO}\right)} \quad \textbf{(Eq. 6)}$$

In **Eq. 5 and 6**, A is the ratio between the two pre-exponential factors, A_{CO} and A_{H_2O}.

Despite considerable effort, no clear correlation was observed between the $k_{CO}/(Ak_{H_2O})$ values and the observed TOF of each topology. For instance, some TxOy sites in ERI, AEI, and STI exhibit relatively high selectivity for the CO addition pathway (e.g., ERI T2O2: 18.54, AEI T1O2: 6.27, and STI T2O6: 353.08) comparable to MOR, yet these topologies still display lower TOF values.

Under the thermodynamically favorable conditions of this study—with a DME/CO ratio of 1:20—the high CO partial pressure (ca. 1.8 MPa) minimized the impact of H_2O addition on overall reactivity, thereby reducing the correlation between the proposed parameter and observed catalytic reactivity. This parameter becomes more important under kinetically favored condition, where a larger DME/CO ratio can enhance competing routes. The H_2O addition is kinetically more favorable than CO addition due to the fact that the activation energy ($\mathbf{E_a}$) for H_2O addition is consistently lower than that of CO addition across all the effective TxOy sites in Table S3, while the reaction enthalpy ($\boldsymbol{\Delta E}$) is conversely higher. As the DME/CO ratio increases, the excess DME potentially promotes the formation of H_2O at the TxOy sites, thereby enhancing competing reaction pathways and removing the surface methyl groups (SMGs).

Furthermore, under certain conditions, hydrocarbons may be formed through homologation and oligomerization processes involving DME.[17-21] These side reactions are more noticeable at acid sites in zeolite frameworks with pore dimensions larger than 8-MR. Conversely, when the largest pore in the zeolite is 8-MR, such side reactions are significantly reduced, allowing the suggested $k_{CO}/(Ak_{H_2O})$ parameter to remain an effective indicator. This is because homologation and oligomerization reactions are suppressed, and the reaction pathway is governed solely by the additions of CO and H_2O.

Consequently, only the interactions of these molecules with the methylated BAS within the 8-MR framework need to be considered.

Therefore, to isolate the intrinsic influence of the 8-MR framework itself without interference from larger pore-induced side reactions, all reaction tests were performed at 165 °C, which is the lowest temperature at which DME carbonylation can ordinarily occur. Although the low-temperature conditions may favor the H_2O addition pathway due to its lower activation energy, the partial pressure of CO applied in this study was substantially higher than that of H_2O from double demethylation of DME. As a result, the reaction passed through the thermodynamically favorable CO addition, leading to high MA selectivity.

However, in this Section, we aimed to evaluate the extent to which CO addition step is hindered by H_2O demethylated from DME, thereby assessing the relative ordering among the investigated zeolites in this regard and determining whether this is directly related to catalytic reactivity. Ultimately, the proposed parameter was found to be of limited effectiveness.

Beyond this perspective, we explored feasible alternative parameter and confirmed from previous studies that reactivity can be assessed by correlating it with geometrical factors at TxOy sites. The following section introduces this approach and evaluates whether it adequately explains the superior reactivity of the zeolite catalysts examined in this study. These results highlight the importance of water as a competitive inhibitor that suppresses forward carbonylation by regenerating BAS (remethylation).

Reference

1. M. Bocus, R. Goeminne, A. Lamaire, M. Cools-Ceuppens, T. Verstraelen and V. Van Speybroeck, Nuclear quantum effects on zeolite proton hopping kinetics explored with machine learning potentials and path integral molecular dynamics, *Nat. Commun.*, 2023, **14**, 1008.

2. Z. Zhao, Y. Xing, S. Li, X. Meng, F. Xiao, R. McGuire, A. N. Parvulescu, U. Müller and W. Zhang, Mapping Al distributions in SSZ-13 zeolites from 23Na solid-state NMR spectroscopy and DFT calculations, *J. Phys. Chem. C*, 2018, **122**, 9937–9979.

3. M. Lusardi, T. T. Chen, M. Kale, J. H. Kang, M. Neurock and M. E. Davis, Carbonylation of dimethyl ether to methyl acetate over SSZ-13, *ACS Catal.*, 2019, **10**, 842–851.

4. A. Bhan, A. D. Allian, G. J. Sunley, D. J. Law and E. Iglesia, Specificity of sites within eight-membered ring zeolite channels for carbonylation of methyls to acetyls, *J. Am. Chem. Soc.*, 2007, **129**, 4919–4924.

5. W. Chu, X. Liu, Z. Yang, H. Nakata, X. Tan, X. Liu, L. Xu, P. Guo, X. Li and X. Zhu, Constrained Al sites in FER-type zeolites, *Chin. J. Catal.,* 2021, **42**, 2078–2087.

6. A. Martucci, A. Alberti, G. Cruciani, P. Radaelli, P. Ciambelli and M. Rapacciulo, Location of Brønsted sites in D-ferrierite by neutron powder diffraction, *Microporous Mesoporous Mat.,* 1999, **30**, 95–101.

7. P. Feng, G. Zhang, X. Chen, K. Zang, X. Li and L. Xu, Specific zone within 8-membered ring channel as catalytic center for carbonylation of dimethyl ether and methanol over FER zeolite, *Appl. Catal. A-Gen.*, 2018, **557**, 119–124.

8. T. Lemishko, S. Valencia, F. Rey, M. Jiménez-Ruiz and G. Sastre, Inelastic neutron scattering study on the location of Brønsted acid sites in high silica LTA zeolite, *J. Phys. Chem. C*, 2016, **120**, 24904–24909.

9. C. Beauvais, X. Guerrault, F. Coudert, A. Boutin and A. Fuchs, Distribution of sodium cations in faujasite-type zeolite: Acanonical parallel tempering simulation study, *J. Phys. Chem. B*, 2004, **108**, 399–404.

10. J. Sauer, Sodium doped sodium sodalite: Magnetic coupling between F centers and hyperfine interactions with framework atoms, *Phys. Chem. Chem. Phys.*, 1999, **1**, 4505–4514.

11. H. Trill, H. Eckert and V. Srdanov, Topotactic transformations of sodalite cages: Synthesis and NMR study of mixed salt-free and salt-bearing sodalites, *J. Am. Chem. Soc.*, 2002, **124**, 8361-8370.

12. K. Lillerud, Aluminium distribution in the zeolites offretite and erionite, *Zeolites*, 1987, **7**, 14–17.

13. G. Engelhardt and D. Michel, High-resolution solid-state NMR of silicates and zeolites, *Wiley*, New York, 1987.

14. R. Fletcher, S. Ling and B. Slater, Violation of Löwenstein's rule in zeolites, *Chem. Sci.*, 2017, **8**, 7483–7491.

15. B. W. Boal, J. E. Schmidt, M. A. Deimund, M. W. Deem, L. M. Henling, S. K. Brand, S. I. Zones and M. E. Davis, Facile synthesis and catalysis of pure-silica and heteroatom LTA, *Chem. Mat.*, 2015, **27**, 7774–7779.

16. M. Dusselier, M. A. Deimund, J. E. Schmidt and M. E. Davis, Methanol-to-olefins catalysis with hydrothermally treated zeolite SSZ-39, *ACS Catal.*, 2015, **5**, 6078–6085.

17. M. Boronat, C. Martinez and A. Corma, Mechanistic differences between methanol and dimethyl ether carbonylation in side pockets and large channels of mordenite, *Phys. Chem. Chem. Phys.*, 2011, **13**, 2603–2612.

18. Y. Li, W. Guo, W. Fan, S. Yuan, J. Li, J. Wang, H. Jiao and T. Tatsumi, A DFT study on the distributions of Al and Brönsted acid sites in zeolite MCM-22, *J. Mol. Catal. A-Chem.*, 2011, **338**, 24–32.

19. K. Cai, S. Huang, Y. Li, Z. Cheng, J. Lv and X. Ma, Influence of acid strength on the reactivity of dimethyl ether carbonylation over H-MOR, *ACS Sustain. Chem. Eng.*, 2018, **7**, 2027–2034.

20. W. Chen, Z. Liu, X. Yi and A. Zheng, Confinement-driven dimethyl ether carbonylation in mordenite zeolite as an ultramicroscopic reactor, *Acc. Chem. Res.*, 2024, **57**, 2804–2815.

21. Y. Li, Q. Sun, S. Huang, Z. Cheng, K. Cai, J. Lv and X. Ma, Dimethyl ether carbonylation over pyridine-modified MOR: Enhanced stability influenced by acidity, *Catal. Today*, 2018, **311**, 81–88.